Triggerstudien zur Suche nach stabilen, massiven Teilchen mit dem ATLAS-Detektor

Trigger studies for the search for stable massive particles with the ATLAS detector

Masterarbeit an der Fakultät für Physik
der
Ludwig-Maximilians-Universität München

vorgelegt von
Vincent Kitali
geboren in Hameln

München, den 30. September 2015

Abstract

Results of trigger studies for the search for stable massive particles with the ATLAS detector are presented. The study uses 19.3 fb^{-1} of $\sqrt{s} = 8$ TeV data collected in 2012 as well as 85 pb^{-1} of $\sqrt{s} = 13$ TeV data collected in 2015. Stable massive particles (SMP) are predicted by several promising particle physics models beyond the Standard Model. SMPs are expected to be produced at velocities significantly below the speed of light. Among other properties of SMPs this leads to a low efficiency of most trigger items. Missing transverse energy (E_T^{miss})-triggers have the highest efficiency in the selection of events, in which very massive, stable particles are produced. The influence of the detector noise and particle–detector interactions on the event selection with E_T^{miss}-triggers is calibrated with $Z \to \mu\mu$-event data.

The parametrisation of the event selection with six different fit functions is tested and the best performing fit function is found to be the error function. Newly developed methods to estimate systematic uncertainties of trigger efficiencies, the so-called contour and grid methods, as well as the previously used method are presented and tested. The comparison between the performances of the uncertainty estimation methods is presented, with the contour method being the best performing. The E_T^{miss}-trigger efficiencies are found to increase from trigger items used in 2012 to comparable trigger items used in 2015. The systematic uncertainties of the new trigger items are found to range between 2.0% and 5.3%.

Zusammenfassung

Die Resultate von Triggerstudien zur Suche nach stabilen, massiven Teilchen mit dem ATLAS Detektor werden präsentiert. Die Studie verwendet 19.3 fb^{-1} Daten, die bei $\sqrt{s} = 8$ TeV im Jahr 2012 gesammelt wurden, sowie 85 pb^{-1} Daten, die bei $\sqrt{s} = 13$ TeV 2015 genommen wurden. Stabile, massive Teilchen (SMP) werden von einer Reihe von vielversprechenden Teilchenphysikmodellen jenseits des Standardmodells vorhergesagt. Es wird erwartet, dass SMPs bei Geschwindigkeiten deutlich unterhalb der Vakuumlichtgeschwindigkeit produziert werden. Neben anderen Eigenschaften von SMPs führt dies zu einer geringern Effizienz der meisten Trigger. Fehlende Transveralenergie (E_T^{miss})-Trigger zeigen die höchste Effizienz in der Auswahl von Ereignissen, in denen besonders schwere, stabile Teilchen erzeugt werden. Der Einfluss von Detektorrauschen und Teilchen–Detektor Wechselwirkungen auf die Ereignisselektion mit E_T^{miss}-Triggern wird mithilfe von $Z \to \mu\mu$-Ereignis-Daten kalibriert.

Die Parametrisierung der Ereignisselektion mit sechs verschiedenen Fitfunktionen wird getestet und die Fehlerfunktion wird als die am besten geeignete Fitfunktion identifiziert. Neu entwickelte Methoden zur Abschätzung systematischer Unsicherheiten von Triggereffizienzen, die sogenannten Contour- und Gridmethoden, sowie die zuvor verwendete Methode werden präsentiert und untersucht. Der Vergleich zwischen den Güten der Methoden zur Abschätzung der Unsicherheiten wird präsentiert und die Contourmethode wird als die Methode mit der höchsten Qualität identifiziert. Die Effizienzen vergleichbarer E_T^{miss}-Trigger zeigen eine Steigerung im Vergleich zwischen den Datennahmen in 2012 und in 2015. Die systematischen Unsicherheiten der neuen Trigger haben Werte zwichen 2.0% und 5.3%.

Contents

Chapter 1

Introduction

The Standard Model (SM) has shaped our view of the fundamental laws of the Universe and it continues to do so until this day. After the discoveries of the last elementary Standard Model fermions, the top quark in 1995 as well as the tau neutrino in 2000 at the Tevatron [1–3], and the discovery of a scalar boson compatible with the Standard Model Higgs boson at the Large Hadron Collider (LHC) in 2012 [4, 5], almost every prediction of the SM was verified by experiments. Constructed as a fundamental theory the Standard Model was designed to describe every phenomenon observed in nature. However, many exact results can in practice only be calculated via theories derived from the SM. As such, for example, classical electrodynamics can be seen as a limit of a more fundamental quantum field theory (QFT) and therefore a limit of the SM.

There are however phenomena that can not be described by the SM. The indirect detection of Dark Matter [6] suggests the existence of at least one more particle, which is not part of the SM. Furthermore, neutrino oscillation, which was observed in the research of the solar neutrino spectrum among other experiments [7–9], is a process, which can not be described by SM interactions. These phenomena, as well as the hierarchy problem [10], underline the necessity of new fundamental theories.

There are numerous models [11–19], known as Beyond Standard Model (BSM) theories, with the potential to become the first theory to describe a phenomenon beyond the SM. Many of those models introduce a new symmetry called Supersymmetry (SUSY). A description of SUSY and BSMs will be given in this work.

The discovery of a Higgs-like boson in 2012 clearly showed the ability of the experiments ATLAS (A Toroidal LHC ApparatuS) [4] and CMS (Compact Muon Solenoid) [5] to discover new particles even at centre-of-mass energies of 7 and 8 TeV and therefore below the design energy of the LHC. After the end of data taking in 2012 the LHC and ATLAS underwent a couple of changes to reach the new record centre-of-mass energy of 13 TeV in 2015 and 14 TeV in the near future. The changes most relevant to the research discussed here will be covered in detail in this work. Despite the fact, that no clear proof of BSM physics was found before this long shutdown, there are numerous indications for New Physics to be discovered with the LHC in the near future [20], making the next few years potentially one of the most exciting eras in the history of particle physics.

Given the fact, that there are multiple stable and metastable particles in the SM, it is not surprising, that a high number of BSM theories predict the existence of new particles with long or infinite lifetimes [12–19, 21]. Especially the existence of Dark Matter is proof for at least one stable particle, which has not yet been discovered. The search for stable and metastable particles could therefore be central to the search for New Physics. One reason why these long-lived particles escaped discovery thus far could be their high mass, making it unlikely or even impossible to produce them with collider experiments at centre-of-mass energies of 8 TeV and below. These high masses discriminate new long-lived particles from all

examples for particles with long lifetimes in the SM. This leads to a significant difference in velocity between SM and beyond SM long-lived particles at LHC energies. This work contains a detailed description of the unique challenges in the search for stable, massive particles (SMP) resulting from the properties of SMPs.

A huge challenge for modern high-energy physics (HEP) is the storage and processing of large amounts of data. In the ATLAS experiment this challenge is met with the preselection of interesting events using triggers [22, 23] and therefore deleting large amounts of data directly during data taking. It is left to the analysis groups to decide, which of the available trigger items are most suitable for their analyses and to estimate how efficient these triggers are in selecting events containing interesting processes.

Due to Poincaré invariance the momenta of all particles produced in collider experiments add up to zero. Because of the production of particles, that are invisible to the detector, and other phenomena, missing energy transverse to the beam axis is a common property of hadron collision events. Processes containing stable, massive particles give rise to missing transverse energy (E_T^{miss}) as well. The use of E_T^{miss} triggers in the search for SMPs as well as the calculation of their efficiencies in selecting SMP events is the central focus of this work. During the long shutdown of the LHC multiple challenges but also innovations met the analysis of E_T^{miss} triggers in the search for SMPs. The results of these innovations will be presented here using ATLAS data taken not only before the long shutdown of the LHC but also at the record centre-of-mass energy of 13 TeV in 2015.

In chapter 2 of this thesis a description of the Standard Model is given with a focus on proton–proton collisions at high energies. The search for SMPs with its unique challenges is also discussed in that chapter. This is complemented with a discussion of BSMs predicting stable, massive particles, with Supersymmetry being the most important one. A description of the ATLAS detector is given in chapter 3. All parts of the detector and their functionality as well as the event selection using multiple trigger levels are depicted in the same chapter. Chapter 4 contains the methods used in the analysis of E_T^{miss} triggers for the search for SMPs. The procedure of estimating trigger efficiencies, which was used in the search for SMPs with data taken by the ATLAS detector at 8 TeV centre-of-mass energy [24], is described in detail in that chapter. This is complemented by a discussion of new methods designed to achieve greater accuracy in that calculation. The results of the analysis with these methods, using data taken by the ATLAS detector in 2015, are presented in chapter 5.

The conclusion of the analysis can be found in chapter 6 together with an outlook on the search for SMPs with the ATLAS detector in the near future.

Chapter 2

Theory

In the following natural units will be used unless stated otherwise:

$$\hbar = c = 1. \tag{2.1}$$

2.1 The Standard Model and proton-proton collisions

The Standard Model of particle physics (SM)[1] is an effective quantum field theory describing three of the four fundamental interactions between elementary particles. An effective theory is only applicable up to a certain energy scale as it is expected to be the limit of a more fundamental theory. The SM is expected to break down at the Planck scale ($\Lambda_P \simeq 10^{19}$ GeV) at the latest [10].

Table 2.1: Elementary particles of the Standard Model. Particle symbols (large letters) together with spin, electromagnetic charge and mass on the right as well as the lifetime of the particle below the symbol. Lifetimes were calculated from the decay width via $\tau = 1/\Gamma$ as defined in equation 2.2. The particle data was taken from Ref.[26] or from Ref.[27]. *The neutrino lifetimes are speculative and neutrino oscillation (See section 2.3) is ignored at this point. †The Higgs lifetime is estimated from the theoretical predictions in Ref.[28].

u	1/2 2/3 ∞	2.3 MeV	c	1/2 2/3 $\sim 10^{-13}$ s	1.3 GeV	t	1/2 2/3 $\sim 10^{-25}$ s	173 GeV	γ	1 0 ∞	0
d	1/2 -1/3 ∞	4.8 MeV	s	1/2 -1/3 $\sim 10^{-8}$ s	95 MeV	b	1/2 -1/3 $\sim 10^{-12}$ s	4.7 GeV	g	1 0 ∞	0
e	1/2 -1 ∞	0.5 MeV	μ	1/2 -1 2×10^{-6} s	105 MeV	τ	1/2 -1 3×10^{-13} s	1.8 GeV	Z	1 0 3×10^{-25} s	91 GeV
ν_e	1/2 0 ∞^*	< 2 eV	ν_μ	1/2 0 ∞^*	< 2 eV	ν_τ	1/2 0 ∞^*	< 2 eV	$W^\pm$	1 ± 1 3×10^{-25} s	80 GeV
									h	0 0 $\sim 10^{-22}$ s†	125 GeV

[1] A more detailed introduction to the SM can be found in [25]

In table 2.1 the elementary particle content of the SM is shown together with some of the quantum numbers and continuous properties of the particles. It includes spin 1/2 fermions divided into three flavours of up-type quarks (u, c, t), down-type quarks (d, s, b), charged leptons (e, μ, τ) and uncharged leptons or neutrinos (ν_e, ν_μ, ν_τ). The SM describes interactions through the exchange of spin 1 bosons. The electromagnetic interaction is communicated via the photon (γ) and affects only particles with an electromagnetic charge. The electromagnetic charge is conserved resulting from a symmetry between particles and antiparticles[2], which only differ from each other by charge-like quantum numbers, hence the particle content of the SM is almost[3] doubled by this symmetry. The Z and $W^{\pm}$ bosons mediate the weak interaction with the latter making flavour changing interactions possible. The unified symmetry between electromagnetism and weak theory, the electroweak symmetry, is broken due to the Higgs-mechanism and therefore due to the interaction with the scalar (spin quantum number= 0) Higgs boson (h)[4].

The last interaction described by the SM is the strong interaction, which is mediated by the gluons (g). The gluons couple to every particle with a colour charge namely quarks and other gluons. The colour charge is analogous to the electromagnetic charge except there are three types of colour charge (red, green and blue). The underlying symmetry[5] is unbroken on every energy scale within reach of experiments, which means that it is unnecessary to view, for example, up quarks with different colour charges as different particles analogous to the distinction between electron and antielectron (positron). The colour charge is a charge-type quantum number, which means that antiparticles have anticolour charges (antired, antigreen and antiblue).

There are no naturally occurring colour-charged states, because quarks and gluons become confined in colourless multi-parton states in a process called hadronisation. A colourless multi-parton state (hadron) is either the union of the same amount of colour and anticolour particles or of the same amount of particles with each of the three colour charges forming typically two-quark (mesons) or three-quark states (baryons)[6]. The typical timescale for the hadronisation process as measured by the ALICE (A Large Ion Collider Experiment) experiment is 0.4 ± 0.1 fm [32].

2.1.1 Proton-proton collisions at the 10 TeV scale

Protons are composite particles with two up quarks and one down quark as valence partons. Though the masses of the quarks only sum up to 9.4 MeV the proton mass is actually as large as $m_p = 938$ MeV [26]. The large difference between parton masses and proton mass can be attributed to the binding energy resulting from interactions mainly between gluons inside the proton. The relevant interactions in collisions between protons at around 10 TeV centre-of-mass energy, and thus at an energy scale four orders of magnitude larger than the proton binding energy, are therefore parton interactions.

In figure 2.1 a Feynman diagram[7] of a proton-proton interaction resulting in an arbitrary final state is depicted. One of the protons emits a gluon before the interaction, which leads to initial state radiation (ISR) and hadronisation of the gluon. Due to the high rate of strong interactions inside a proton, ISR is very common in proton-proton collisions.

[2]The antiparticle of a particle x is often denoted as $\bar{x}$. The relation between symmetry and conservation law is given by Noether's theorem [29].

[3]Charge eigenstates like the photon are their own antiparticle.

[4]More on electroweak symmetry breaking in chapter 10.8 of Ref.[25].

[5]The symmetry group is SU(3). More on group theory as a concept in quantum field theories in Ref.[30].

[6]No law prevents the formation of combinations of mesons and baryons. In fact pentaquarks were recently observed at LHCb (Large Hadron Collider beauty experiment) [31].

[7]Feynman diagrams visualise particle interactions either in a simplified way as in this case or in mathematically accurate way, from which cross-sections or lifetimes can be calculated. More on Feynman diagrams can be found in Ref.[25].

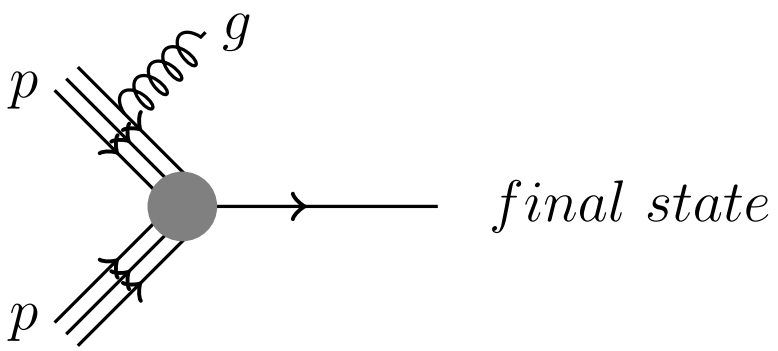

Figure 2.1: Initial state radiation emitted by one of the constituents of one of the protons in a proton-proton interaction into an arbitrary final state.

2.2 Long-lived particles

Many elementary and composite particles can decay into lighter particles in a finite amount of time, which is called the lifetime. Since every process in a quantum field theory is of statistical nature, a meaningful definition of the term "lifetime" can only be given for a large amount of particles. As such the number of particles n at a given time t is described by

$$n(t) = n(t=0) \cdot \mathrm{e}^{-\frac{t}{\tau}}, \tag{2.2a}$$

$$\tau = \frac{1}{\Gamma}, \tag{2.2b}$$

where the mean lifetime or simply "lifetime" τ is the time, after which the number of particles shrinks to e^{-1} of its original size and Γ is the decay rate. The lifetime is a continuous property of every particle[8]. The definition of long-lived is therefore not unique and depends on the properties of the ATLAS detector (See section 3.2) in this work. For a particle to be regarded as long-lived, it has to possess a long enough lifetime to make particle–detector interactions possible.

The general expression for the decay rate of a particle with mass m_1 decaying into $n-1$ particles with the mass of the ith particle m_i is given by Fermi's golden rule[9]

$$\Gamma = \frac{S}{2m_1} \int |\mathcal{M}|^2 \delta^4(p_1 - \sum_{i=2}^{n} p_i) \prod_{j=2}^{n} 2\pi\delta(p_j^2 - m_j^2)\theta(E_j)\mathrm{d}^4 p_j, \tag{2.3}$$

where S is a combinatoric factor to avoid double counting of final states, p_i is the four-momentum of the ith particle and E_i is its energy. $\mathcal{M}$ is the Feynman amplitude, which contains all dynamical information about the process. The Dirac delta function $\delta(x)$ and the Heaviside function $\theta(x)$ secure energy and momentum conservation. If a particle has multiple decay modes the decay rate is the sum of all partial decay rates.

It can be derived from Fermi's golden rule, that the lifetime of a particle depends on several factors. Its quantum numbers together with the respective symmetry and therefore a conservation law dictate, which decays if any are allowed. The mass of the particle adds another restriction, because the decay into particles with a higher mass sum than the mass of the initial particle is forbidden for kinematic reasons as can easily be seen in the reference frame, in which the mother particle is at rest. It is important to note, that this restriction

[8] The lifetime of a particle is equal to the lifetime of its antiparticle.
[9] See for example chapter 6 of Ref.[25].

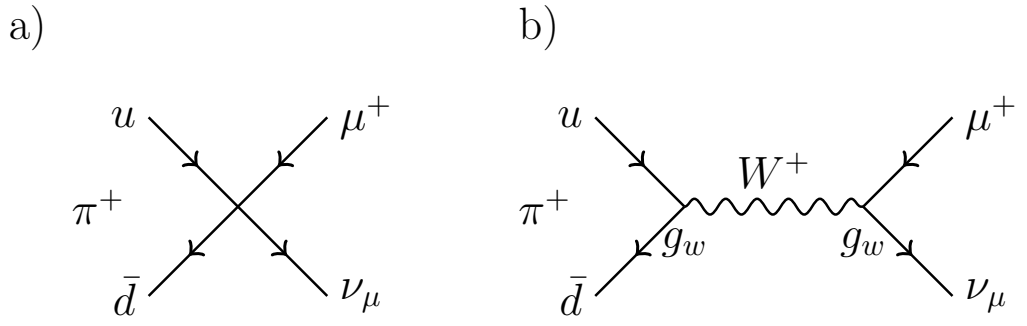

Figure 2.2: Decay of the π^+ a) with a four-point interaction, which is a good approximation at energies below the W mass, and b) with the exchange of the W boson as a mediator.

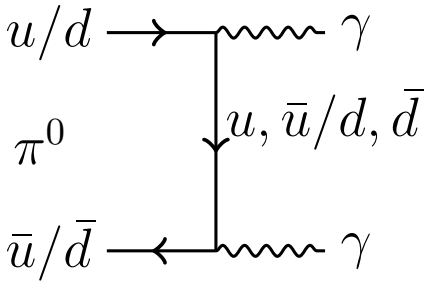

Figure 2.3: Dominant π^0 decay mode. Decay into two photons.

is only true, while comparing the kinematics of initial and final state. Decays via a heavy, intermediate particle are suppressed, but not forbidden.

This can be seen by taking the decay of the mesons π^+ (quark content $u\bar{d}$) and π^0 (the quark content is a superposition of $u\bar{u}$ and $d\bar{d}$) into account. The dominant π^+ decay mode a) via a four-point interaction and b) via a heavy mediator particle is shown in figure 2.2. Due to the large mass of the W boson, the coupling here can be described by an effective coupling constant G_F at energies below the W mass m_W.

$$\sqrt{\Gamma_{\pi^\pm}} \propto G_F = \frac{\sqrt{2} g_w^2}{8 m_W^2} = 1.166 \times 10^{-5}\ \text{GeV}^{-2}, \tag{2.4}$$

where g_w is the "true" weak coupling constant. The square of the effective coupling constant is proportional to the probability for this process to occur and therefore inversely proportional to the lifetime of the pion. Decays via the exchange of lighter particles happen at a faster rate. Therefore the lifetime of the chargeless pion, which can decay electromagnetically, is a lot smaller than the lifetime of charged pions [33]. The dominant decay mode of the chargeless is depicted in figure 2.3.

The square-root of the cross-section of the dominant π^0 decay channel is proportional to $\alpha_{em} = g_{em}^2 \simeq 1/137$. Therefore the partial decay rate has the proportionality and dependence on the exchange particle mass as seen in

$$\sqrt{\Gamma_{\pi^0}} \propto \frac{\alpha_{em}}{(p_{u,d} - p_{\bar{u},\bar{d}})^2 - m_{u,d}^2}. \tag{2.5}$$

Since the mass of the W is four orders of magnitude larger than the quark masses, the lifetime of π^0 is nine orders of magnitude smaller than the $\pi^\pm$ lifetime. Additionally, the mass difference between the decaying particle and its decay products plays a role in the

determination of its longevity. Taking the two-body decay of a particle with mass M into particles with masses m_1 and m_2 as an example, equation 2.6 shows, that for $M \simeq m_1 + m_2$ the decay rate Γ becomes small:

$$\Gamma \propto \frac{[(M^2 - (m_1 + m_2)^2)(M^2 - (m_1 - m_2)^2)]^{1/2}}{M^2} \tag{2.6}$$

To summarise: The lifetime of a particle is determined by the coupling strengths of its decay processes and the size of the phase space of final states[10]. That phase space is determined by the number of allowed decays and the mass difference between the decaying particle and its decay products. In case of a vanishing phase space of final states, the particle is stable.

2.3 Beyond Standard Model theories

Despite its unprecedented success story, the Standard Model fails to describe a handful of particle physics phenomena. Observations of the rotation of galaxies and the cosmic microwave background (CMB) suggest the existence of Dark Matter [6], which shows properties, that it shares with no SM particles. It does not take part in electromagnetic and strong interactions at a significant rate, otherwise it would be visible with modern telescopes and it has a huge abundance, accounting for 26.8% of the energy content of the Universe, which excludes neutrinos as sole Dark Matter candidates.

The same observations of the CMB [6] indicate that Dark Energy, which is an energy form held responsible for the accelerated expansion of the Universe, adds up to 68.3% of the Universes' energy content. This means that the SM only explains the nature of 4.9% of the Universe. Furthermore, Dark Energy seems to be homogeneously distributed across space, suggesting that it interacts very little with SM particles.

Another cosmological observation, which is not explained by the SM is the asymmetry between matter and antimatter in the Universe [34]. A priori there would be no change to the SM processes if positive electromagnetic charges were renamed into negative charges, matter into antimatter[11] and vice versa. Therefore there is no reason for the early Universe to produce more matter than antimatter unless there was a process, which is not yet understood, involved.[12]

Neutrino oscillation is the transition of neutrinos into neutrinos of different flavour, which leads to a periodic dependence of the probability to measure, for example, an electron neutrino in a neutrino beam on the distance from the source of the beam to the location of the measurement. This phenomenon was first observed in the research of solar neutrinos [7] and cannot be described with any SM process and also requires nonzero masses of at least two of the three neutrinos. An explanation of nonzero neutrino masses requires at least an extension[13] of the SM.

One of the most prominent questions left open by the SM is, whether there can be a grand unified theory (GUT) to treat the three fundamental interactions on an equal footing. The unification of the electromagnetic theory with the weak theory far above the electroweak scale, which coincides with the mass of the W boson[14], raises the hope, that such a unification is possible for all fundamental interactions. Through understanding the process of electroweak symmetry breaking it is clear that the weak interaction only seems to have a comparatively small coupling strength, because of the large W mass, which is irrelevant at large energy scales. A similar unification could be possible for the strong interaction as well.

[10] The phase space of final states is the parameter space, which contains all possible final states.
[11] (,left-handed into right-handed)
[12] Of course a universe with perfect matter-antimatter symmetry would be dominated by radiation. There would be no galaxies, planets or sentient beings, who could ask this question.
[13] See for example Seesaw mechanism in chapter 1 of Ref.[10]
[14] See for example Higgs mechanism in chapter 18 of Ref.[30]

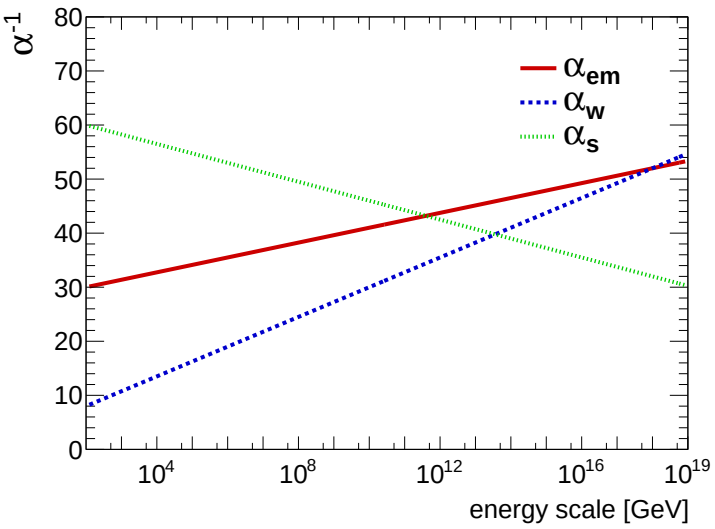

Figure 2.4: Inverse coupling strengths of the three fundamental interactions of the SM depending on the energy scale. Electromagnetic coupling constant α_{em} (red solid line). Weak coupling constant α_W (blue dashed line). Strong coupling constant α_S (green dotted line).

In figure 2.4 an illustration of the problem of grand unification is shown. Taking the energy dependence of the coupling strengths as derived from the SM into account leads to couplings strengths that do not intersect at a single point, which means that there either is no GUT or the high energy behaviour of the couplings strengths is not well understood yet. Furthermore, the unification with the gravitational interaction in a theory of everything (TOE) could be demanded as well. The problem here, also known as the hierarchy problem, is the large gap ($O(10^{32})$) in coupling strengths between the weak interaction and gravity. In addition this would require a quantum field theory of gravity, although quantum effects becoming relevant to gravity is only expected at the Planck scale ($\Lambda_P \simeq 10^{19}$ GeV).

Another problem with the unification at the GUT scale ($\Lambda_{GUT} \simeq 10^{16}$ GeV) or at the Planck scale are the corrections to the mass of the Higgs boson through loop corrections. Because the Higgs boson couples to every massive particle, it can form loop diagrams with each of them, which leads to the fact that the Higgs mass measured in an experiment is not the "true" mass the particle would have without these interactions. Bridging the gap between the electroweak scale and the unification scale would require an excellent fine tuning of the parameters involved to result in a Higgs mass at the order of the electroweak scale as can be seen in

$$m_h^2 = m_0^2 + \frac{3\Lambda^2}{8\pi^2 v^2}\left[(4m_t^2 - 2M_W^2 - M_Z^2 - m_h^2) + O(\log\frac{\Lambda}{\mu})\right], \tag{2.7}$$

where m_h is the measured Higgs mass, m_0 is the bare Higgs mass without loop corrections, v is the Higgs vacuum expectation value, μ is the momentum scale of the experiment and Λ is the cut-off scale of the SM, at which New Physics determines the behaviour of a more general theory than the SM [10]. It could be the grand unification scale[15]. The factor $(4m_t^2 - 2M_W^2 - M_Z^2 - m_h^2)$ corresponds to the one loop corrections from top quark, W, Z and Higgs boson. These are the largest contributions to the one loop corrections, because of the large masses m_t, m_W, m_Z and m_h of those particles. In general the correction through the coupling of a particle to the Higgs is negative for fermions and positive for bosons. To

[15]The value of the unification scale can of course only be determined with certainty, when it and if it is accessible by experiment.

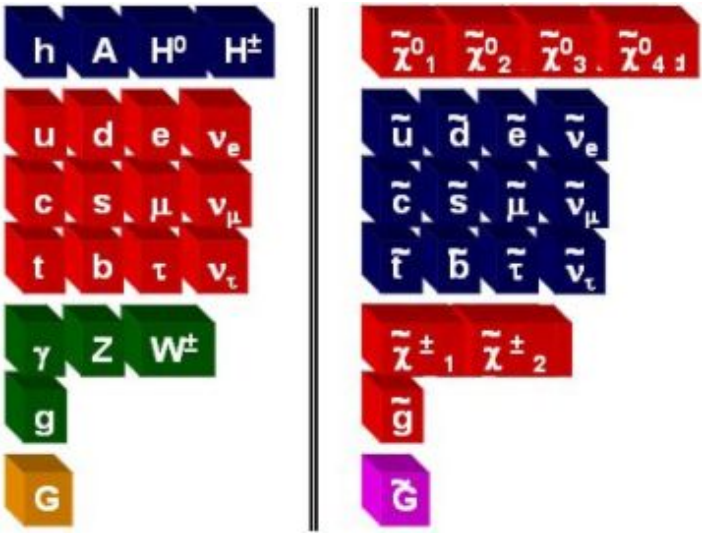

Figure 2.5: Elementary particle content of the Minimal Supersymmetric Standard Model with SM particles on the left side and superpartners on the right [36].

reach consistency with past observations this would require ($m_h^2 \sim 10^4$ GeV^2) = ($m_0^2 \sim 10^{32}$ GeV^2) $- O(10^{32}$ GeV^2), which would be a large coincidence.

To get rid of this problem, either more loop corrections, which cancel the above loop corrections, are required or a cut-off scale far lower than Λ_{GUT} has to be found. Of course this problem can be removed altogether, if one just assumes, that these fundamental constants[16] were just randomly assigned to the Universe. That is however an almost philosophical explanation, which cannot be disproved by experiments. A more scientific approach to solve all of these problems would be the search for a new theory at an energy scale between the electroweak and the Planck scale.

There are numerous Beyond Standard Model (BSM) theories, which commonly involve extra dimensions [15], a hidden sector of particles out of reach of experiments [18] or an additional fundamental symmetry. The prediction of Long-Lived Particles (LLP) is a common characteristic of these new models, especially if the BSM theory is supposed to solve the Dark Matter problem. Since Dark Matter is so abundant and almost not interacting, it has to be long-lived.

2.3.1 Supersymmetry

A common property of BSM theories is Supersymmetry (SUSY). SUSY is a symmetry between bosons and fermions. It is therefore different from the internal symmetries associated with the SM interactions, because it does not commute with Poincaré transformations. If such a symmetry was found in nature in its simplest form, for each SM fermion (boson) there would be a boson (fermion) with exactly the same mass and quantum numbers except the spin, which differs by 1/2. The superpartners of SM fermions are called sfermions (selectron, sneutrino, etc.) and superpartners of SM bosons are named gluino, Wino and so forth. One immediately sees the merit of such a symmetry considering equation 2.7, where the one loop contributions of those particles would cancel the SM loop corrections.

Clearly there are no such superpartners. They were not observed in any past experiment, although they would be just as easily detectable as their SM counterparts. Therefore Supersymmetry can only be realised in nature with a SUSY breaking mechanism pushing the superpartners to a higher mass scale.

[16]The Standard Model has 19 free parameters, which is a high number for the taste of many scientists [10].

In figure 2.5 the elementary particles of the minimal supersymmetric Standard Model (MSSM) are shown. On the left side in addition to the well-known SM particles there is an extended Higgs sector[17]. The right side of the figure shows the superpartners after mixing. As in the SM particles with equal quantum numbers can mix to form mass eigenstates different from the interaction eigenstates. In the SUSY sector there are more possibilities for particle mixing, because the superpartners of the Higgs particles have the same spin (1/2) as the superpartners of the electroweak bosons. The mass eigenstates resulting from this mixing are neutralinos and charginos[18].

As a substitute for baryon number and lepton number conservation a number BSM theories including SUSY introduce R-parity conservation with the multiplicative R-parity P_R defined in

$$P_R = (-1)^{3(B-L)+2s}, \tag{2.8}$$

where the baryon number B equals $\pm 1/3$ for each quark (antiquark), the lepton number L equals ± 1 for each lepton (antilepton) and s is the spin of the particle. Assuming R-parity conservation makes it possible to allow the consistency with proton-stability among other past observations without artificially removing many possible SUSY processes from the theory or adding both baryon number and lepton number conservation to the theory. From the definition it follows that for all SM particles $P_R = +1$ and for all superpartners $P_R = -1$. Therefore SUSY particles can only be produced in pairs from an initial state consisting of SM particles. Because of R-parity conservation the lightest supersymmetric particle (LSP) would be stable.

If any of the supersymmetric particles are long-lived they have the possibility to form bound states with SM particles. In this sense colour-charged superpartners can be partons of the so called R-hadrons. An R-hadron has similar properties as a hadron except one or more of its partons are replaced by their superpartners.

In the following four of the most important BSM theories, which assume SUSY, are presented briefly.

Minimal Supersymmetric Standard Model

The Minimal Supersymmetric Standard Model (MSSM) was designed as a minimal extension of the SM with a Lagrangian[19] invariant under the SUSY transformation. As such of all the extensions of the SM, which include SUSY, it has the least amount of predicted new particles. The MSSM still introduces 105 additional free parameter, which can be related by arguments of underlying physics to reduce their number significantly. The free parameter space is however still large enough to allow nearly degenerate mass spectra. Therefore the MSSM predicts aside from a stable LSP possibly a long-lived next-to-lightest supersymmetric particle (NLSP).

Supergravity

An attempt to generalise SUSY and include gravity as the fourth fundamental interaction is Supergravity (SUGRA)[20]. Compared to the MSSM, SUGRA reduces the number of free parameters to only 5 by making assumptions about physics just below the Planck scale. In SUGRA the gravitino, the superpartner of the graviton, could be the LSP, therefore stable and an ideal Dark Matter candidate.

[17] This is needed to avoid gauge anomalies as is elaborated in the introduction of Ref.[35]

[18] More on SUSY mixing in chapter 8 of Ref.[35]

[19] The Lagrangian is a term, which contains all energy contributions to and therefore all interaction of a given theory. It is designed to be invariant under all symmetry transformation of the theory. The Lagrangian is used to derive equations of motions and rules to construct Feynman diagrams [30]

[20] See for example chapter 6 of Ref.[10].

LeptoSusy

Another possible scenario of SUSY is the so called Leptogenic Supersymmetry [14] (LeptoSUSY). The name refers to a typical particle spectrum, predicted by several different BSMs. Its main characteristic is the high number of leptons produced in cascade decays. LeptoSUSY predictions also include the existence of long-lived sleptons.

SplitSUSY

In the split Supersymmetry [12] (splitSUSY) scenario the mass spectrum of the superpartners is split into light fermions at an energy scale not far above the electroweak scale and far heavier bosons. In this scenario gluinos would be long-lived and their lifetime would be a measure of the mass scale of the superpartners of the SM fermions.

2.3.2 BSM without Supersymmetry

The introduction of a symmetry between bosons and fermions is no necessity for a consistent BSM theory as the following two examples among many others show.

Universal extra dimensions

Models predicting universal extra dimensions [15] (UED) work under the assumption that there are more than four spacetime dimensions. These extra dimensions would be so small and possibly circular that they cannot be observed at low energies. UED can be an underlying framework to explain SUSY breaking, but is actually a more general concept [37]. The concept leads to a prediction of a number of mass states (Kaluza-Klein modes) [38]. The lightest of these is expected to be stable.

Hidden valley Models

The assumption behind the hidden valley models is the existence of a hidden sector of particles, which couple weakly to SM particles. This coupling would be mediated by an ultraheavy particle. Additionally, these models predict a valley of low mass states called v-states. In case these v-states can only decay into SM particles, they are long-lived because of the small coupling [18].

An example model including both a hidden sector and SUSY is gauge-mediated supersymmetry breaking (GMSB). Here the hidden sector is an explanation for high masses of superpartners compared to their SM counterparts.

2.4 Stable, massive particles

The term "stable particle" in the context of collider experiments requires the particle to have at least a mean path length of the order of 10 m before its decay. In that sense the particle is called detector-stable, if it is able to leave the detector, before it decays. The minimal lifetime for detector-stability therefore depends on the properties of the experiment, which is described in section 3.1. In that sense detector-stable particles are particles with exceptionally long lifetimes, which may or may not be actually stable.

SM examples for detector-stable particles are listed in table 2.2. They include elementary particles like electrons, muons, photons and neutrinos as well as hadrons like protons, neutrons and neutral long-lived kaons. Charged pions and kaons are listed as well, although they fall just short of detector-stability. Additionally, there are gluons and light quarks, which hadronise quickly [32] to possibly form detector-stable hadrons. Of course the SM also includes stable atomic nuclei, atoms and even more complex structures build out of atoms. However, the

Table 2.2: Detector-stable SM particles and their lifetimes τ in s [26].

Stable		Metastable	
Name/Symbol	Lifetime	Name/Symbol	Lifetime
Electron e^-	∞	Muon μ^-	2.20×10^{-6} s
Proton p	∞	Neutron n	880 s
Neutrino $\nu_{e,\mu,\tau}$	∞	Charged Pion $\pi^\pm$	2.60×10^{-8} s
		Charged Kaon $K^\pm$	1.24×10^{-8} s
		Long-lived Kaon K_L^0	5.12×10^{-8} s

production of atomic nuclei in collider experiments is very unlikely, because it would require a large number of elementary particles with similar momenta to form such a complex bound state. Aside from atomic nuclei the masses of stable SM particles range from 0 (photon) to 940 MeV (neutron), which is light compared to the electroweak scale ($\simeq$ 100 GeV).

The masses of stable and long-lived particles predicted by BSM theories might be orders of magnitudes larger than that. The path length of a particle within its mean lifetime τ is the mean path length, which can be approximated by $c\tau$. Because the mean path length depends not only on the lifetime of the particle, but also on its velocity, the term detector-stability cannot be defined by the lifetime alone. Whether the approximation that the mean path length roughly equals $c\tau$ is accurate for long-lived SM particles or even long-lived new particles, depends on the typical energy scale of the experiment in question. Furthermore, there could be a clear distinction between stable SM particles and Stable, Massive Particles (SMP), which can be determined by a velocity measurement.

At high-energy physics (HEP) experiments relativistic effects play an important role. As such both the lifetime and the mean path length depend not only on the properties of the particles, but also on the reference frame. One of the first experiments to measure this effect was based on the measurement of muon decays [39]. In this experiment the muon abundance at a given distance was higher than expected without relativistic effects. The reason for this is that the distance is shortened in the reference frame of the muons according to

$$l = \frac{l_0}{\gamma}, \tag{2.9a}$$

$$t = t_0 \cdot \gamma, \tag{2.9b}$$

$$\gamma = \frac{1}{\sqrt{1-\beta^2}}, \tag{2.9c}$$

$$E^2 = m^2 + p^2 = \gamma^2 m^2, \tag{2.9d}$$

where l is the contracted distance in the reference frame of the muons, l_0 is the distance measured by the observer at rest compared to the muons moving with speed β, t is the elongated time in the muon reference frame and t_0 is the time in the laboratory frame. γ is called Lorentz factor and the transformations describing the relation between reference frames, which differ by a constant velocity β are called Lorentz transformations. E, p, and m are energy, absolute value of the three momentum and mass of the particle.

Chapter 3

Experimental methods

3.1 The Large Hadron Collider

The Large Hadron Collider (LHC) is a circular particle collider build for proton–proton and heavy-ion collisions at record centre-of-mass energies ($\sqrt{s}$) and luminosities. In the LHC two particle beams divided into several particles bunches are accelerated to equal kinetic energies. The luminosity L is defined via its relation to the number of particle collisions (events) N_{event} and the cross–section σ of the studied process:

$$N_{event} = \sigma \int L \mathrm{d}t. \tag{3.1}$$

The luminosity depends solely on the properties of the beam (number of particles per bunch N_b, number of bunches in the beam n_b, revolution frequency f_{rev}, gamma factor γ, normalized transverse beam emittance ϵ_n and beta function at the collision point β^*) and is independent from the processes under study [40]. It can be expressed as

$$L = \frac{N_b^2 n_b f_{rev} \gamma}{4\pi\epsilon\beta^*} F(\theta_c; \sigma_z, \sigma^*). \tag{3.2}$$

Here F is the geometric luminosity reduction factor, which is needed, since the bunches with length σ_z and width σ^* do not collide head on, but rather under the crossing angle θ_c.

Currently the highest centre-of-mass energy reached by the LHC is 13 TeV and therefore just 1 TeV below the design energy. The main detectors working with LHC beams are LHCb (Large Hadron Collider beauty experiment), ALICE, and the multi-purpose detectors ATLAS and CMS. The main accelerator was built into the existing tunnel of the LEP (Large Electron Positron Collider) experiment and the injectors use the structure of older accelerators like the SPS (Super Proton Synchrotron), for example.

This work uses both data taken at $\sqrt{s} = 8$ TeV and data taken after the long shutdown at $\sqrt{s} = 13$ TeV. At $\sqrt{s} = 8$ TeV the LHC delivered an integrated luminosity of $\int L\mathrm{d}t = 22.8\ \mathrm{fb}^{-1}$ and ATLAS recorded $\int L\mathrm{d}t = 20.3\ \mathrm{fb}^{-1}$, which were good for physics [41]. The $\sqrt{s} = 13$ TeV-data used in this work amounts to $\int L\mathrm{d}t = 113\ \mathrm{pb}^{-1}$ delivered and $\int L\mathrm{d}t = 85\ \mathrm{pb}^{-1}$ good-for-physics data. The total integrated luminosity recorded by day in 2012 at 8 TeV and in 2015 up to the end of July at 13 TeV can be seen in figure 3.1.

3.2 The ATLAS detector

The ATLAS detector [43] is one of two general purpose-detectors operating at the LHC, the other one being CMS. It is designed to collect collision data from proton–proton collisions at a centre-of-mass energy of up to 14 TeV and up to luminosities as high as $10^{34}\ \mathrm{cm}^{-2}\mathrm{s}^{-1}$. Another purpose is data taking from heavy-ion collisions with a centre-of-mass energy as high

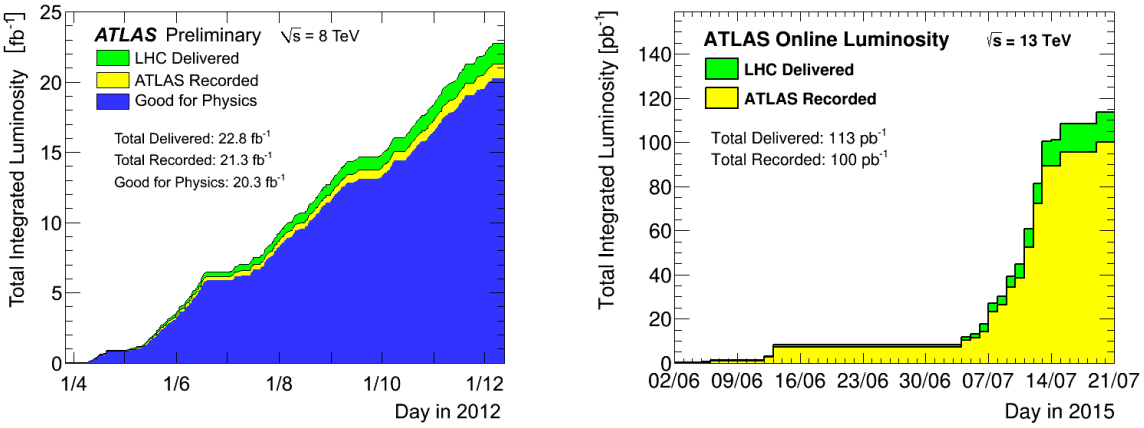

Figure 3.1: Integrated luminosity per day at $\sqrt{s} = 8$ TeV [41] (left) and integrated luminosity per day at $\sqrt{s} = 13$ TeV [42] (right).

as 2.8 TeV per nucleon and 10^{27} cm^{-2}s^{-1} design luminosity. The peak luminosity at the peak energy of 13 TeV for data taking up until July 2015 was 1.6×10^{33} cm^{-2}s^{-1} for proton-proton collisions [42].

Fields of research range from precision measurements of SM parameters to searches for new particles. Therefore the detector is equipped with the ability to measure tracks, energies, charges and many other properties of almost[1] all particles. Rapidly decaying particles are detected via their daughter particles. The basic principle of particle detection and identification works via the use of several subdetectors, which are each especially efficient in measuring certain particle properties or are optimised for the detection of certain particles. Thus the electromagnetic calorimeter is designed to absorb light particles, which interact electromagnetically, such as electrons and photons, the hadronic calorimeter does the same for hadrons like charged pions, protons and neutrons. Muons typically pass through most of the detector. The measurement of their properties is improved with the muon spectrometer. With the ATLAS detector tracks and energy deposits are measured, from which particle and jet four-momenta can be constructed. Due to a 2 T magnetic field in the inner detector, particle tracks can be used to distinguish between positive, negative and neutral electromagnetic charges, which contributes to the identification of the particle.

A schematic of the ATLAS detector can be found in figure 3.2. The detector with its toroidal shape and forward–backward symmetry was constructed such, that the beam-pipe coincides with its central axis. The origin of the ATLAS coordinate system is defined as the nominal interaction point. The positive x-direction points towards the centre of the LHC ring, the positive y-direction points upward and the z-direction follows the beam-pipe in a right-handed coordinate system. Azimuthal angle ϕ and polar angle θ are measured around the z-axis and from the z-axis respectively. The toroid has an eightfold symmetry in the ϕ-direction as well as a mirror symmetry with respect to the x–y-plane, where $z = 0$. Other important quantities are the pseudorapidity $\eta = -\ln\tan(\theta/2)$, the distance $\Delta R = \sqrt{\Delta\eta^2 + \Delta\phi^2}$ and the distance to the centre of the beam pipe in the x–y-plane $r = \sqrt{x^2 + y^2}$. For highly relativistic particles the pseudorapity is a good approximation of the rapidity $1/2\ln(E + p_z/E - p_z)$ and differences between two rapidities are invariant under Lorentz boosts along the beam axis. This means that the definition of ΔR allows for a measure of the spatial separation of two particle tracks without knowing the exact velocity of the interacting partons of the colliding protons.

More detailed descriptions of inner detector (section 3.2.1), electromagnetic and hadronic

[1] Neutrinos and possibly a number if new particles are invisible to the ATLAS detector.

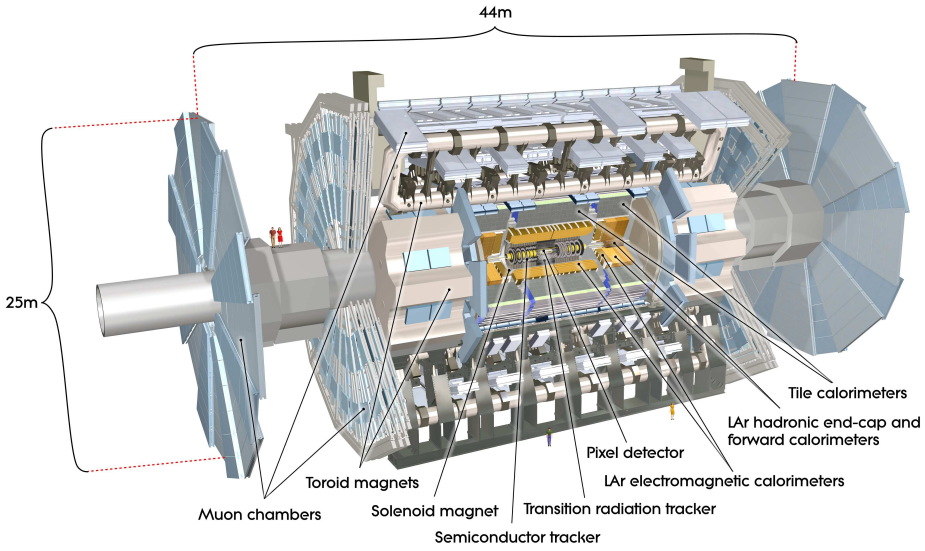

Figure 3.2: Schematic of the ATLAS detector with the inner detector, the calorimetry and the muon system [43].

calorimeter (section 3.2.2) as well as muon spectrometer (section 3.2.3) are given below. Additionally, the functionality of the ATLAS trigger system (section 3.2.4) is discussed.

3.2.1 Inner detector

The general purpose of the inner detector is the measurement of momenta of traversing charged particles inside a 2 T solenoidal magnetic field as well as the resolution of primary and secondary collision points (vertices). It is of cylindrical shape with 1.150 m radius and 7.024 m length. A schematic of the inner detector can be found in figure 3.3.

The inner detector is the first layer around the beam-pipe ($r < 34.3$ mm). It contains three parts: The pixel detector [44] ($r < 122.5$ mm), the semiconductor tracker consisting of silicon-microstrip sensors [45] (SCT, $r < 514$ mm) and the transition radiation tracker [46] (TRT, $r < 1066$ mm). The subdivided design was chosen to optimise cost, resolution and radiation tolerance.

Pixel detector

The pixel detector system provides the ATLAS experiment with charged-particle tracking. Its main function is the reconstruction of primary vertices as well as the identification and reconstruction of secondary vertices. The 1744 pixel modules with a total number of pixels equal to 80.4×10^6 are arranged in three layers. The pixel detector is located within 122.5 mm distance from the centre of the beam-pipe within an envelope with radius $r = 242$ mm and three layers of end-cap disks. With this design a charged track hits the pixel detector at three different points.

Semiconductor tracker

The SCT is divided into four layers in the barrel region ($|\eta| < 2.5$) and nine layer in each disk. The tracker is built out of 15912 sensors and has a similar purpose as the pixel detector. With a stereo angle of 40 mrad between two strips, the SCT reaches a resolution of 16 μm for $\eta \sim 0$.

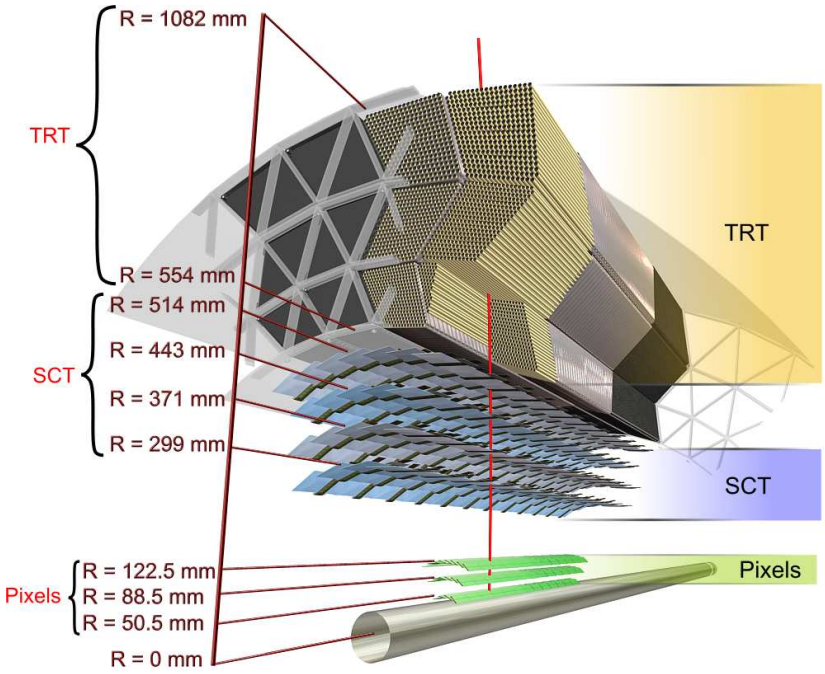

Figure 3.3: Schematic of the barrel inner detector consisting of the pixel detector, the SCT, the TRT and a single charged track (red line) [43].

Transition radiation tracker

Using polyamide proportional drift tubes (straws) the TRT registers hits of charged particles in a gas mixture consisting of Xe, CF_4 and CO_2 (70% Xe). As such this part of the inner detector is able to resolve tracks, because a traversing particle can ionise gas molecules in the TRT and the secondary electrons, which are produced in this ionisation, are accelerated in the TRT and deposit their charge at the anode wire. In the low pseudorapidity region ($|\eta| < 2$) particles cross between 35 and 40 straws allowing a track resolution of the order of up to 10 μm. The TRT is used for electron identification by detecting their transition radiation in the gas mixture.

3.2.2 Calorimetry

In figure 3.4 the calorimeter system of the ATLAS detector is shown including the electromagnetic (EM) calorimeter ($r < 2$ m) surrounded by the hadronic calorimeters ($r < 4.25$ m). The calorimetry was designed mainly for the measurement of energies of particles as well as for jet reconstruction resulting from the hadronisation of colour-charged particles.

A good momentum measurement can even provide information about particles, which are undetectable by the experiment via the quantity $\vec{E}_T^{miss}$. In the ATLAS experiment[2] the missing transverse momentum $\vec{E}_T^{miss}$ is defined via

$$\vec{E}_T^{miss} = -\sum_i \vec{p}_{T,i}, \tag{3.3}$$

where $\vec{p}_{T,i}$ is the projection of the momentum of the ith particle or jet to the plane transverse to the beam axis i.e. the x–y-plane. The missing transverse energy E_T^{miss} is defined as the magnitude of the missing transverse momentum [47]. In collider experiments with elementary particles[3] the momenta of the colliding particles in the laboratory frame of reference add up

[2] and other collider experiments
[3] For example e^+e^- colliders like the LEP.

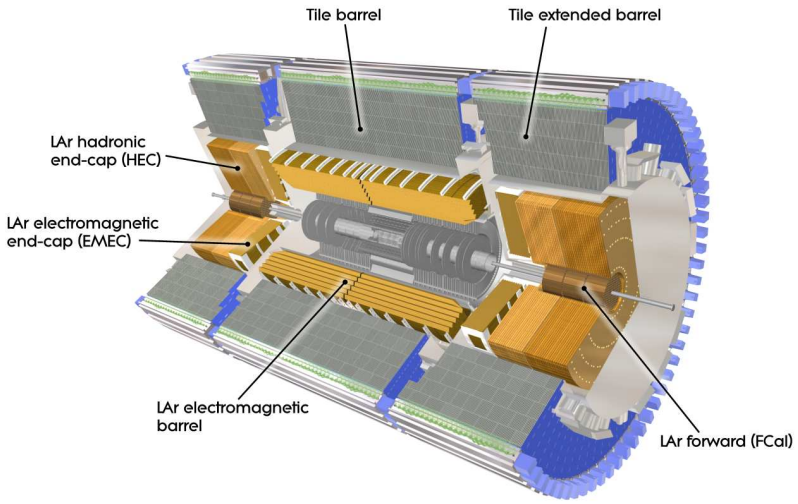

Figure 3.4: Schematic of the ATLAS calorimetry with electromagnetic calorimeter and the hadronic calorimeters [43].

to zero. This means, that due to Poincaré invariance the momenta of the final state particles have to add up to zero as well. Therefore the reason for any deviation from a vanishing momentum sum has to be the presence of undetectable particles or mismeasurement. For colliding hadrons however the momentum along the beam axis of each parton is less clear because of parton–parton interactions inside the hadron. The total momentum transverse to the beam axis equals zero though, so the missing momentum transverse to the beam axis can be used as an almost equivalent quantity.

Since muons lose only a small amount of kinetic energy in the calorimeters the momenta reconstructed in the muon spectrometer are added to the transverse momentum as well.

Electromagnetic Calorimeter

The barrel EM calorimeter is a Pb-liquid Ar calorimeter built out of accordion-shaped copper electrodes and lead absorbers imbued in liquid argon (LAr). The accordion shape avoids discontinuities in the ϕ-direction. The purpose of the EM calorimeter is the measurement of the properties of light electromagnetic particles (electrons, positrons and photons). Incoming particles can ionise the active material LAr, which due to the large electric field between electrons and absorbers leads to an acceleration of secondary electrons, which in turn leads to a pulse signal in the electrodes. For $|\eta| < 2.5$ the modules of the EM calorimeter each consist of three layers, the innermost of which is divided into fine segments, which allows for a good momentum direction measurement.

Hadronic Calorimeters

There are three hadronic calorimeters: The hadronic barrel scintillator-tile calorimeter (tile calorimeter) [48] directly outside the EM calorimeter, the hadronic end-cap calorimeter (HEC) consisting of two wheels behind the end-caps of the EM calorimeter and the LAr forward calorimeter (FCal), which is enveloped by the end-cap of the EM calorimeter and the HEC. The hadronic calorimeters are optimised for energy measurements of objects, which experience the strong interaction like hadrons and jets. The hadronic calorimeters are designed to fully contain hadronic showers. The tile calorimeter is divided into a barrel region and two extended barrel regions.

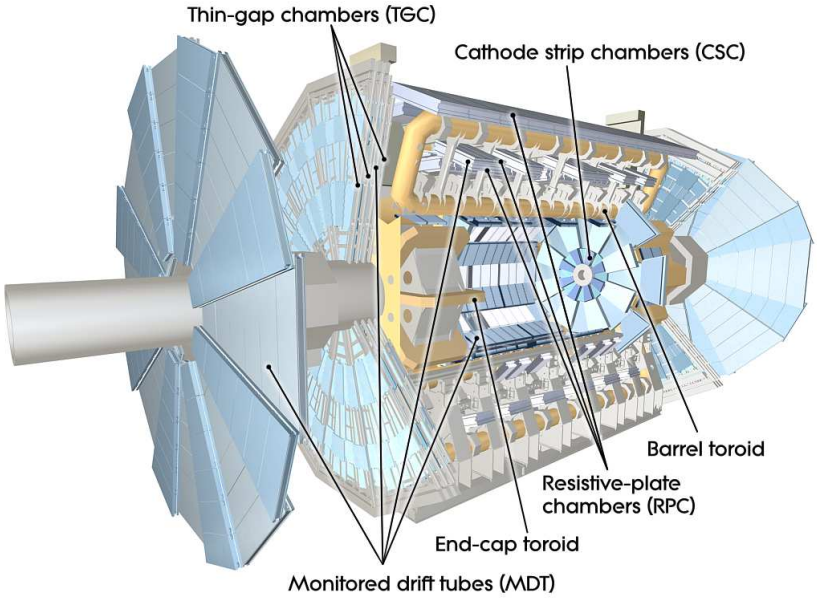

Figure 3.5: Schematic of the ATLAS muon spectrometer, which contains thin-gap chambers, cathode strip chambers, monitored drift tubes, resistive plate chambers and the superconducting toroid magnet [43].

3.2.3 Muon spectrometer

The muon system of the ATLAS detector is shown in figure 3.5. It is the outermost region of the detector and therefore extends to $r = 12.5$ m in the barrel region and $|z| = 22$ m in the end-cap regions. The muon system contains thin-gap chambers (TGC), cathode strip chambers (CSC), monitored drift tubes chambers (MDT), resistive-plate chambers (RPC) and superconducting toroid magnet coils. The muons system is designed to measure energies as well as momenta and to reconstruct tracks of muons or charged muon-like particles, which traverse the rest of the detector without depositing all their kinetic energy.

The MDTs consist of chambers with between three and eight layers of drift tubes performing the precision momentum measurement. CSCs are used in the forward region ($2 < |\eta| < 2.7$) for tracking, measuring positions from induced-charge distributions. To allow for reliable capability to trigger[4] on muon tracks RPCs are used in the barrel region ($|\eta| < 1.05$) and TGCs in the end-cap region ($1.05 < |\eta| < 2.4$). Both RPCs and TGCs provide track information shortly ($O(10$ ns$)$) after the particle passed through them.

3.2.4 Trigger

At the LHC the proton bunches crossed at a rate of 20 MHz, which was increased to 40 MHz during data taking in 2015. In each bunch crossing there are on average 23 proton–proton collisions at the design luminosity $L = 1 \times 10^{34}$ cm^{-2}s^{-1}. Considering the fact that each event leads to ~ 1.5 Mbyte of data, this results in the production of data on a Pbyte/s scale. This is far more than any practical storage system can handle. To meet that challenge the ATLAS detector uses a multi-level trigger system, which preselects only a comparatively small number of the events produced in the detector.

For practical permanent storage an event rate of only a few hundred Hz is required, which means that only one in about 10^7 events is not rejected by the trigger system. To still be sensitive to New Physics, the triggers cannot select events at random, but rather have to use

[4]See next section for a description of the ATLAS trigger system.

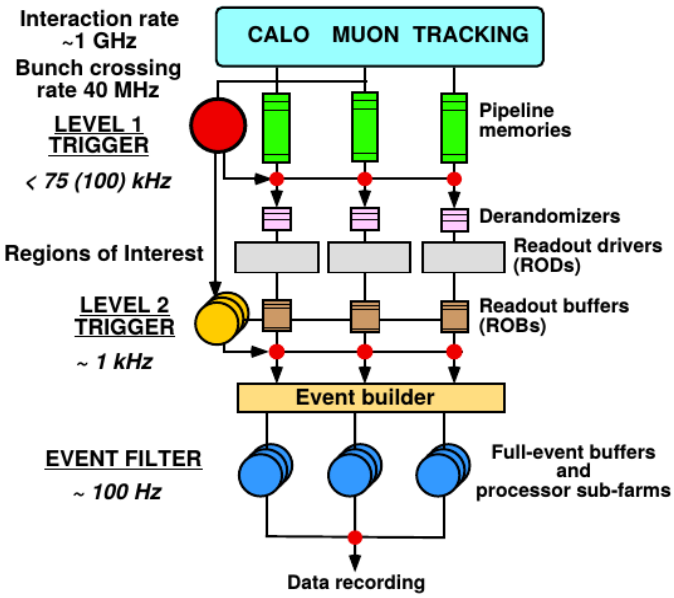

Figure 3.6: Schematic of the ATLAS trigger system: The event selection is divided into fast L1 triggers (red), L2 triggers (yellow) and EF (blue) [22].

the acquired data to distinguish between potentially interesting and other events.

The event selection is divided into level 1 (L1) triggers [22], level 2 (L2) triggers and event filter (EF). The L1 triggers are based on hardware, while both the L2 triggers and the EF, which are also called high level triggers (HLT) [23], are software-based. The L1 triggers work with very simple trigger algorithms and without complete detector information selecting events at rates below 75 kHz. The L2 trigger output rate is on the order of 1 kHz and the EF finally reduces the event selection rate to the required value. In figure 3.6 a schematic of the ATLAS trigger system is shown.

After the L1 trigger decision, the selected events are temporarily stored in readout buffers (ROB) after being evenly distributed into readout drivers (ROD) by intermediate buffers (derandomizers). Until the L2 event selection the data is held in the ROBs. The L2 trigger decision uses the information from certain η–ϕ regions of the detector for the reconstruction of jets and tracks. These regions-of-interest (RoI) are defined by the L1 trigger to use only relevant data for the event selection. In the final step, the EF uses full detector event information for the trigger decision.

Only events that meet certain requirements are selected. In that sense the trigger decision is based on the question, whether a so called trigger variable exceeds a certain threshold. Trigger variables used by the ATLAS experiment include but are not limited to the p_T of at least one muon object in the event above a given threshold, a number of jets with an E_T above a required value or E_T^{miss} of at least a given value. There can also be additional requirements on the event topology or more complicated algorithms at least for the HLTs. Typically the L1 trigger thresholds are lower than the HLT thresholds and the trigger decision becomes more sharpened at higher trigger levels decreasing the selection uncertainty. This is due to the fact that the HLTs have both more time and more information to build the trigger decision.

An important property of a trigger is its efficiency, which is the number of events passing the trigger divided by the number of all events. If a trigger exceeds a required maximum rate a prescale factor is chosen. Therefore for a trigger with the prescale factor n only $1/n$ of the events are randomly chosen to be kept. This ensures that the rate, at which events pass at least one of all the triggers, does not exceed 200 Hz.

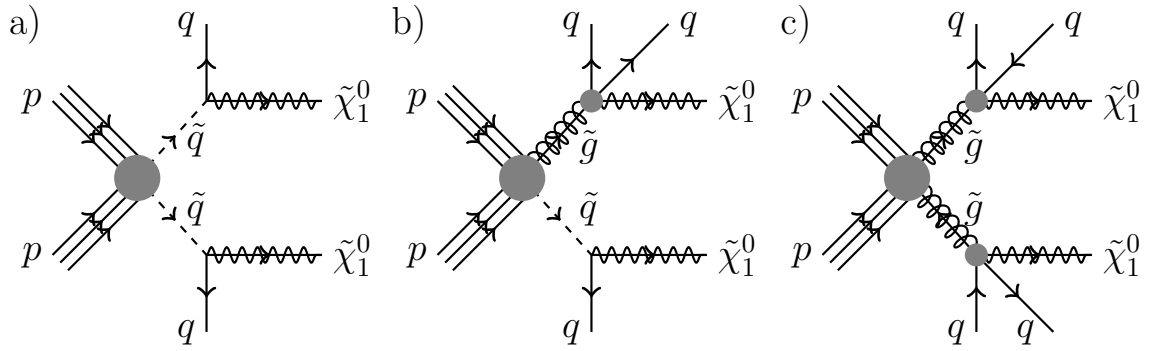

Figure 3.7: Pair production of colour-charged SMPs in LeptoSUSY Models. a) Squark pair production. b) Production of a gluino and a squark. c) Gluino pair production. Decay of each squark into a neutralino and a quark. Decay of each gluino into a neutralino and two quarks.

3.3 Stable, massive particles in the ATLAS detector

As mentioned in section 2.4 SMPs predicted by BSM theories can have far greater masses than detector-stable SM particles. Therefore SMPs produced in LHC collision-events are expected to have velocities far smaller than 1, which discriminates them from every SM particle. This means that SMPs are an excellent hint to New Physics. Examples for SMPs, their production mechanisms and signatures in the ATLAS detector are discussed below.

3.3.1 *R*-hadrons

If the lifetime of a new colour-charged particle is longer than the hadronisation timescale it will together with SM particles form a colourless multiparton state called R-hadron. The most promising candidates for supersymmetric partons of R-hadrons are sbottoms and stops, the scalar superpartners of heavy quarks, as well as gluinos the superpartners of gluons. Assuming R-parity conservation these particles like any supersymmetric particle can only be produced in pairs or together with a different supersymmetric particle.

The production of a) a squark pair, b) a gluino and a squark as well as the production of c) a gluino pair are shown in figure 3.7. The squarks each decay into a neutralino and a quark, while the gluinos can decay into a neutralino and two quarks or a neutralino and a gluon. The three-body gluino decay happens via the exchange of a heavy intermediate particle in this case. At low energies this can be approximated by a four point interaction. (See also section 2.2). These production modes are possible, for example, in LeptoSUSY Models. If the masses of the gluino/squark and the neutralino are degenerate the gluino/squark is long-lived or even detector-stable. The large mass of the intermediate particle increases the stability of the gluino. In general the supersymmetric particles are produced back-to-back, i.e. with opposite momenta.

The R-hadron has similar properties as the equivalent hadron except the spin differs by 1/2 and the mass is up to several orders of magnitude larger. Considering, for example, a gluino R-hadron consisting of a gluino ($m_{\tilde{g}} = 1$ TeV), two up-quarks and one down-quark as valence quarks, the particle mass is dominated by the gluino mass. This is in contrast to the proton, which has a mass, that is dominated by its binding energy. The electromagnetic charge is +1 and the spin equals 1 or 0. This means the R-hadron track is bent by a magnetic field and, due to its large mass compared to the atoms of the detector, scattering in the calorimeter is very inefficient. This leads to a muon-like track and not, as may be intuitive, a proton-like track, which would end in the calorimeter. Not only for this example R-hadrons

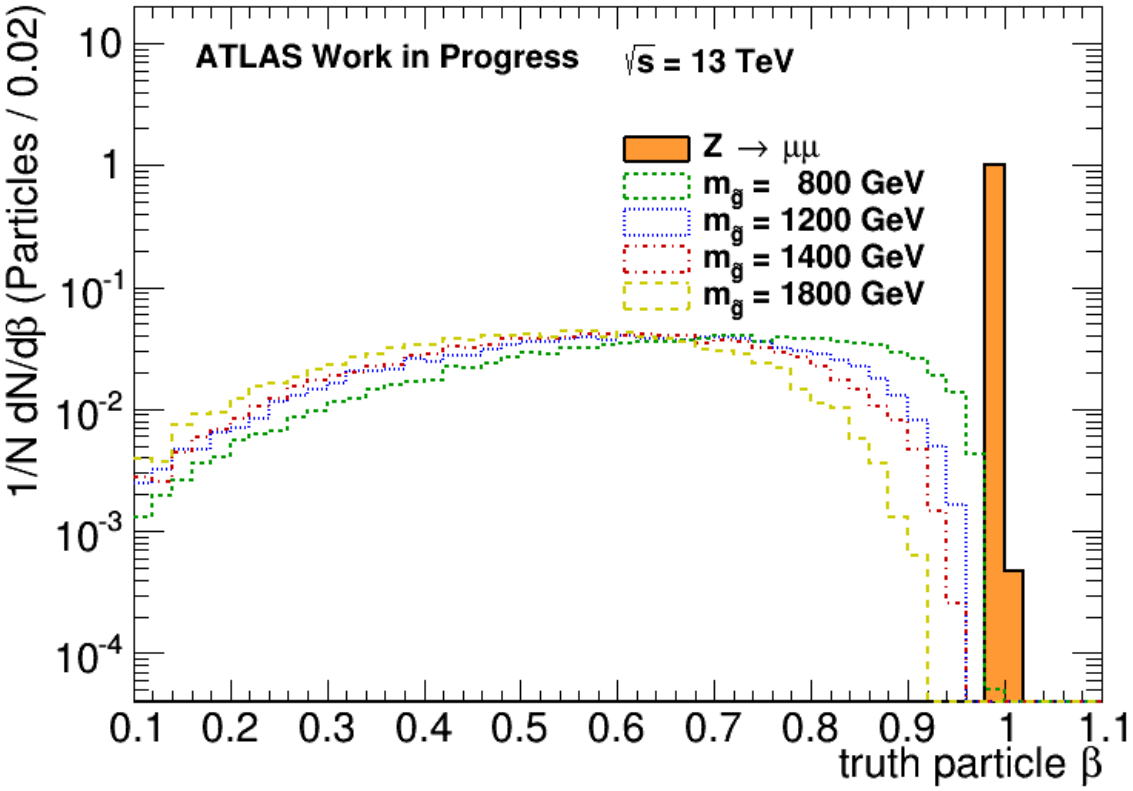

Figure 3.8: Velocity distributions of pair produced gluinos with different masses simulated at 13 TeV centre-of-mass energy. $m_{\tilde{g}} = 800$ GeV (green dashed line), $m_{\tilde{g}} = 1200$ GeV (blue dotted line), $m_{\tilde{g}} = 1400$ GeV (red dash dotted line) and $m_{\tilde{g}} = 1800$ GeV (yellow long dashed line). Comparison to a velocity distribution for muons from $Z \to \mu\mu$ events (black solid line with orange filling). The number of events of each dataset is normalised to one.

can leave the detector without depositing all of their kinetic energy.

The interactions between the SM constituents of the R-hadron and the detector material are however very efficient, because both interact through the strong interaction over small distances. Going back to the example of the proton-like gluino R-hadron. The particle can exchange, for example, an up-quark with a down-quark of the detector material, leading to a change of the electromagnetic charge or a "charge-flip". This can happen multiple times leading to R-hadron tracks, which are bent in different directions or disappearing in the calorimeter. This makes it challenging to associate tracks in the muon spectrometer with inner detector tracks. Therefore a muon-spectrometer-agnostic search was developed for the search for SMPs [24].

Considering equation 2.9 a particle with a given energy has a lower kinetic energy, the larger its mass is. A detector-stable R-hadron can therefore deposit all of its kinetic energy in the detector through SM constituent interactions. It can then be stopped in and bind with the detector material. This stopped R-hadron may then decay minutes, hours or even years later, leading to out-of-time[5] jets in the outer layers of the detector.

Considering for example models, in which the long-lived but not detector-stable SUSY parton of the R-hadron is the NLSP and the LSP is a Dark Matter candidate, which therefore interacts only weakly with SM particles, the R-hadron can decay into particles that are invisible to the detector.

[5]Out-of-time means "not during the event, in which the new particle was produced".

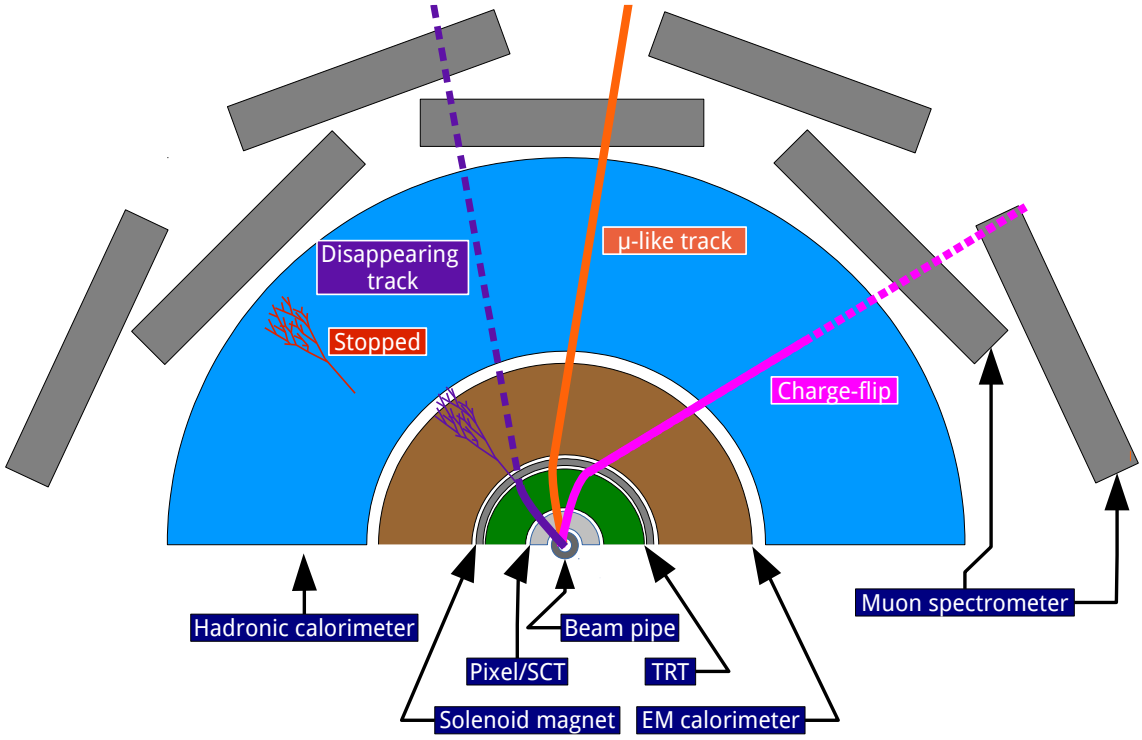

Figure 3.9: Signatures of R-hadrons in the barrel region of the ATLAS detector. Late decaying R-hadron after being stopped multiple events earlier (red). Charged R-hadron (violet) decaying into a particle undetectable with the ATLAS detector (violet, dashed). Charged R-hadron with a muon-like track (orange). Charged R-hadron (magenta). Uncharged R-hadron after a charge-flip (magenta, dotted).

How slow detector-stable R-hadrons can be is depicted in figure 3.8[6], where velocity distributions of a number of Monte Carlo (MC) simulated pair-produced gluinos are shown in comparison to a muon velocity distribution. While a large fraction of the muons have velocities near the speed of light, the mean of the gluino velocities decreases with increasing particle masses. This leads to some unique properties. For example, in a proton beam with 50 ns bunch spacing a stable R-hadron with $\beta = 0.5$ has a distance of ~ 15 m from the interaction point 100 ns after its production. That is the same distance a muon with $\beta \simeq 1$ produced in the next bunch crossing has from the interaction point 50 ns after the production of the muon. This would lead to missing transverse energy in the first bunch crossing and the detection of two muons (one out-of-time muon) in the second bunch crossing. There would however in general be no overall E_T^{miss}, because the supersymmetric particles are in most cases produced back-to-back, leading to a cancellation of the E_T^{miss}-contributions. In figure 3.9 the, for this work, most interesting signatures of R-hadrons are summarised. It is important to note that a charged particle has a bent track in the muon spectrometer. The track is however bent perpendicular to the x–y-plane, which cannot be seen from figure 3.9.

From cosmological observations the stable gluino is excluded to be heavier than a few TeV [21]. Therefore the search for stable gluinos with the ATLAS detector is potentially within reach to exclude the stable superpartner of the gluon completely or discover it. The current exclusion limits for detector-stable gluino-, sbottom- and stop-R-hadrons are up to 1274 GeV, 780 GeV and 899 GeV respectively [24].

[6]See section 4 for a description of the used datasets.

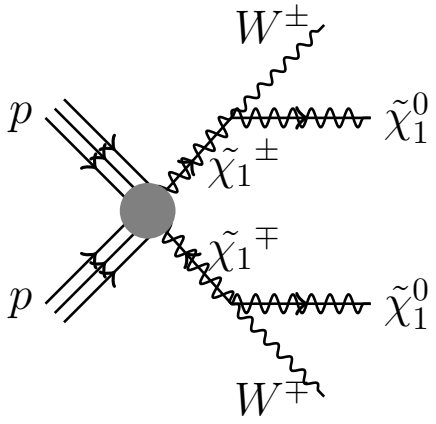

Figure 3.10: Electroweak pair production of charginos, which decay after a possibly large amount of time into W bosons and neutralinos.

3.3.2 Charginos

Charginos ($\chi_{1,2}^{\pm}$) are superpositions of the superpartners of charged $P_R = 1$ bosons namely the charged Higgs bosons and the W bosons. In figure 3.10 one of many examples of production mechanisms of a chargino pair is depicted. The W bosons in the final state will quickly decay hadronically, producing jets, or leptonically, leading to a lepton signature and missing transverse energy. If the charginos are detector-stable, this decay would however take place outside the detector.

The exclusion limits for long-lived charginos almost degenerate to the lightest neutralino are currently at 619 GeV [24]. This means, that a detector-stable chargino too would be heavy and a lot of the properties of long-lived, charged R-hadrons are properties of long-lived charginos too. Muon-like tracks are common to charginos as well, because of inefficient scattering with the detector material. The low velocity of the charginos leads to out-of-time E_T^{miss}, which is canceled, because the chargino pair is typically produced back-to-back. If the lifetime of the chargino is short enough[7] it can decay into invisible particles, neutralinos in the above example, inside the detector leaving a track only in the inner detector (inner detector and calorimeter), but not in the calorimeter and muon spectrometer (muon spectrometer). Other than the slepton (See next section) the chargino can also be produced together with a neutralino leading to only one muon-like track.

Other than squarks and gluinos, charginos are not colour-charged, which means they do not hadronise and do not form bound states. This excludes strong interactions with the detector material and therefore large energy losses. This means the long-lived chargino can typically not be stopped and decay later in the detector.

3.3.3 Sleptons

In Figure 3.11 a Feynman diagram of the direct production of $\tilde{\chi}_1^0\tilde{\chi}_1^{\pm}$ decaying into stable staus and leptons is shown. The stau shall be an example for any detector-stable slepton[8] that have been predicted.

With exclusion limits between 289 GeV and 537 GeV, depending on the parameters of the considered model [24], a detector-stable slepton is heavy compared to detector-stable SM particles. Therefore it has muon-like tracks and can cause out-of-time E_T^{miss}, which does not contribute to the overall E_T^{miss} in case of back-to-back pair production. If the slepton is the

[7] It would therefore only be long-lived and not detector-stable.

[8] or any heavy, detector-stable, charged, colour neutral, scalar particle predicted by any model for that matter

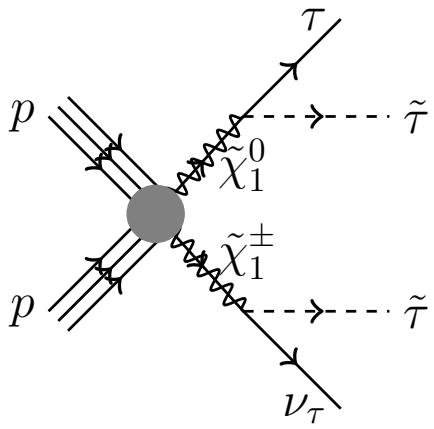

Figure 3.11: Electroweak pair production of staus as examples for long-lived sleptons.

NLSP and the LSP is invisible to the ATLAS detector the slepton can decay into invisible particles as well, if it is long-lived but not detector-stable.

The only differences between stable charginos and stable, charged sleptons are the spin and the production mechanisms. However, without precision measurements of spin correlations, the experiment is not sensitive to the difference between spin $1/2$ charginos and scalar sleptons. The production mechanisms depend on the model in question. Comparing the production mechanisms of stable charginos in figure 3.10 and stable staus in figure 3.11 the stable staus would be accompanied by a lepton signature and E_T^{miss}. In the model independent search [24] this signature difference is irrelevant.

3.3.4 Specific ionisation energy loss and velocity measurement

A charged particle traversing matter loses energy, because it ionises the material. For the specific energy loss ($\mathrm{d}E/\mathrm{d}x$) deposited in the pixel detector the Most Probable Value ($\mathcal{MPV}_{\frac{\mathrm{d}E}{\mathrm{d}x}}$) can be expressed by the parametric function

$$\mathcal{MPV}_{\frac{\mathrm{d}E}{\mathrm{d}x}}(\beta\gamma) = \frac{p_1}{\beta^{p_3}}\ln(1+(p_2\beta\gamma)^{p_5}) - p_4, \tag{3.4a}$$

$$\beta(\beta\gamma) = \sqrt{\frac{(\beta\gamma)^2}{1+(\beta\gamma)^2}}, \tag{3.4b}$$

where $p_1, p_2, ..., p_5$ are parameters, which depend on the properties of the pixel detector, like density and atomic numbers of the elements of the detector or the properties of the particle under study like its charge. These parameters were determined in Ref.[49] using fits to specific energy loss distributions of SM particles. For SMPs the specific energy loss is expected to be larger than for SM particles resulting in the possibility of a precise measurement of the velocity of the particle expressed via $\beta\gamma$. Using the momentum measurement, which is mostly independent of the $\mathrm{d}E/\mathrm{d}x$ in the pixel detector, and the relation $m_{\beta\gamma} = p/\beta\gamma$[9] the mass of the particle can be determined.

Furthermore, the velocity of the particles can be measured through a time-of-flight measurements in the calorimeters [50], MDTs and RPCs. After calibration using $Z \to \mu\mu$ events this information can also be used to determine the masses of the new particles.

[9] See equation 2.9.

3.4 Changes during the long shutdown

During the long shutdown between 13 February 2013 and 5 April 2015 both the LHC and the ATLAS detector experienced a number of changes and upgrades to search for New Physics even more efficiently. Since this work discusses both data and MC simulations from before and after this long shutdown, the most fundamental changes will be discussed below.

Most importantly the centre-of-mass energy was increased from 8 TeV to 13 TeV. At higher centre-of-mass energies the production efficiencies for several New Physics processes increase significantly [20]. Additionally, plans for the future run of the LHC include proton-proton collisions at an even faster rate increasing the luminosity from $L = 8 \times 10^{33}\text{cm}^{-2}\text{s}^{-1}$ peak luminosity in 2012 [41] to $L = 10^{34}\text{cm}^{-2}s^{-1}$ design luminosity and thus increasing the average number of interactions per bunch crossing. The bunch crossing rate increased during data taking after the long shutdown from 20 MHz to 40 MHz in August 2015.

Higher collision rates necessarily lead to changes in the trigger menu to still meet the event selection rate requirements. Furthermore, since many of the trigger thresholds depend on energies directly or indirectly, a higher centre-of-mass energy typically leads to larger event selection rates as well. For example an E_T^{miss}-trigger with a threshold at 80 GeV will have a higher efficiency at $\sqrt{s} = 13$ TeV, because there is more energy available in the particle interactions to produce E_T^{miss}. As a result of that, many triggers in the new menu have higher thresholds or have additional requirements to decrease the event selection rate or received a prescale factor.

Another negative aspect of higher collision rates is pile-up, the occurrence of multiple collision events at the same time. With increasing pile-up it becomes ever harder to reconstruct the primary vertices of secondary particles correctly. This also leads to larger errors in the calculation of E_T^{miss}. To compensate for these pile-up effects a number of new trigger algorithms were developed during the long shutdown. At the time of this writing it is under investigation, which of these trigger algorithms removes pile-up effects most successfully. Therefore analysis teams have to be flexible in their choice of E_T^{miss}-triggers. In figure 3.12[10] the mean number of interactions per bunch crossing at 8 TeV and at 13 TeV is depicted. Both at the beginning of 2012 and 2015 there were a few days of data taking at a low interaction rate for calibration purposes. Since the integrated luminosity at 13 TeV is still smaller by a factor of roughly 200 the influence of this is more prominent in the 13 TeV interactions-per-bunch-crossing distribution in figure 3.12. Other than that the interaction rates are very similar. The interaction rate will however increase, when the LHC reaches its design luminosity.

[10] See section 4 for a description of the used datasets.

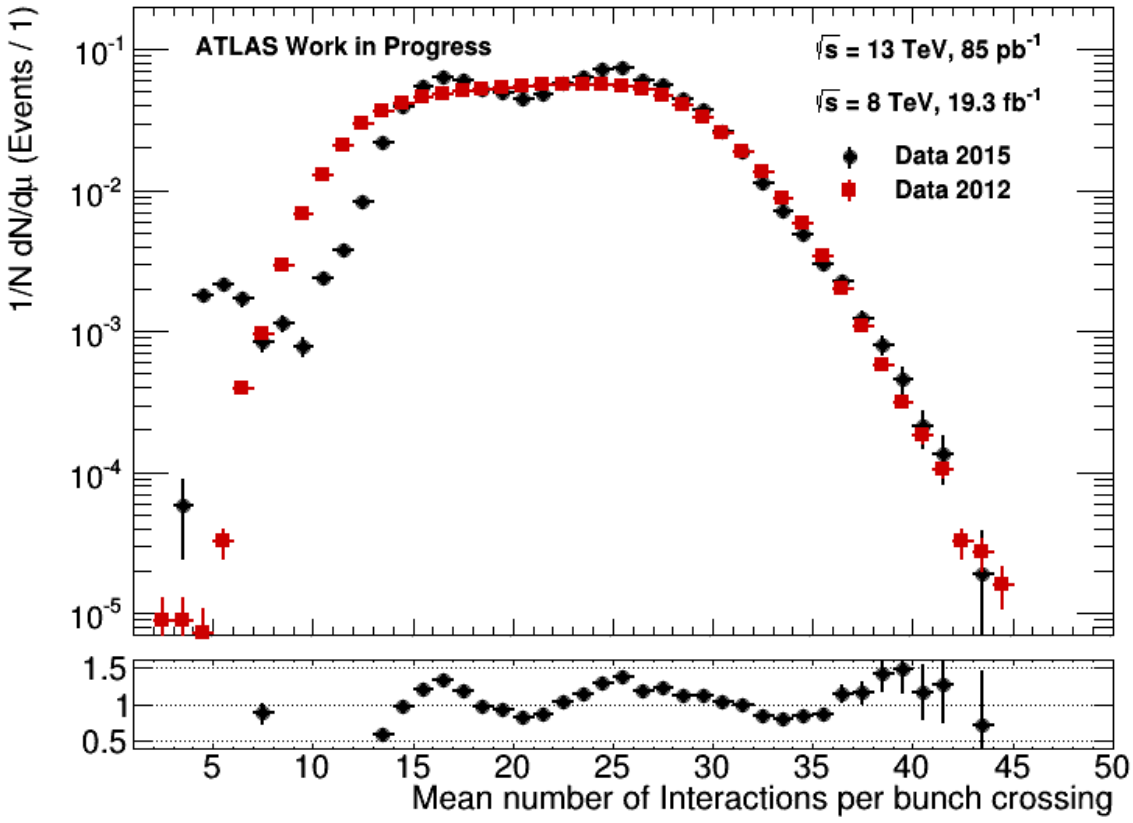

Figure 3.12: Mean number of interactions per bunch crossing for data collected in 2012 at 8 TeV (red squares) and for data taken at 13 TeV in 2015 (black dots). The number of events of each dataset is normalised to one.

Chapter 4

Methods to estimate trigger efficiencies

The core of this work is the estimation of trigger efficiencies described below. Aside from the calculation of trigger efficiencies for data taken with the ATLAS detector at $\sqrt{s} = 13$ TeV the goal is the development and testing of new methods to do so.

4.1 Event samples and trigger items under study

This work uses both proton–proton collision data taken at $\sqrt{s} = 8$ TeV in 2012 and at $\sqrt{s} = 13$ TeV in 2015 as well as signal MC samples and $Z \to \mu\mu$ MC samples simulated at both centre-of-mass energies.

4.1.1 Data and simulated samples

A subset of the 2012 data, which is required to pass a muon trigger and other selection criteria, is used. This dataset is stored in the so called Zmumu-stream and amounts to 19.3 fb^{-1} of integrated luminosity. Additionally, events are required to pass $Z \to \mu\mu$ selection criteria. Thus two muons, which can be reconstructed as products of a Z decay, have to be found. The muon candidates are required to have an invariant mass within 10 GeV distance from the Z boson mass $m_Z = 91.2$ GeV. The selection criteria for the muon candidates are: match to a track reconstructed with $p_T \geq 5$ GeV, a vertex within $|z| < 10$ mm and $r < 2$ mm from the primary vertex, two or more hits in the pixel detectors or passed dead sensors, more than five SCT hits or passed dead sensors, two or less pixel or SCT holes, transverse momentum larger than 20 GeV, isolation from jets with at least 40 GeV transverse momentum more than $\Delta R = 0.30$ and isolation from other tracks with at least 10 GeV transverse momentum more than $\Delta R = 0.25$.

The corresponding $Z \to \mu\mu$ MC sample is simulated using `PYTHIA8` and `POWHEG-BOX` [51][1]. Among the roughly one million simulated events, $Z \to \mu\mu$ events with the same selection criteria as in data are selected. The 8 TeV signal MC samples are simulations of gluino R-hadron pair production with gluino masses between 100 GeV and 1700 GeV in steps of 100 GeV. They are simulated using `PYTHIA6` [52] v. 6.4.27 with specialised hadronisation routines [53, 54].

For data taken at $\sqrt{s} = 13$ TeV with a bunch spacing of 50 ns, the event information of the $Z \to \mu\mu$ data and MC samples is stored in derived datasets keeping only event information relevant for the search for SMPs. Again the events are required to pass the $Z \to \mu\mu$ event selection criteria described above. The candidate selection criteria require the muon candidate to have: at least two pixel hits or passed pixel dead sensors, more than five hits or passed

[1] The simulation tags of all MC samples used in this work can be found in appendix A.

Table 4.1: Trigger items, which are studied in this work, for data taken in 2012.

HLT	L1 trigger
EF_xe80_tclcw_loose	L1_XE40
EF_xe80	L1_XE50
EF_xe100_tclcw_loose	L1_XE50
EF_xe100	L1_XE60
EF_xe110	L1_XE60

dead sensors in the SCT, less than three pixel or SCT holes and a transverse momentum larger than 20 GeV. Additionally, the muon is required to have medium quality, which means that it passed selection criteria similar to the criteria for the 2012 data.

The $Z \rightarrow \mu\mu$ MC sample at $\sqrt{s} = 13$ TeV is simulated again using `POWHEG-BOX` and `PYTHIA8`. Selection criteria equal to the data selection criteria are applied. The gluino R-hadron samples are produced with the same version of `PYTHIA6` , as described above, simulating gluino masses between 800 GeV and 1800 GeV in steps of 200 GeV.

4.1.2 Trigger items under study

The names of ATLAS E_T^{miss}-trigger items contain three parts. The first part is the designation of the trigger level, where L1 denotes level 1 and the full trigger is denoted by EF before and by HLT after the long shutdown. The second part describes the trigger threshold X in the form xe$X$, where xe indicates that the trigger item is an E_T^{miss}-trigger item. In the last part additional requirements for events to be selected by the trigger are denoted. For trigger items used after the long shutdown the L1 trigger threshold Y is indicated at the end of the trigger name in the form L1XEY in some cases.

A number of different E_T^{miss}-trigger items are studied in this work to gain insight into multiple interesting features of the event selection with the ATLAS detector. During data taking with the ATLAS detector there always is a so-called lowest unprescaled E_T^{miss}-trigger, which is the trigger with the highest event selection rate and thus probably also the highest efficiency among the E_T^{miss}-trigger items, which are not prescaled. Obviously this trigger is the most interesting for the analysis teams. During most of data taking in 2012 this was the trigger EF_xe80_tclcw_loose. Therefore the minimum unprescaled E_T^{miss}-trigger threshold for data taken before the long shutdown is 80 GeV. Thus the trigger EF_xe80 is studied as well.

To make comparisons with the trigger items used during data taking with high luminosities after the long shutdown, three trigger items with higher thresholds used in 2012 are studied. The trigger items are chosen such that the difference between the L1 and HLT trigger thresholds has a wide range of values. The trigger items studied in this work for data collected in 2012 are listed in table 4.1 together with their L1 trigger items.

Since the luminosity increases during 2015, the lowest unprescaled trigger changes as well. Early during 2015 the HLT_xe70 was the lowest unprescaled trigger. This then changed to 80 GeV E_T^{miss}-trigger items, which will be followed by 100 GeV E_T^{miss}-trigger items for high luminosity data taking [55]. Again a wide range of differences between HLT and L1 trigger thresholds are chosen. Therefore trigger items, which only differ by their L1 trigger threshold (HLT_xe80_L1XE50, HLT_xe80 and HLT_xe80_L1XE70), are studied. Furthermore, the effects of the new trigger algorithms designed to remove pile-up effects are studied. For data taken in 2015 the trigger items under study are presented in table 4.2.

Table 4.2: Trigger items, which are studied in this work, for data taken in 2015.

HLT	L1 trigger
HLT_xe70	L1_XE50
HLT_xe80_tc_lcw_L1XE50	L1_XE50
HLT_xe80_L1XE50	L1_XE50
HLT_xe80	L1_XE60
HLT_xe80_L1XE70	L1_XE70
HLT_xe100	L1_XE70
HLT_xe100_mht	L1_XE70
HLT_xe100_pueta	L1_XE70
HLT_xe100_pufit	L1_XE70
HLT_xe100_tc_em	L1_XE70
HLT_xe100_tc_lcw	L1_XE70

4.2 Parametrisation of the event selection

The use of E_T^{miss}-trigger items is essential to the search for SMPs, as they show the largest expected efficiencies in signal MCs for large SMP masses. To accurately calculate exclusion limits or the significance of an excess signal, it is important to have a good estimation of the efficiencies of trigger items used in the analysis as well as the systematic uncertainties of those values.

Naturally there are measurement errors involved in the decision of the trigger system, whether a certain event passes a required E_T^{miss}-threshold [22]. For sufficient sample sizes the measurement error is gaussian. The higher the true E_T^{miss} of a given event, the larger the probability for the event to pass the trigger. For sufficiently large E_T^{miss} the probability becomes unity.

A turn-on curve as it is typical for an ATLAS E_T^{miss}-trigger is shown in figure 4.1. As such it depicts the probability for an event with a given offline calorimeter E_T^{miss} to pass the E_T^{miss}-trigger. The offline calorimeter E_T^{miss} is the reconstructed E_T^{miss}, where the transverse momentum contributions from the track reconstruction in the muon spectrometer are ignored. The online E_T^{miss} as it is measured at trigger level ignores the muon contributions as well due to the constraints on the event selection speed. The turn-on curve is calculated by calling the function `TGraphAsymmErrors`(h_p, h_a) of Root [56], where h_a is the histogram corresponding to the offline calorimeter E_T^{miss} spectrum and h_p is the histogram of the same spectrum only with events that passed the E_T^{miss}-trigger. The points $y(E_T^{miss})$ and asymmetric errors $\Delta y_{high,low}(E_T^{miss})$ are calculated via

$$y(E_T^{miss}) = \frac{h_p(E_T^{miss})}{h_a(E_T^{miss})}, \tag{4.1a}$$

$$\Delta y_{low}(E_T^{miss}) = y(E_T^{miss}) - \epsilon_{low}, \tag{4.1b}$$

$$\Delta y_{high}(E_T^{miss}) = \epsilon_{high} - y(E_T^{miss}), \tag{4.1c}$$

$$I_{\epsilon_{low}}(h_p(E_T^{miss}), h_a(E_T^{miss}) - h_p(E_T^{miss}) + 1) = \frac{1-l}{2}, \tag{4.1d}$$

$$I_{\epsilon_{high}}(h_p(E_T^{miss}) + 1, h_a(E_T^{miss}) - h_p(E_T^{miss})) = \frac{1+l}{2}, \tag{4.1e}$$

where $h_p(E_T^{miss})$ and $h_a(E_T^{miss})$ are the number of events passing the trigger and the number

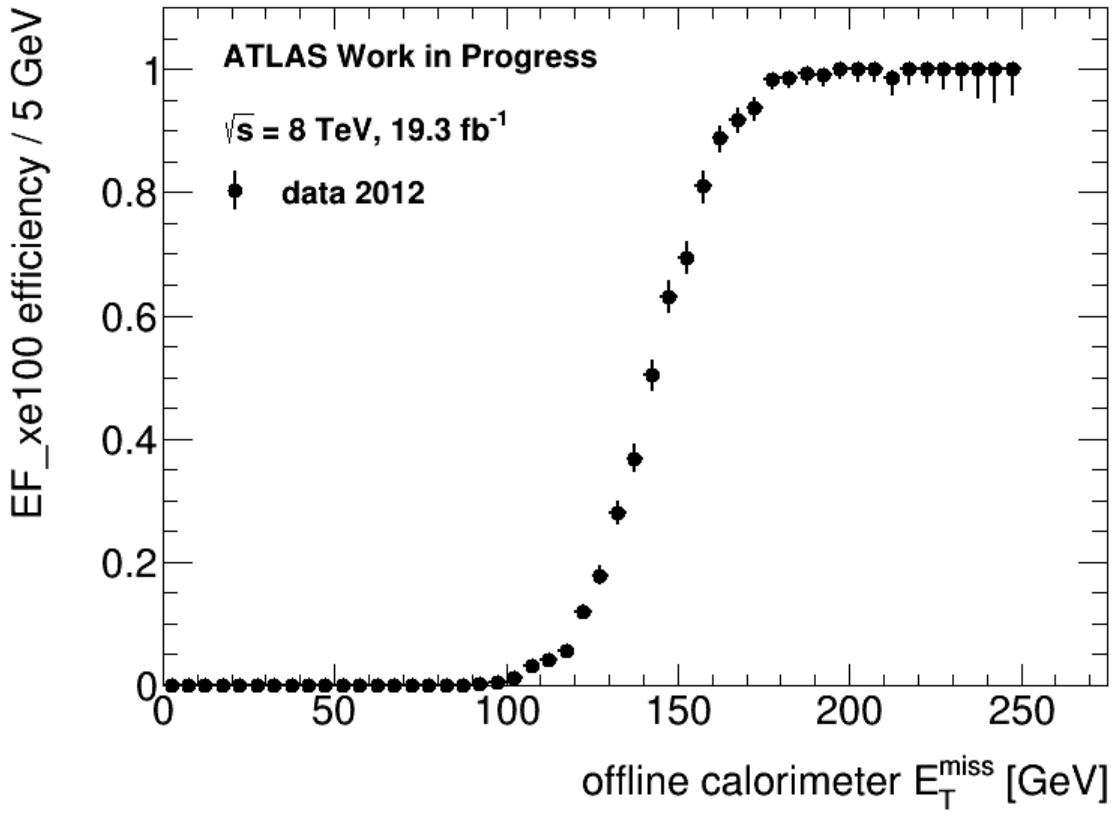

Figure 4.1: Turn-on curve of the trigger EF_xe100 for $Z \to \mu\mu$ selected events in data taken in 2012 at $\sqrt{s} = 8$ TeV. The data-points were calculated by calling the function `TGraphAsymmErrors` of Root [56].

of all events at a given value of E_T^{miss}, respectively. $I_\epsilon(\alpha, \beta)$ is the probability for $\leq \alpha$ events to occur within $\beta + \alpha - 1$ experiments, if the probability for one event to occur in one experiment is ϵ. $l = 0.68269$ is the confidence level of the error [57]. ΔE_T^{miss} is symmetrical and equal to half the bin size of the histograms.

Assuming a normal distribution of the errors, the turn-on curve can be modeled by an integral over a Gaussian for large sample sizes:

$$\Phi(E_T^{miss}) = \frac{A}{2}\left[1 + \mathbf{erf}\left(\frac{E_T^{miss} - B}{\sqrt{2}C}\right)\right], \tag{4.2a}$$

$$\mathbf{erf}(x) = \frac{2}{\sqrt{\pi}}\int_0^x e^{-t^2}\mathrm{d}t, \tag{4.2b}$$

where $\Phi(E_T^{miss})$ is the probability for an event with a given value of E_T^{miss} to pass the trigger, A is the height of the plateau and equals $\Phi(E_T^{miss} \to \infty)$, B is the effective threshold with $\Phi(B) = 0.5 \cdot A$ and C is the standard deviation of the Gaussian. $\mathrm{erf}(x)$ is the error function and $\Phi(x)$ is a shifted error function (just error function from now on), which also is the cumulative distribution function of the Gaussian [58]. For a trigger that becomes fully efficient, $A = 1$.

Since the search for SMPs is a search for new particles, there is no data of SMP events. Because the simulation of detector noise and particle-detector interactions is not exact for E_T^{miss}-trigger items a fully MC-driven calculation of trigger efficiencies, would not lead to a

trustworthy result. Thus a measure of the difference between MC and data event selection is needed.

To gain a deeper understanding of the selection of events, in which SMPs are produced $Z \to \mu\mu$ MC samples and data are considered. Because the calculation of E_T^{miss} on trigger level only uses calorimeter energy deposits and no data from the muon spectrometer, muons appear as E_T^{miss} on trigger level. Considering R-parity conserving supersymmetric models, SMPs are always produced in pairs just like muons in $Z \to \mu\mu$ events. Additionally, the SMPs are, like the products of $Z \to \mu\mu$ decays, dominantly produced with exactly opposite transverse momenta. In those cases there is no overall E_T^{miss} resulting from the production process. There is however the possibility of the emission of ISR (see also section 2.1.1) before or final state radiation (FSR) after the hard production process.

ISR is the most common reason for E_T^{miss}. Because of their similarity to SMP production processes and because they are comparatively easily identifiable in data, $Z \to \mu\mu$ events are used to study the event selection of SMP events.

A good understanding of the signal trigger efficiencies is especially important for the search for SMPs. The reason for that are the efficiencies, which typically range between 0.2 and 0.3, and are therefore small compared to, for example, the efficiencies of muon trigger items in $Z \to \mu\mu$ events, which can be close to 1.0. Despite the muon-like signatures of charged SMPs (see section 3.3) the most efficient muon trigger items are less efficient than the most efficient E_T^{miss}-trigger items for large SMP masses[2]. This is due to the fact that late arriving particles cannot trigger muon trigger items efficiently and the probability that a particle is too slow for the muon trigger rises with its mass. For a sufficiently late arrival the muon-like particle is out-of-time and is therefore not associated with the collision event, in which it is produced.

4.2.1 Minimisation problems

To increase the insight into physical processes or to estimate the "true" behaviour of a physical quantity from statistically distributed data points, functions are determined through minimisation problems. The quantity, which is minimised in the problems considered in this work, is χ^2:

$$\chi^2 = \sum_{i=1}^{N} \frac{(y(E_T^{miss,i}) - \Phi(E_T^{miss,i}))^2}{(\Delta y_*(E_T^{miss,i}))^2 + (\Delta E_T^{miss}(E_T^{miss,i}) \cdot \Phi'(E_T^{miss,i}))^2}, \tag{4.3a}$$

$$\Delta y_*(E_T^{miss,i}) = \Delta y_{low}(E_T^{miss,i}), \quad y(E_T^{miss,i}) - \Phi(E_T^{miss,i}) \leq 0, \tag{4.3b}$$

$$\Delta y_*(E_T^{miss,i}) = \Delta y_{high}(E_T^{miss,i}), \quad y(E_T^{miss,i}) - \Phi(E_T^{miss,i}) < 0, \tag{4.3c}$$

where $y(E_T^{miss,i})$ is a set of N data points with asymmetric errors. $\Phi(E_T^{miss})$ is the value of the fit function at E_T^{miss} and $\Phi'(E_T^{miss})$ the value of its derivative. $\Delta y_{low,high}(E_T^{miss})$ are lower and upper asymmetric errors of the data points. $\Delta E_T^{miss}(E_T^{miss})$ is the uncertainty of the data points in E_T^{miss}-direction. For the data points considered in this work this uncertainty is constant and symmetrical. Thus χ^2 is the error weighted distance between the fit function and the data points. The function with the lowest χ^2 has the highest likelihood i.e. judging from the data points the highest probability to be the function, which describes the process in question. However, the formulation of a minimisation problem is more than a number of data points and a function with yet undetermined fit parameters. Additionally, initial values and limits of the fit parameters are important properties of the minimisation problem. The χ^2 minimum is determined via an iterative process using `TMinuit` [59]. Possible problems with the determination of the χ^2 minimum include the minimisation at a local minimum instead of

[2] In the case of stable gluinos the E_T^{miss}-trigger items become more efficient than muon-trigger items around $m_{\tilde{g}} = 300$ GeV.

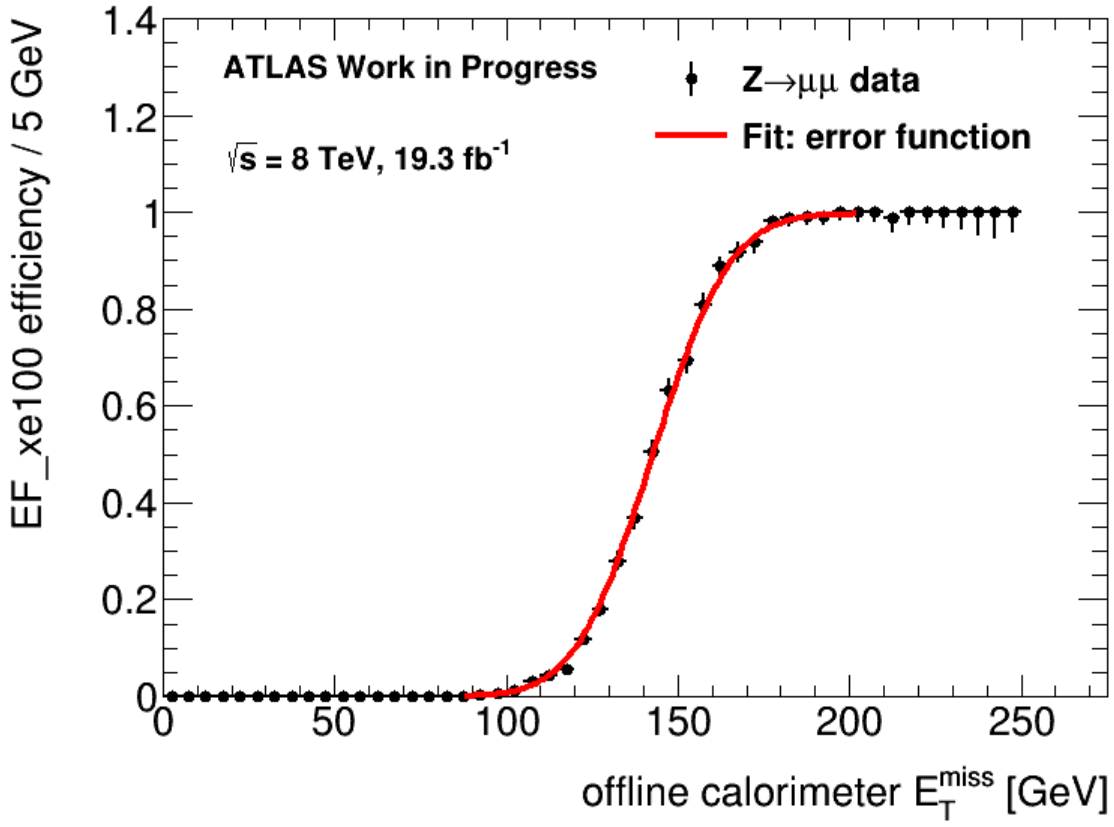

Figure 4.2: Turn-on curve of the trigger EF_xe100 for $Z \to \mu\mu$ selected events in data taken in 2012 at $\sqrt{s} = 8$ TeV (black dots). Error function fit (red solid line) to the data points.

the global minimum. Furthermore, there can be problems near the limits of the parameters or at divergencies of the function in question.

An important byproduct of the determination of the function with the highest likelihood are the errors of the fit parameters. Because the function with the highest likelihood is uniquely determined by a corresponding combination of fit parameters, these parameter errors are a measure of the uncertainty in determining the function.

4.3 Fit functions

From the fit of an error function, as defined in equation 4.2, to the turn-on curve, the height of the plateau A, the effective threshold B and the measurement error C can be obtained. As an example this is done for the trigger EF_xe100, which was part of the trigger menu before the long shutdown. The corresponding fit function can be seen in figure 4.2.

The height of the plateau $A = 0.996 \pm 0.006$ is consistent with a trigger, that becomes fully efficient for large values of E_T^{miss} and from the behaviour of the turn-on curve it is concluded that the real value of A is exactly equal to 1. The same is true for every trigger considered in this study both for data and MC[3]. The effective threshold $B = 143 \pm 1$ GeV is significantly larger than the trigger threshold of 100 GeV. In fact the trigger threshold lies in the beginning of the turn-on area, which is the region of the turn-on curve between the two plateau regions. The reason for that can only be understood by considering both trigger levels. The resolution

[3]Some examples of this can be found in appendix B.

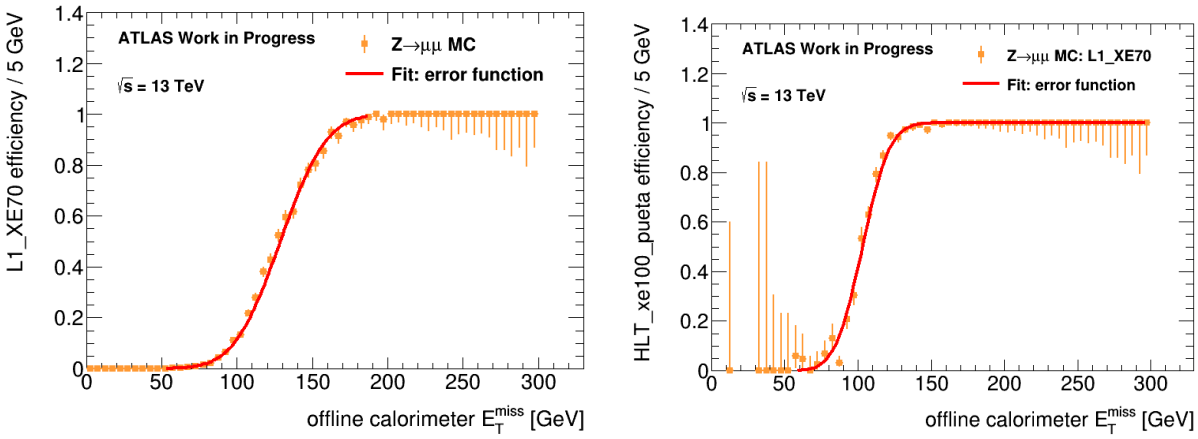

Figure 4.3: Turn-on curve of the trigger L1_XE70 for $Z \to \mu\mu$ selected events in a MC simulated $Z \to \mu\mu$ sample at $\sqrt{s} = 13$ TeV (orange squares). Error function fit (red solid line) to the data points (left). Turn-on curve of the trigger HLT_xe100_pueta for $Z \to \mu\mu$ selected events, preselected with the trigger L1_XE70, in a MC simulated $Z \to \mu\mu$ sample at $\sqrt{s} = 13$ TeV (orange squares). Error function fit (red solid line) to the data points (right).

$C = 17.7 \pm 0.6$ GeV is large compared to trigger items, which do not rely on the measurement of E_T^{miss} like jet or muon trigger items[4].

4.3.1 Multilevel turn-on curve fit functions

As described in section 3.2.4, the event selection with the ATLAS detector happens on multiple trigger levels. Therefore the error function can at most be an approximation of a turn-on curve. To describe the event selection on multiple trigger levels, five alternative fit functions in addition to the error function in equation 4.2 are studied as a part of this thesis.

Multiplied Error Function

The Multiplied Error Function (MEF) is a product of two error functions and is given by

$$\Phi_{MEF}(E_T^{miss}) = \frac{A}{2}\left[1 + \mathbf{erf}\left(\frac{E_T^{miss} - B_1}{\sqrt{2}C_1}\right)\right] \times \frac{1}{2}\left[1 + \mathbf{erf}\left(\frac{E_T^{miss} - B_2}{\sqrt{2}C_2}\right)\right], \tag{4.4}$$

where B_1, C_1, B_2 and C_2 are effective threshold and resolution of HLT and L1 trigger, respectively. The idea here is to model the two trigger decisions independently by describing the HLT as an event selector, which can only select events among a subsample, which is preselected by the L1 trigger. This is already well justified considering how events are selected with the ATLAS detector (see section 3.2.4). To further justify this the event selection on each trigger level is studied independently using simple error functions.

In figure 4.3 the fit of an error function to the turn-on curves of the L1 trigger L1_XE70 (left) and to the turn-on curve of the HLT HLT_xe100_pueta obtained by considering only events, that passed the L1 trigger (right) are depicted. As such the right plot shows the probability for an event with the missing transverse energy E_T^{miss} to pass the HLT on the condition that the event already passed the L1 trigger. From these fits the fit parameters of each trigger level can be obtained and inserting them into the MEF in equation 4.4 yields a parametrisation of the multi-level event selection.

[4]See also appendix B for Jet and muon turn-on curves.

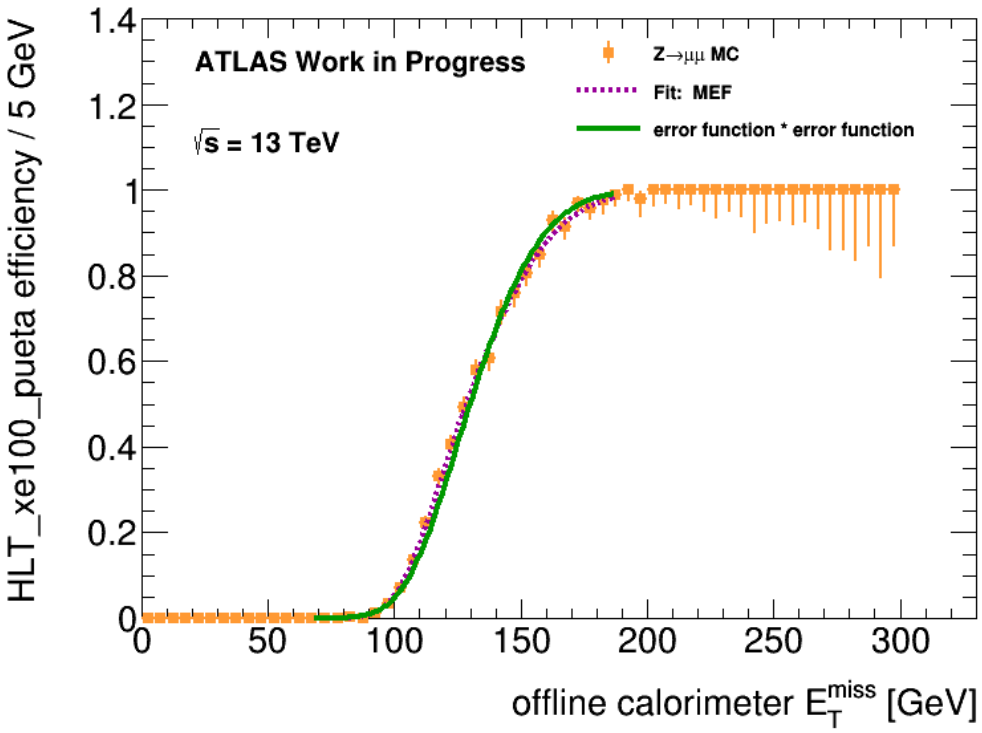

Figure 4.4: Turn-on curve of the trigger HLT_xe100_pueta for $Z \to \mu\mu$ selected events in a MC simulated $Z \to \mu\mu$ sample at $\sqrt{s} = 13$ TeV (orange squares). MEF fit (violet dotted line) to the data points and product of the error function fits in figure 4.4 (green solid line).

In figure 4.4 the turn-on curve of HLT_xe100_pueta together with a MEF with parameters obtained from individual error function fits to each trigger level together with a MEF fit is shown. For the MEF fit to the multi-level turn-on curve the errors increase significantly as can be seen in table 4.3. The reason for that is the correlation between fit parameters, enabling each parameter to reach a greater range of values, because there are more other parameters to compensate for the deviation from the χ^2-minimum of the fit.

Subdivided Error Function

The Subdivided Error Function (SEF) is an alternative to the MEF. It is defined via

Table 4.3: Fit parameters obtained from error function fits to turn-on curves of the individual trigger levels (second and third column). Fit parameters obtained from MEF fit and SEF fit to the full trigger (last two columns).

Fit parameter	L1	HLT	MEF	SEF
B_1 [GeV]		103 ± 1	104 ± 4	123 ± 2
C_1 [GeV]		14.6 ± 0.9	11.6 ± 1.9	14.0 ± 1.2
B_2 [GeV]	128 ± 1		128 ± 2	128 ± 1
C_2 [GeV]	24.1 ± 0.5		27.7 ± 2.3	26.9 ± 1.8

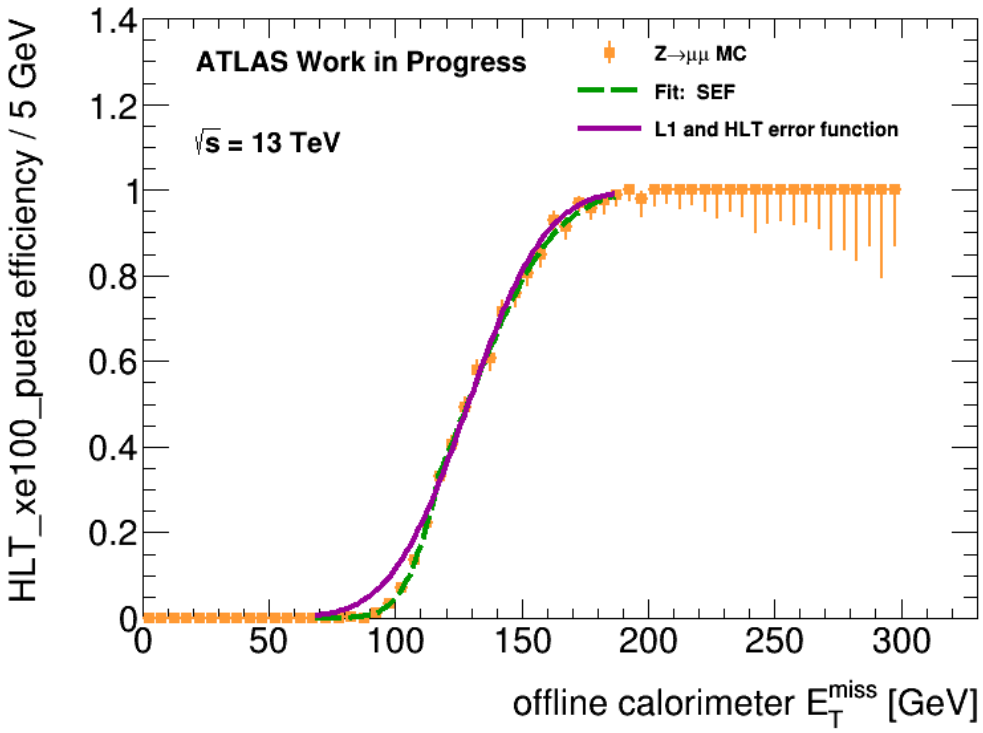

Figure 4.5: Turn-on curve of the trigger HLT_xe100_pueta for $Z \to \mu\mu$ selected events in a MC simulated $Z \to \mu\mu$ sample at $\sqrt{s} = 13$ TeV (orange squares). SEF fit (green dashed line) to the data points and parts of the error function fits in figure 4.3 according to equation 4.5 (violet solid line).

$$\Phi_{SEF}(E_T^{miss}) = \Phi_{HLT}(E_T^{miss}) = \frac{A}{2}\left[1 + \mathbf{erf}\left(\frac{E_T^{miss} - B_1}{\sqrt{2}C_1}\right)\right] \text{ with } E_T^{miss} < E^*, C_1 \neq C_2 \text{ and} \tag{4.5a}$$

$$\Phi_{SEF}(E_T^{miss}) = \Phi_{L1}(E_T^{miss}) = \frac{A}{2}\left[1 + \mathbf{erf}\left(\frac{E_T^{miss} - B_2}{\sqrt{2}C_2}\right)\right] \text{ with } E_T^{miss} \geq E^*, C_1 \neq C_2, \text{where} \tag{4.5b}$$

$$\Phi_{L1}(E^*) = \Phi_{HLT}(E^*) \Rightarrow E^* = \frac{B_2C_1 - B_1C_2}{C_1 - C_2} \text{ and} \tag{4.5c}$$

$$\Phi_{SEF}(E_T^{miss}) = \Phi_{HLT}(E_T^{miss}) \text{ with } C_1 = C_2. \tag{4.5d}$$

The parametrisation with the SEF assumes, that the event selection is dominated by one trigger below E^* and dominated by the other trigger for larger E_T^{miss} values. The advantage over the MEF is the possibility to interpret an additional parameter in E^* and thus gain a deeper understanding of the multi-level event selection with the ATLAS detector. To justify this assumption the same procedure as for the MEF with the parameters obtained earlier is applied to the SEF as is depicted in figure 4.5.

Similar to the MEF fit the parameter errors in the SEF fit increase, as can be seen in table 4.3. Furthermore, the width of the error function describing the upper part of the turn-on curve C_2 is larger than C_1 just like the width of the error function of the L1 trigger is larger than the width of the HLT in figure 4.3. This leads to the conclusion that the event selection is dominated by the L1 trigger for high E_T^{miss} values. This conclusion is supported by

parameter values obtained from fits to MC turn-on curves of the other trigger items considered in this work. Thus another advantage over the MEF becomes apparent, since this distinction between the trigger levels is not possible for a product of error functions.

From the fit parameters acquired through a SEF fit a value for $E^*(B_1, C_1, B_2, C_2)$ can be derived. In the approximation, that the parameters are uncorrelated[5], an uncertainty ΔE^* can be calculated as in

$$\Delta E^* = \sqrt{\Delta B_1^2 \left(\frac{\partial E^*}{\partial B_1}\right)^2 + \Delta C_1^2 \left(\frac{\partial E^*}{\partial C_1}\right)^2 + \dots} \,. \tag{4.6}$$

In the vicinity of $C_1 = C_2$ the SEF becomes unreliable as a fit function, since both E^* and ΔE^* tend towards infinity in that case. Although the resolutions of the trigger levels differ significantly as can be seen from figure 4.3 and table 4.3, there could be problems in the minimisation with the SEF. In that sense it is possible, that the fit algorithm while varying the C_1, C_2 values changes from $C_1 > C_2$ to $C_1 < C_2$, which means that the problematic region is passed in the process. To circumvent this problem two additional fit functions, the Subdivided Error Function with intermediate range (SEFi) and the Subdivided Error Function with bypassed range (SEFb) are defined and tested[6]

$$\Phi_{SEFi}(E_T^{miss}) = \Phi_{SEF}(E_T^{miss}) \text{ with } |C_1 - C_2| \geq \epsilon \text{ and} \tag{4.7a}$$

$$\Phi_{SEFi}(E_T^{miss}) = \Phi_{HLT}(E_T^{miss}) \text{ with } |C_1 - C_2| < \epsilon \text{ and} \tag{4.7b}$$

$$\Phi_{SEFb}(E_T^{miss}) = \Phi_{SEF}(E_T^{miss}) \text{ with } |C_1 - C_2| \geq \epsilon \text{ and} \tag{4.7c}$$

$$\Phi_{SEFb}(E_T^{miss}) = \frac{A}{2}\left[1 + \mathbf{erf}\left(\frac{E_T^{miss} - B^*}{\sqrt{2}C_1}\right)\right] \text{ with } |C_1 - C_2| < \epsilon, \text{where} \tag{4.7d}$$

$$B^* = B_1(\frac{1}{2} + \frac{C_1 - C_2}{2\epsilon}) + B_2(\frac{1}{2} - \frac{C_1 - C_2}{2\epsilon}) \text{ and} \tag{4.7e}$$

$$\epsilon = 100 \text{ MeV}. \tag{4.7f}$$

Gompertz Function

The turn-on curve of an ATLAS E_T^{miss}-trigger has a plateau for small values of E_T^{miss} then reaches a region of small efficiency growth followed by a region of large growth. Before the plateau of maximum efficiency there is another region of small efficiency growth. Therefore the turn-on curve has the shape of a sigmoid function [60]. The error function is an example of a sigmoid function, which is symmetrical with respect to its point of steepest descent. Such a symmetry is only expected for the event selection on a single trigger level but not for multi-level event selection, which introduces asymmetries. Additionally, the requirement to pass an E_T^{miss}-trigger is not always simply to surpass certain E_T^{miss} thresholds, but can be more complicated. For a number of E_T^{miss}-trigger items used after the long shutdown new trigger algorithms were introduced to remove pile-up effects already on trigger level [61]. These algorithms add additional asymmetries.

In figure 4.6 the turn-on curves of HLT_xe100 and HLT_xe100_pueta are depicted, the latter of which uses a new trigger algorithm for the event selection. At the beginning of the turn-on area a deviation from the turn-on curve without a new trigger algorithm can be seen. The overall effect is small. However, the parametrisation of the turn-on curve with a MEF or a SEF, which does not take additional trigger algorithms into account, still is a simplifications

[5] They are clearly not uncorrelated. The approximation is only applied to get a first idea of the meaning of E^*.

[6] The width of the intermediate/bypassed range was chosen to be small compared to the bin-width.

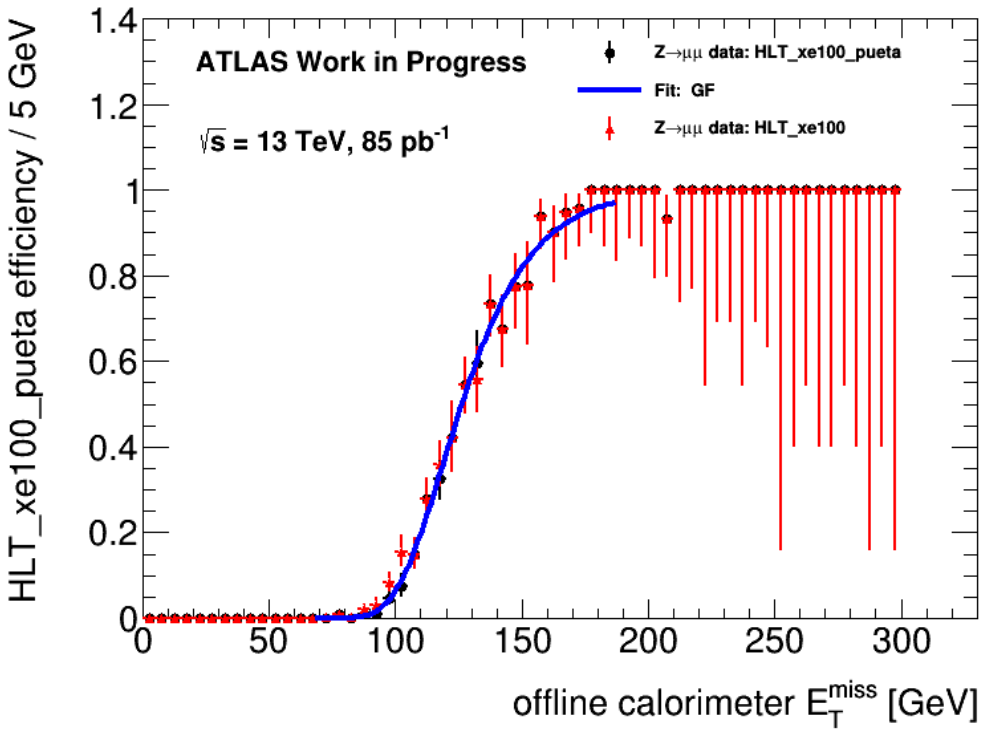

Figure 4.6: Turn-on curves of the trigger items HLT_xe100 (red triangles) and HLT_xe100_pueta (black dots) for $Z \rightarrow \mu\mu$ selected events in data taken in 2015 at $\sqrt{s} = 13$ TeV. GF fit to the HLT_xe100_pueta turn-on curve (blue solid line).

of the event selection. To parametrise the turn-on curves successfully it is important to find a fit function with the highest simplicity i.e. with the lowest number of fit parameters, which enables robust and reliable minimisation. Within the constraints of that requirement the goal is to explain as many features of the event selection as possible like, for example, the asymmetries of the turn-on curve.

The Gompertz Function (GF), defined as

$$\Phi_{GF}(E_T^{miss}) = Ae^{-be^{-E_T^{miss}/c}} \text{ with } b, c > 0, \tag{4.8}$$

is a sigmoid function with no symmetry with respect to the point of steepest decent. Here $A = \Phi_{GF}(E_T^{miss} \rightarrow \infty)$ is the height of the high E_T^{miss} plateau region of the turn on curve, b is a measure of how far the graph stretches to high E_T^{miss} values and c is the inverse growth rate. Since the GF is introduced as a parametrisation with no further justification rather than as a physically motivated model, the results from the GF fits are harder to interpret. Its advantage over the above defined fit functions is the possibility to describe asymmetric turn-on curves with only three fit parameters.

In figure 4.6 a GF fit to the turn-on curve of HLT_xe100_pueta is shown. It is important to note that $\Phi_{GF}(E_T^{miss} = 0) \ll 1$ only if $e^b \gg A$, which is a loose requirement considering the properties of the exponential function.

4.3.2 Methods to Formulate Minimisation Problems

To parametrise the turn-on curves in a robust and reliable way it is important to formulate the minimisation problem optimally. Aside from the choice of a good fit function, three more aspects are discussed below. The correct choice of a subset of data points to fit to, initial parameter values and limits on the fit parameters.

Choice of a turn-on area

The parametrisation is supposed to describe the turn-on area with great accuracy, but it is not necessary to optimise the minimisation for the plateau regions. In the higher plateau region the turn-on curve is dominated by information from the tail of the E_T^{miss} distributions leading to ever increasing errors for large E_T^{miss}. In the lower plateau region, where the efficiency equals zero the errors are very small, which increases their influence on the fit results.

The algorithm to choose the points of the turn-on curve most important for the parametrisation identifies both the end of the lower plateau region and the beginning of the higher plateau region in E_T^{miss} direction to chose all points of the turn-on curve in between as the data points for the minimisation problem. To do this the maximum efficiency value of the turn-on curve is identified and the point with the minimum distance to half of the maximum efficiency is determined as the central point $E_{central}$ by iteration. Then in another iteration over the points in E_T^{miss} direction the difference in efficiencies between the ith and the $(i-1)$th point is calculated. For the points with E_T^{miss} larger than the central point, if the efficiency difference between the ith and the $(i-1)$th point is smaller than 0.002 and if then in another step the difference between the jth and the $(j-1)$th point[7] is also smaller than 0.002[8], the jth point is chosen as the end of the graph with $E_T^{miss} = E_{max}$. The procedure is then repeated in the negative E_T^{miss} direction to find the beginning of the data points E_{min}.

In figure 4.7 the points identified by the above described algorithm for the turn-on curve of HLT_xe100_tc_lcw are shown. It can clearly be seen that the points chosen by the algorithm reach well into the plateau region, which allows the later acquired fitted function to have the desired limit behaviour:

$$\Phi(E_T^{miss} \to \infty) = A, \tag{4.9a}$$

$$\Phi(0) = 0, \tag{4.9b}$$

where A is the efficiency associated with the upper plateau region. For the turn-on curves considered in this work $A = 1$, but one of the advantages of this algorithm is that it can even identify plateau regions, if the trigger in question does not become fully efficient.

Choice of initial values

Another important point for the formulation of a minimisation problem is the optimal choice of initial values. Of course this choice depends on the fit function in use. However, since most of the fit functions (except for the GF) follow the same logic of a turn-on curve describing the integral over the gaussian error of one or two trigger decisions, the determination of the initial values is similar for all the non-GF fit functions. Using the relation $\Phi(B) = 0.5 \cdot A$ the E_T^{miss} value of the central point $E_{central}$ i.e. the point, where the efficiency is closest to $0.5 \cdot A$, is the initial value for the B-like fit parameters (see figure 4.7).

Since C is the standard deviation of the Gaussian and the width of the turn-on area. The initial values for the C-like fit parameters are determined using the relations

[7] This means $j > i$.

[8] The values $0.001, 0.002, 0.003, ..., 0.010$ are tested and at 0.002 the selection of the region, which is important for the parametrisation, shows the best performance.

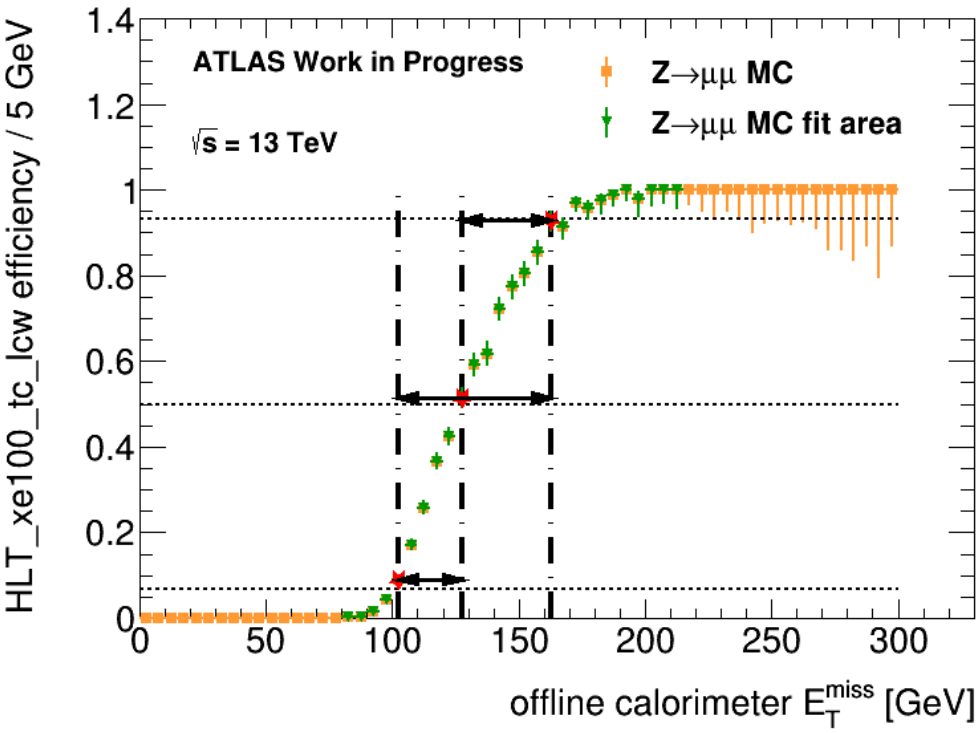

Figure 4.7: Turn-on curve of the trigger HLT_xe100_tc_lcw (orange squares) for $Z \to \mu\mu$ selected events in a MC simulated $Z \to \mu\mu$ sample at $\sqrt{s} = 13$ TeV. Part of the turn-on curve, which is used for the fit (green triangles). Characteristic points of the turn-curve: points closest to half of the maximum efficiency, closest to and larger than $[1-[\Phi(B+x\cdot C)-\Phi(B-x\cdot C)]]/2$ as well as the point closest to and smaller than $1-[1-[\Phi(B+x\cdot C)-\Phi(B-x\cdot C)]]/2$ (red stars) for $x = 1.5$. E_T^{miss} width between these points (black arrows), lines of constant E_T^{miss} of the characteristic points (black dashed dotted lines) and lines of constant efficiency equal to half of the maximum efficiency, $[1-[\Phi(B+x\cdot C)-\Phi(B-x\cdot C)]]/2$ and $1-[1-[\Phi(B+x\cdot C)-\Phi(B-x\cdot C)]]/2$ (black dashed lines).

$$\Phi(B + 1 \cdot C) - \Phi(B - 1 \cdot C) \simeq A \cdot 0.682689, \tag{4.10a}$$
$$\Phi(B + 1.5 \cdot C) - \Phi(B - 1.5 \cdot C) \simeq A \cdot 0.866386, \tag{4.10b}$$
$$\Phi(B + 2 \cdot C) - \Phi(B - 2 \cdot C) \simeq A \cdot 0.954500, \tag{4.10c}$$
$$\Phi(B + 2.5 \cdot C) - \Phi(B - 2.5 \cdot C) \simeq A \cdot 0.987581, \tag{4.10d}$$
$$\Phi(B + 3 \cdot C) - \Phi(B - 3 \cdot C) \simeq A \cdot 0.997300, \tag{4.10e}$$
$$\Phi(B + E) + \Phi(B - E) = A, \tag{4.10f}$$

where E is an arbitrary energy. A part of the turn-on curve between $[1 - [\Phi(B + x \cdot C) - \Phi(B - x \cdot C)]]/2$ and $1 - [1 - [\Phi(B + x \cdot C) - \Phi(B - x \cdot C)]]/2$ is selected and its points of minimum and maximum efficiency $y(E_\alpha)$ and $y(E_\beta)$ are identified (see figure 4.7). The difference between E_α and E_β depends on the confidence factor x.

It is concluded that $E_\beta - E_\alpha \equiv \Delta E_T^{miss}$ roughly equals $2 \cdot x \cdot C$. Thus $\Delta E_T^{miss}/(2x)$ is chosen as the initial value for C. For the SEF-like functions it is not practical to use equal initial values for both C-like fit parameters, because there are potential discontinuities in the $C_1 \simeq C_2$ region of the parameter space. Therefore the distances between the central point and the end points are chosen as $\Delta E_T^{miss,left} \equiv E_{central} - E_\alpha$ and $\Delta E_T^{miss,right} \equiv E_\beta - E_{central}$. The larger distance is chosen as the width of the L1 trigger turn-on curve, because the L1 trigger decision naturally has larger errors, since at this trigger level there is both less time and less information for the trigger decision. If $\Delta E_T^{miss,left} = \Delta E_T^{miss,right}$ a value equal to the bin-width ΔE_{bin} is added to the initial C_2 value.

The method to estimate initial values is illustrated in figure 4.7 and the choices for the initial values are summarized in table 4.4. The initial values for the GF can not be determined as easily from the turn-on curve, because the GF is harder to interpret and the motivation for its use is weaker. After the study of GFs with manually varied parameters the values $b = 400$ and $c = 1/6 \cdot E_{central}$ are found to typically approximate the turn-on curve well.

For the ATLAS E_T^{miss}-trigger items considered in this work the assumption $A = 1$ is viable, which can be seen from the turn-on curves in the figures shown above. Therefore the parameter A is fixed to unity for all minimisation problems.

It is a priori unclear, which value for x yields the optimal fit results. For small values of x the points are selected in a steep area of the turn-on curve, which means that the uncertainty to select points with the correct efficiency value is high. For large values of x the points are selected at the beginning of the plateau region, where the turn-on curve has only a small slope leading to a larger uncertainty of selecting the points with the correct E_T^{miss} value. Five different values for $x = 1.0, 1.5, 2.0, 2.5, 3.0$ are tested. The decisive criterion for the best confidence factor is, for which value of x the minimisation problem converges most reliably.

Choice of parameter limits

Crucial to the formulation of a minimisation problem is the ideal choice of parameter limits. Large parameter limits can hurt the fit performance, because the parameters may vary around local χ^2 minima far from the global χ^2 minimum. In case of too small parameter limits the fit might reach a minimum at the limit of a parameter potentially leading to bad error estimations or the true minimum might even be outside the parameter limit. Three sets of parameter limits are considered to optimise the fit performance for each fit function. The sets of parameter limits are varied independently from the x values, from which the initial values are determined. For each combination of initial values and parameter limits each of the above mentioned fit functions is used for a fit to 10 different turn-on curves and the convergence of the minimisation is checked. One set of parameter limits is to apply no parameter limits at all.

Table 4.4: Summary of the initial values chosen for the minimisation problems with each of the six fit functions. The initial values depend on the parameter x, which is varied from 1 to 3 in steps of 0.5 to optimise the choice of initial values. Aside from x, the initial values depend solely on the data points of the turn-on curve.

error function	A	1.0 fixed
	B	$E_{central}$
	C	$\Delta E_T^{miss}/(2x)$
MEF		
	A	1.0 fixed
	B_1	$E_{central}$
	C_1	$\Delta E_T^{miss}/(2x)$
	B_2	$E_{central}$
	C_2	$\Delta E_T^{miss}/(2x)$
SEF	A	1.0 fixed
	B_1	$E_{central}$
	C_1	$\mathrm{Min}(\Delta E_T^{miss,left}/x, \Delta E_T^{miss,right}/x)$
	B_2	$E_{central}$
	C_2	$\mathrm{Max}(\Delta E_T^{miss,left}/x, \Delta E_T^{miss,right}/x)$
	or	$\Delta E_T^{miss,right}/x + \Delta E_{bin}$ with $\Delta E_T^{miss,left} = \Delta E_T^{miss,right}$
GF	A	1.0 fixed
	b	400
	c	$1/6 \cdot E_{central}$

For the error function the B parameter cannot be smaller than the lower trigger threshold i.e. the L1 trigger threshold E_{L1}. As can be seen from figure 4.1, almost no events are selected below the threshold and therefore the E_T^{miss} value of half efficiency cannot be below that value. Furthermore, the B parameter has to be smaller than the beginning of the upper plateau region E_{max} with the same reasoning. The upper limit for the C parameter is set to the difference between the B parameter limits consistent with the choice of B parameter limits. The lower limit is set to 5 GeV from the knowledge of typical E_T^{miss} turn-on curves. For trigger items with smaller event selection uncertainties this might be an overestimation. For the third and tightest set of parameter limits the knowledge gained from the calculation of initial values is used. The B parameter limits are set to E_{L1} and E_β. The limits of the C parameter are again 5 GeV and the difference between the B parameter limits.

For the MEF the lower loose limit of the B_1 and B_2 parameters are set to the L1 threshold E_{L1} and the upper limit is set to E_{max} equal the B limits of the error function. The tight parameter limits are the L1 threshold and E_β respectively. In each case the C parameter limits are 5 GeV and the difference between the B parameter limits. This choice respects that each factor of the MEF describes a different trigger level. The same parameter limits are used for the SEF-like functions. The knowledge about E_T^{miss}-trigger turn-on curves could not be applied as easily to the GF. Therefore the parameters b and c are only required to be positive. In table 4.5 the sets of parameter limits are summarised.

4.4 Systematic uncertainty estimation methods

Three methods to estimate the systematic uncertainty are presented below. The first method was used before the long shutdown [24]. The other two were developed for this work.

Table 4.5: Summary of two of the sets of parameter limits chosen for the parameter limits with each fit function. SEF represents all SEF-like functions. Prior knowledge of the trigger thresholds is used to determine the parameter limits.

		loose	tight
error function	B	$E_{L1} \leftrightarrow E_{max}$	$E_{L1} \leftrightarrow E_{\beta}$
	C	5 GeV $\leftrightarrow E_{max} - E_{L1}$	5 GeV $\leftrightarrow E_{\beta} - E_{L1}$
MEF, SEF	B_1	$E_{L1} \leftrightarrow E_{max}$	$E_{L1} \leftrightarrow E_{\beta}$
	C_1	5 GeV $\leftrightarrow E_{max} - E_{L1}$	5 GeV $\leftrightarrow E_{\beta} - E_{L1}$
	B_2	$E_{L1} \leftrightarrow E_{max}$	$E_{L1} \leftrightarrow E_{\beta}$
	C_2	5 GeV $\leftrightarrow E_{max} - E_{L1}$	5 GeV $\leftrightarrow E_{\beta} - E_{L1}$
GF	b	> 0	> 0
	c	> 0	> 0

4.4.1 Uncertainty estimation used in 2012

The fitting algorithm not only returns fit parameter values of the fit with the highest likelihood, but also parameter errors. These can be used to estimate the error on the trigger efficiency. One method, which was used in the search for SMPs before the long shutdown [24], treats the errors of the parameters independently disregarding correlation effects, to get an upper limit on the efficiency estimation error. Taking the error function as an example and varying the parameters B and C independently by their 1 σ error leads to a total of nine different error functions with $B = B_{min}, B_{min} - \Delta B, B_{min} + \Delta B$ and $C = C_{min}, C_{min} - \Delta C, C_{min} + \Delta C$ as the parameters. Here B_{min}, C_{min} are the parameters at the χ^2 minimum and $\Delta B, \Delta C$ are the 1 σ errors. Each of these error functions is then multiplied bin-by-bin with the offline calorimeter E_T^{miss} spectrum of the signal MC in questions. Dividing the sum over the so calculated bin contents by the total number of events leads to an estimation of the efficiency $\epsilon^{(B,C)}$ depending on the parameters B and C

$$\epsilon^{(B,C)} = \frac{\sum_i \Phi^{(B,C)}(E_T^{miss,i}) \cdot N_i}{\sum_i N_i}, \tag{4.11}$$

where $\Phi^{(B,C)}$ is the error function with the parameters B and C, N_i is the number of entries in the ith bin of the signal E_T^{miss} spectrum and $E_T^{miss,i}$ is the $E_T^{miss}$of the ith bin. The so calculated efficiencies, with parameters obtained from a fit to a turn-on curve in $Z \to \mu\mu$ events in data taken at $\sqrt{s} = 8$ TeV and an E_T^{miss} spectrum in a gluino R-hadron signal MC sample, are listed in table 4.6.

The systematic uncertainty is then calculated from three contributions. The first contribution to the systematic uncertainty Δ_{data} is the maximum relative difference between the efficiencies in table 4.6 and $\epsilon^{(B_{min},C_{min})}$. The second contribution Δ_{MC} is calculated by repeating the procedure with a fit to a turn-on curve in $Z \to \mu\mu$ MC events. The third and last contribution $\Delta_{rel,dif}$ is defined as the relative difference between the efficiencies $\epsilon^{(B_{min},C_{min})}$ calculated from MC and data respectively. The calculation of the total uncertainty Δ as the quadratic sum of the three contributions is summarised in

Table 4.6: Trigger efficiency obtained by bin-by-bin multiplying an error function turn-on curve fit of the trigger EF_xe100_tclcw_loose in $Z \to \mu\mu$ data taken in 2012 at $\sqrt{s} = 8$ TeV with the E_T^{miss} spectrum of a gluino R-hadron signal sample with $m_{\tilde{g}} = 800$ GeV (second row, second column). The other efficiency values are obtained by varying the parameters B and C independently by their errors. The deviation from the central efficiency value is shown in brackets.

	$B - \Delta B$	B	$B + \Delta B$
$C - \Delta C$	0.214(+0.709%)	0.212(−0.146%)	0.210(−0.990%)
C	0.214(+0.858%)	0.213(±0%)	0.211(−0.847%)
$C + \Delta C$	0.215(+1.02%)	0.213(+0.155%)	0.211(−0.695%)

$$\Delta_{MC} = \mathrm{Max}_{B,C} \left(\frac{|\epsilon_{MC}^{(B_{min},C_{min})} - \epsilon_{MC}^{B,C}|}{\epsilon_{MC}^{(B_{min},C_{min})}} \right), \tag{4.12a}$$

$$\Delta_{data} = \mathrm{Max}_{B,C} \left(\frac{|\epsilon_{data}^{(B_{min},C_{min})} - \epsilon_{data}^{B,C}|}{\epsilon_{data}^{(B_{min},C_{min})}} \right), \tag{4.12b}$$

$$\Delta_{rel,dif} = \frac{|\epsilon_{MC}^{(B_{min},C_{min})} - \epsilon_{data}^{(B_{min},C_{min})}|}{\mathrm{Min}(\epsilon_{MC}^{(B_{min},C_{min})}, \epsilon_{data}^{(B_{min},C_{min})})}, \tag{4.12c}$$

$$\Delta = \sqrt{\Delta_{MC}^2 + \Delta_{data}^2 + \Delta_{rel,dif}^2}. \tag{4.12d}$$

This method can just as easily be applied to the fit functions defined in the previous section. The contributions Δ_{MC} and Δ_{data} are in this case obtained via the maximisation over 3^n efficiencies, where n is the number of fit parameters of the fit function. Due to the correlation between the fit parameters this leads to larger uncertainties, the larger n is.

4.4.2 Interpretation of parameter errors

To improve the precision of the error estimation a deeper insight into the parameter error estimation with the fit algorithm is needed[9]. The parameter errors used in the method described above are calculated from the error matrix, which is obtained by inverting the second derivative matrix of χ^2. The errors of the parameters are the square roots of the diagonal elements of the error matrix and thus they are by definition symmetrical with respect to the χ^2 minimum. An alternative way to estimate the parameter errors is the MINOS algorithm [59].

Here the error is calculated using a contour of constant χ^2 values in parameter space. Taking again the error function as an example, the contour is defined as a set of points (B, C) in parameter space

$$\{(B, C) \mid \chi^2_{B,C} = \chi^2_{min} + \mathbf{up}\}, \tag{4.13}$$

where **up** is constant. For $\mathbf{up} = 0$, the contour is a single dot at the minimum. The $\mathbf{up} = 1$ contour obtained from an error function fit is depicted in figure 4.8. The MINOS error can be calculated by identifying the points on the contour, where the parameters have their extremal values $(B_{low}, B_{high}, C_{low}, C_{high})$. The statement behind the MINOS error is therefore that

[9] More on this topic in Ref.[62]

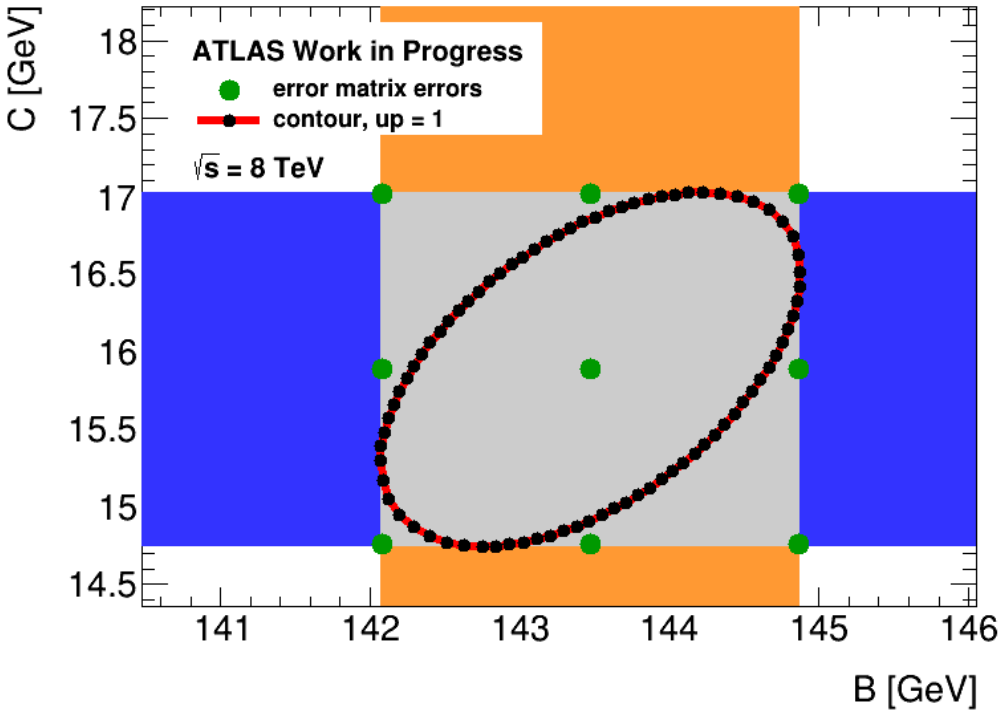

Figure 4.8: Characteristic subspaces of the parameter space of an error function fit. Contour of constant $\chi^2 = \chi^2_{min} + 1$ with 39.3% probability content (black dots, red solid line). Rectangle bounded by the extreme B and C values of the contour (grey area). Rectangle bounded by the extreme B values of the contour and infinite length in the C direction (orange and grey areas). Rectangle bounded by the extreme C values of the contour and infinite length in the B direction (blue and grey areas). Points obtained by varying the two parameters independently by their error matrix errors (green dots). Contour and points were obtained from an error function fit with $x = 1.5$ to the EF_xe100 turn-on curve for $Z \to \mu\mu$ events simulated at $\sqrt{s} = 8$ TeV.

the probability for the true value of B to lie between B_{low} and B_{high} is 68.269%[10]. For the error function fits considered in this work the MINOS errors and the parameter errors obtained from the error matrix are nearly the same. For an example error function fit this can be seen in figure 4.8. In this case the parameter values are $B = 143.470^{+1.404}_{-1.395}$ GeV and $C = 15.8876^{+1.1336}_{-1.1450}$ GeV for the MINOS technique and $B = 143.470 \pm 1.394$ GeV and $C = 15.8876 \pm 1.1304$ GeV calculated via the error matrix.

To estimate the systematic uncertainty of the efficiency it is required to make statements about the probability for the efficiency to be within a certain range of possible values. This is estimated by using the function acquired with the minimisation problem. Thus the statements about the likelihood of efficiency values can be expressed as the likelihood of the fit function. The function is uniquely determined by a combination of all of the parameters. Therefore the uncertainty is a function of the parameter errors, which have to be considered in combination instead of individually. This means the definition of an area in the 2-dimensional parameter space with the required probability content is needed to define a range of possible efficiencies within the required confidence level.

By using the method presented in the previous subsection this area is essentially defined as a rectangle, where $B_{low} < B < B_{high}$ and $C_{low} < C < C_{high}$ with errors obtained from the error matrix. Regardless of whether the MINOS errors or the error matrix errors are used for

[10]The probability is $\Phi(B + C) - \Phi(B - C)$ to be exact.

Table 4.7: Height of the contour of constant χ^2 values above the χ^2 minimum depending on the number of parameters and the desired probability content. Values for **up** calculated from the inverse cumulative distribution function of the χ^2 distribution.

up	x	39.347%	68.269%	95.450%	99.730%
n					
1		0.2653	1.0	4.0	9.0
2		1.0	2.2958	6.1801	11.829
3		1.8388	3.5267	8.0249	14.156
4		2.7154	4.7195	9.7156	16.251
5		3.6119	5.8876	11.314	18.205

the definition of this rectangle, there are two problems with this choice. Firstly the area does not respect the likelihoods for the parameter pairs to be the true parameter values. As such there are regions inside the rectangle with lower likelihood than some regions of the same size just outside the area. The second problem is that it is not trivial to calculate the probability content of such an area and it is therefore in general impossible to interpret the systematic uncertainty calculated with this definition [63].

For the contour it is guaranteed by definition that any point outside the contour has a lower likelihood than a point inside. In case of the contour in figure 4.8 the probability content is 39.3%. The relation between the probability content of a contour x, the number of parameters n and the value of **up** is given by

$$\mathbf{up} = F^{-1}(x; n), \tag{4.14}$$

where $F^{-1}(x; n)$ is the inverse cumulative distribution function of the χ^2 distribution with n degrees of freedom i.e. for an n-parameter problem. A number of values for **up** calculated with equation 4.14 are given in table 4.7[11]. The value $\mathbf{up} = F^{-1}(0.68269; 2) = 2.2958$ is thus used for the contours of two parameter fits and the value $\mathbf{up} = F^{-1}(0.68269; 4) = 4.7195$ for four parameter fit functions.

4.4.3 Uncertainty estimation methods developed for this work

In this work the systematic uncertainty estimation using a parameter subspace with 68.269% probability content is tested. To do this for each fit the contour, where $\chi^2 = \chi^2_{min} + \mathbf{up} = const.$ is determined by calling the function `MnContour` of TMinuit [59] and requiring n_c points on the contour to get a sufficient precision. For each point on the contour the respective fit function is multiplied bin-by-bin with the signal offline calorimeter E_T^{miss} spectrum as in the uncertainty estimation method described above. From $Z \to \mu\mu$ data and MC contributions to the systematic uncertainty together with the unchanged contribution from the relative difference between the MC and data fits with the highest likelihood the systematic uncertainty is again calculated as the quadratic sum over the three contributions.

In figure 4.9 the parameter subspaces, which form the basis of the uncertainty estimation methods, are depicted. The blue rectangle, which is determined from the 1σ parameter errors, is mostly enclosed by the contour, but since only extremal points are considered for the uncertainty estimation, it is at this point unclear, which of the methods yields higher uncertainties. As a counterpart to table 4.6, efficiency values corresponding to the points on the contour method are listed in table 4.8. There, both the largest and the smallest efficiency

[11] One may note the quadratic relation between the value of **up** for $n = 1$ and the confidence level.

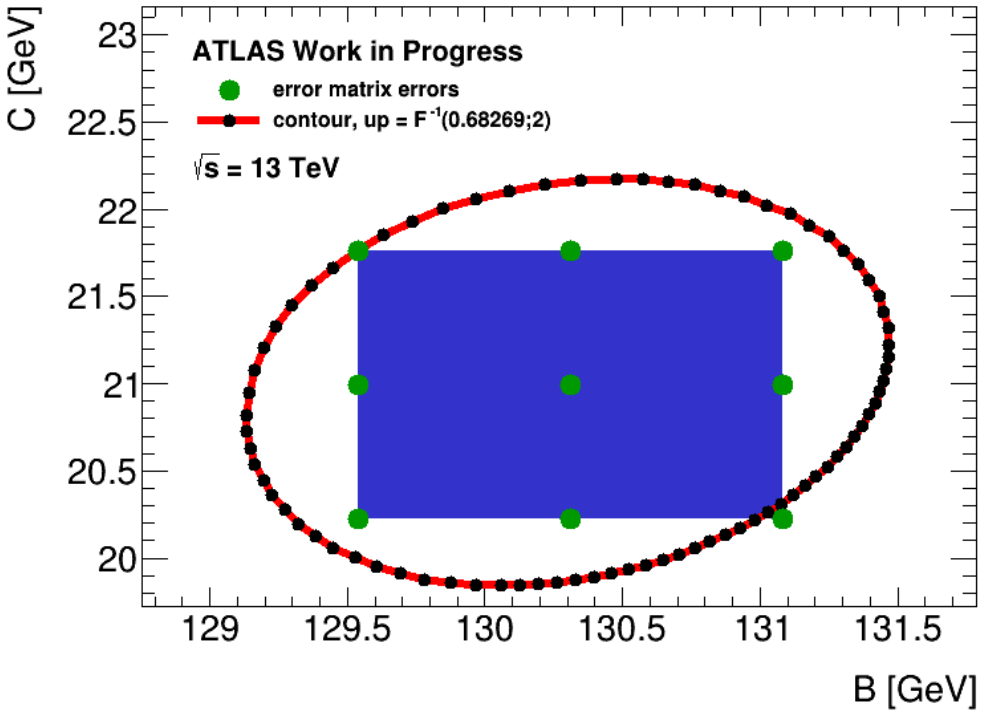

Figure 4.9: Subspaces of the parameter space of an error function fit corresponding to the two error estimation methods. Contour of constant $\chi^2 = \chi^2_{min} + 2.30$ with probability content 68.3% (black dots, red solid line). Points obtained by varying the parameter values independently by their error matrix error (green dots) and the rectangle bounded by these points (blue area). The contour and the points are obtained from an error function fit to the turn-on curve of the trigger HLT_xe100_pufit in $Z \to \mu\mu$ events simulated at $\sqrt{s} = 13$ TeV.

Table 4.8: Trigger efficiencies obtained by multiplying $n_c = 80$ different error functions corresponding to the points on the contour bin-by-bin with the signal E_T^{miss} spectrum of gluino R-hadrons with $m_{\tilde{g}} = 1400$ GeV simulated at $\sqrt{s} = 8$ TeV. The contour and thus the parameter values of the error function were obtained from an error function fit to the turn-on curve of the trigger EF_xe100 in $Z \to \mu\mu$ events for data taken in 2012 at $\sqrt{s} = 8$ TeV. The extreme efficiency values are marked in bold.

i	$\epsilon^{(B,C)}$	i	$\epsilon^{(B,C)}$	i	$\epsilon^{(B,C)}$	i	$\epsilon^{(B,C)}$
1	0.141(0.94)	21	0.139(-0.41)	41	0.138(-0.93)	61	0.140(0.43)
2	0.141(0.91)	22	0.139(-0.46)	42	0.138(-0.90)	62	0.140(0.47)
3	0.141(0.89)	23	0.139(-0.50)	43	0.138(-0.87)	63	0.140(0.52)
4	0.141(0.85)	24	0.139(-0.54)	44	0.138(-0.83)	64	0.140(0.56)
5	0.141(0.81)	25	0.139(-0.59)	45	0.138(-0.79)	65	0.140(0.60)
6	0.140(0.76)	26	0.139(-0.63)	46	0.138(-0.74)	66	0.140(0.64)
7	0.140(0.71)	27	0.138(-0.67)	47	0.138(-0.69)	67	0.140(0.68)
8	0.140(0.66)	28	0.138(-0.71)	48	0.138(-0.64)	68	0.140(0.72)
9	0.140(0.56)	29	0.138(-0.74)	49	0.139(-0.54)	69	0.140(0.76)
10	0.140(0.46)	30	0.138(-0.78)	50	0.139(-0.44)	70	0.140(0.79)
11	0.140(0.36)	31	0.138(-0.81)	51	0.139(-0.34)	71	0.141(0.83)
12	0.140(0.26)	32	0.138(-0.84)	52	0.139(-0.23)	72	0.141(0.85)
13	0.140(0.14)	33	0.138(-0.87)	53	0.139(-0.13)	73	0.141(0.88)
14	0.139(0.04)	34	0.138(-0.89)	54	0.139(-0.02)	74	0.141(0.91)
15	0.139(-0.07)	35	0.138(-0.92)	55	0.140(0.09)	75	0.141(0.93)
16	0.139(-0.17)	36	0.138(-0.93)	56	0.140(0.19)	76	0.141(0.94)
17	0.139(-0.22)	37	0.138(-0.95)	57	0.140(0.24)	77	0.141(0.96)
18	0.139(-0.27)	**38**	**0.138(−0.95)**	58	0.140(0.29)	**78**	**0.141(0.96)**
19	0.139(-0.32)	39	0.138(-0.95)	59	0.140(0.33)	79	0.141(0.96)
20	0.139(-0.37)	40	0.138(-0.94)	60	0.140(0.38)	80	0.141(0.95)

value are marked in bold. The points corresponding to these values are located opposite to each other on the contour and are near the points of the largest and smallest value of B on the contour.

As can be seen from table 4.7 this method can in principle be extended to any required confidence level by changing the value for **up**. To extend this method to fit functions with a higher number of parameters is however not as trivial. For a fit function with n fit parameters there are $n(n-1)/2$ possible contours, one for each pair of parameters. Maximising the efficiency deviation from the fit with the highest likelihood along these contours again leads to an uncertainty estimation equivalent to the two parameter example described above. However, the confidence region (the parameter subspace with a given probability content) is limited by a multidimensional hypersurface instead of a one dimensional contour in the two parameter case. The hypersurface can in principle be interpolated from the contours if the shape of the parameter subspace is not too complex.

The precision can theoretically be increased indefinitely by increasing the number of points on the contour n_c. The so calculated uncertainty should converge for large values of n_c and for n_c larger than a certain value the precision should be dominated by statistical uncertainties. Several values for n_c are tested to find an ideal value N_c, where the uncertainty only changes slightly with increasing n_c and thus $\Delta_{N_c} - \Delta_{N_c-1}$ is sufficiently small.

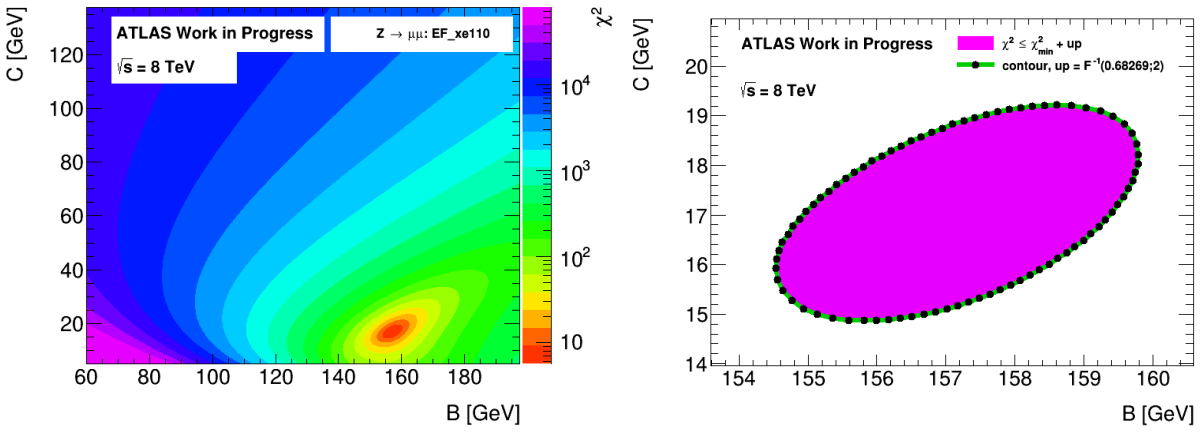

Figure 4.10: Regions of the parameter space of an error function fit to the EF_xe110 turn-on curve in $Z \to \mu\mu$ events simulated at $\sqrt{s} = 8$ TeV: Values of χ^2 in the fit parameter space between the parameter limits on a grid with $n_g^2 = 1000^2$ points (left). Contour of constant χ^2 with 68.3% probability content calculated by calling `MnContour` (black dots, red solid line) and part of the parameter space with $\chi^2 \leq \chi^2_{min} + 2.30$ determined by calculating χ^2 directly on a grid (violet area) (right).

Hypersurface approximation using a fit parameter grid

An alternative way to approximate the hypersurface, which bounds the confidence region uses a grid of parameter values to calculate χ^2 over a wide range of the parameter space. First for each of the d parameters, the range between the parameter limits is divided into n_g steps, resulting in n_g^d grid points in the parameter subspace bounded by the parameter limits. At each point the $\chi^2(\Phi^{(B,C,...)}(E_T^{miss}), y(E_T^{miss}))$ between the fit function $\Phi^{(B,C,...)}(E_T^{miss})$ with these d fit parameters and the turn-on curve $y(E_T^{miss})$ is calculated. The χ^2 in the parameter space of a fit function can be seen in figure 4.10.

Using these χ^2 values a subset of the parameter space is selected according to

$$\{(B, C, ...) \mid \chi^2_{B,C,...} \leq \chi^2_{min} + \mathbf{up}\}, \tag{4.15}$$

where $B, C, ...$ represent any number of parameters in the fit function. For the two dimensional case, the χ^2 values on n_g^2 grid point in this parameter subspace are shown in figure 4.10. Equivalently to the calculations leading to table 4.6 and table 4.8 these points can be used for bin-by-bin multiplications of functions near the χ^2 minimum and the signal E_T^{miss} spectra.

The advantage of this method is the very reliable selection of the relevant parameter subspace without relying on the convergence of minimisation problems, which are used to calculate the contours. In the same sense the calculations in this method are more transparent. The disadvantages of this method are the precision, which can be increased by increasing the resolution of the grid n_g, and the high computation time, which increases proportional to n_g^d.

Similarly to the contour method the uncertainty is expected to converge to the true value of the uncertainty for large n_g. Furthermore, both the contour method and the grid method are expected to lead to the same result.

Chapter 5

Results

The results of the analysis are presented below. They include the performance of the newly developed methods to estimate systematic uncertainties. Additionally, estimates of the efficiencies of the triggers used before and after the long shutdown are presented together with their systematic uncertainties.

5.1 Performance of the minimisation with new fit functions

The most important criterion for the use of one of the new fit functions is, whether the minimisation converges reliably to the global χ^2 minimum. For each fit function this is checked for all different sets of parameter limits and initial values. For each minimisation TMinuit returns one of the statuses CONVERGED, OK, SUCCESSFUL, PROBLEMS, NOT POSDEF, CALL LIMIT or FAILED to summarise the fit result. To simplify the discussion of the fit performance a grade system is introduced. The purpose of this is to have an intuitive way to describe the overall performance, while applying the fit method to multiple turn-on curves. The ten turn-on curves of triggers used before the long shutdown are considered, in order to avoid bias, when using the fit functions to produce new results. The grade system is:

- Grade 1 - Status is CONVERGED for every turn-on curve,
- Grade 2 - Status is CONVERGED, OK or SUCCESSFUL for every turn-on curve and status is CONVERGED for at least 80% of the turn-on curves,
- Grade 3 - Status is CONVERGED, OK or SUCCESSFUL for at least 50% of the turn-on curves and PROBLEMS for the rest,
- Grade 4 - Status is CONVERGED, OK or SUCCESSFUL for at least 50% of the turn-on curves,
- Grade 5 - Status is not for every turn-on curve NOT POSDEF, CALL LIMIT or FAILED,
- Grade 6 - Status is NOT POSDEF, CALL LIMIT or FAILED for every turn-on curve.

The highest possible grade consistent with the criteria above is given to each combination of fit function, parameter limits and choice of initial values. The criterion to consider a fit function as suitable for the analysis is to be assigned at most grade 3 for one combination of initial values and parameter limits. With grade 3 or lower at least the minimum is found in each case, though in some cases there may have been problems in the process. After the analysis of the fit performance only initial value–parameter limit pairs with the highest reliability are considered for each fit function.

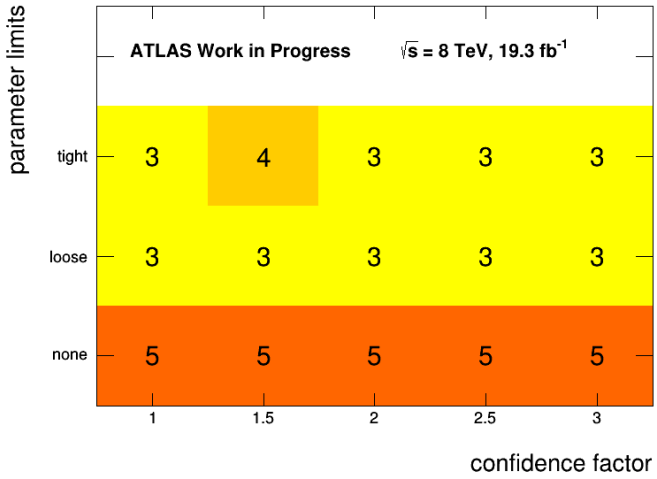

Figure 5.1: Minimisation performance of the MEF. The performance of the MEF depending on the choice of initial values through the confidence factor x and the choice of parameter limits is illustrated with grades, where a lower grade corresponds to a better performance.

5.1.1 Error function performance

The error function (equation 4.2) shows a very reliable performance independent of the choice of initial values and parameter limits. For every turn-on curve considered and with each of the 15 combinations of sets of parameter limits and initial values the minimisation converged (grade 1).

5.1.2 MEF performance

The MEF performance is sensitive to the choice of initial values and parameter limits as shown in figure 5.1. Most of the combinations of parameter limits and initial values pass the minimal requirement of reliability, but none of them come close to the performance of the error function. The minimisation without parameter limits is very unreliable.

The MEF shows the most reliable minimisation for $x = 3$ and tight parameter limits followed by $x = 3$ and loose parameter limits. For both of the combinations the minimisation always converges. However, in both cases between 30% and 40% of the minimisation problems converge only with problems.

The uncertainties calculated by varying the MEF parameter errors independently can have values of more than 100%, as can be seen in table 5.1. These very implausible results stem from the fact that this method does not respect the correlation between the fit parameters. The effect of the correlations is especially pronounced because of the high number of fit parameters. Thus the uncertainty estimation with the MEF is usable only with one of the newly developed error estimation methods. Whether the MEF is suitable for the analysis of E_T^{miss}-trigger efficiencies depends therefore on the performance of these methods.

5.1.3 SEF performance

Similar to the MEF, the performance of the minimisation problems with the SEF depends both on the choice of initial values and on the parameter limits. This is illustrated in figure 5.2. The minimisation performance of the SEFi and the SEFb are very similar to the SEF performance[1]. The minimisation problems with any of the SEF-like functions do not converge as reliably as demanded in section 5.1 regardless of parameter limits and initial values. Without further

[1]Figures illustrating that can be found in appendix C.

Table 5.1: Systematic uncertainties of a selection of signal trigger efficiencies in $Z \to \mu\mu$ data taken in 2015 at $\sqrt{s} = 13$ TeV with the E_T^{miss} spectrum of a gluino R-hadron signal sample with $m_{\tilde{g}} = 800$ GeV. The uncertainties were obtained with MEF fits and by varying the parameter errors independently as it was done in 2012.

trigger item	uncertainty
HLT_xe70	23.7%
HLT_xe80_L1XE70	38.7%
HLT_xe80	101%
HLT_xe100_mht	13.3%
HLT_xe100	41.5%

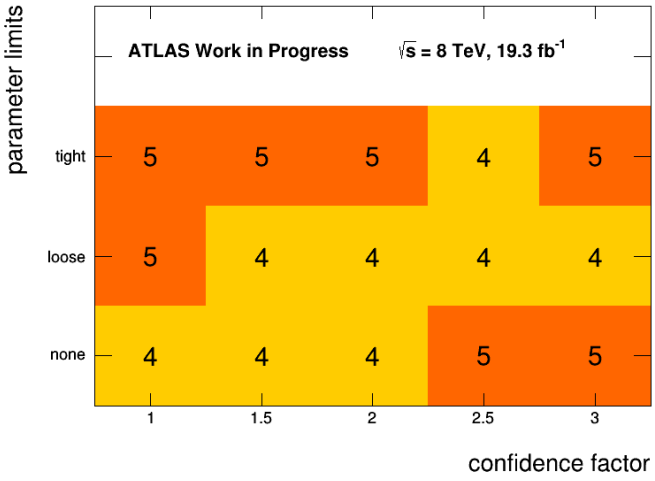

Figure 5.2: Minimisation performance of the SEF. The performance of the SEF depending on the choice of initial values through the confidence factor x and the choice of parameter limits is illustrated with grades, where a lower grade corresponds to a better performance.

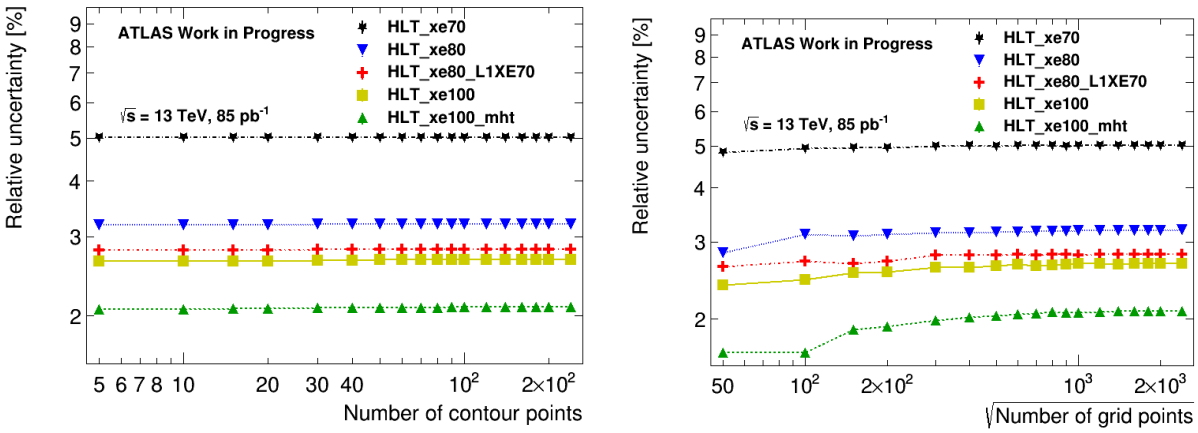

Figure 5.3: Systematic uncertainties of the signal trigger efficiency of a gluino R-hadron signal sample with $m_{\tilde{g}} = 800$ GeV simulated at $\sqrt{s} = 13$ TeV. Uncertainties, estimated with the contour method, of the triggers HLT_xe70 (black long dashed dotted line, black stars), HLT_xe80 (blue dotted line, blue triangles), HLT_xe80_L1XE70 (red dashed dotted line, red crosses), HLT_xe100 (yellow solid line, yellow squares), HLT_xe100_mht (green dashed line, green triangles pointing up) depending on the number of contour points (left). Uncertainties, estimated with the grid method, of the triggers HLT_xe70 (black long dashed dotted line, black stars), HLT_xe80 (blue dotted line, blue triangles), HLT_xe80_L1XE70 (red dashed dotted line, red crosses), HLT_xe100 (yellow solid line, yellow squares), HLT_xe100_mht (green dashed line, green triangles pointing up) depending on the grid resolution (right).

improvement of the methods to determine initial values and parameter limits these function are not suited for the parametrisation of the turn-on curves considered in this work.

5.1.4 GF performance

In case of the GF there is only one set of parameter limits and initial values. Its performance is graded as a 4, which means it is not suitable for the analysis. To improve this a better interpretation of the GF in the context of E_T^{miss}-trigger event selection is needed. Even if parameter limits and initial values with a better performance would be found by testing a large number of randomly chosen combinations, it is not clear, whether the event selection wit a trigger item used in the future can be parametrised the same way.

5.2 Performance of the contour method

The contour as calculated with the Root-function `MnContour` of TMinuit [59] is determined by solving a number of minimisation problems for a subset of the fit parameters. These solutions may or may not converge leading to, in some cases incomplete, contours. There also remains the question, which would be the right amount of points on the contour n_c to be demanded. For the error function the uncertainty calculated with the contour method using n_c points on the contour is depicted in figure 5.3 (left).

The uncertainty does converge very quickly in all cases tested in this work. For $n_c \geq 90$ the uncertainty changes on a scale smaller than 10^{-5}%. Thus it is concluded that $n_c = 90$ is more than sufficient to calculate systematic uncertainties with a high precision at least in the case of an error function fit[2].

[2]In appendix D a table, supporting that choice, can be found.

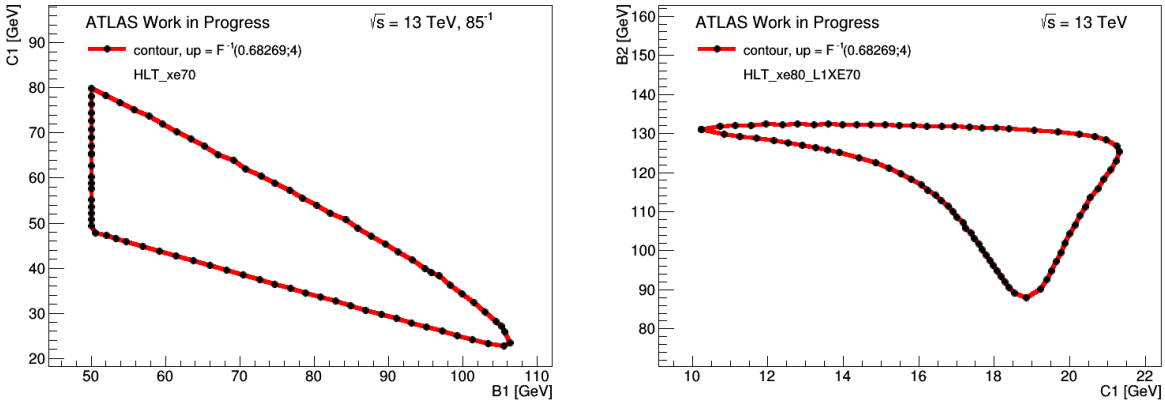

Figure 5.4: B_1–C_1 contour of constant $\chi^2 = \chi^2_{min} + F^{-1}(0.68269; 4)$ for a MEF fit to the turn-on curve of the trigger HLT_xe70 in $Z \to \mu\mu$ events in data taken in 2015 at $\sqrt{s} = 13$ TeV (black dots, red solid line) (left). C_1–B_2 contour of constant $\chi^2 = \chi^2_{min} + F^{-1}(0.68269; 4)$ for a MEF fit to the turn-on curve of the trigger HLT_xe80_L1XE70 in $Z \to \mu\mu$ events simulated at $\sqrt{s} = 13$ TeV (black dots, red solid line) (right).

5.2.1 Error function contours

Error function contours can be seen in figures 4.8, 4.9 and 4.10 in section 4.4.3. For the error function regardless of initial values and parameter limits a contour with 90 points is always returned.

5.2.2 MEF contours

To estimate the systematic uncertainty using the contour method with MEF fits, the contours have to hint at a simple shape (hypersphere, hyperellipsoid, etc.) for each of the six parameter pairs. A hypersurface[3] with a simple shape could also be specified as a simple mathematical expression. Then the contour points could be used to interpolate that surface and construct points in parameter space through which the uncertainty can be calculated via maximisation.

In figure 5.4 (left) an example of a contour with a nearly elliptic shape interrupted by a parameter limit is shown. The parameter limit as a limit to the contour is no problem for the method, since the points can, together with the other five contours, be used to construct a part of a hyperellipsoid with a truncated side. In roughly 20% of the cases tested in this work the function `MnContours` returns a contour of similar shape, hinting at a hyperellipsoid or truncated hyperellipsoid.

The other contour depicted in figure 5.4 (right) is more problematic, because of its complex shape. To construct a hypersurface from this contour and the five other contours for this trigger would be difficult and therefore error-prone.

Another typical example of a MEF contour is depicted in figure 5.5. Not only is the shape of the contour very complex, but also are the points on the contour ordered incorrectly, which can be seen from the connecting lines between the points on the contour. In principle it is not problematic for the points to have a different order or to even have points determined to be inside the contour. Since the uncertainty is estimated via maximisation, it is almost irrelevant that a small number of points is inside the contour. However, a large number of points irrelevant to the uncertainty estimation has a negative effect on the precision. The most striking problem here is that such imperfections in the determination of the contour cast doubt on the credibility of the result. Contours of similar shape or of high complexity, as in the example above, are constructed in about 20% of the tested cases.

[3]It is noteworthy that this is a three dimensional surface embedded in a four dimensional parameter space.

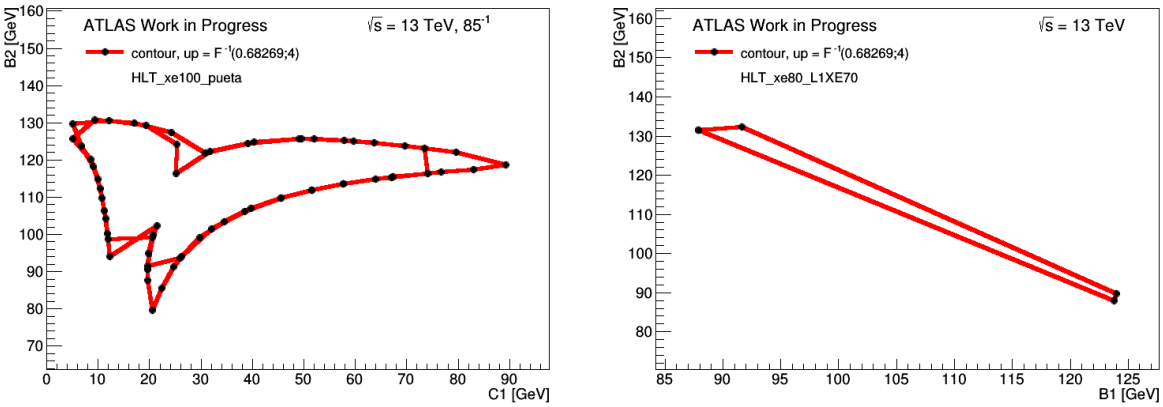

Figure 5.5: C_1–B_2 contour of constant $\chi^2 = \chi^2_{min} + F^{-1}(0.68269; 4)$ for a MEF fit to the turn-on curve of the trigger HLT_xe100_pueta in $Z \to \mu\mu$ events in data taken in 2015 at $\sqrt{s} = 13$ TeV (black dots, red solid line) (left). B_1–B_2 contour of constant $\chi^2 = \chi^2_{min} + F^{-1}(0.68269; 4)$ for a MEF fit to the turn-on curve of the trigger HLT_xe80_L1XE70 in $Z \to \mu\mu$ events simulated at $\sqrt{s} = 13$ TeV (black dots, red solid line) (right).

It is even more problematic, if only a few points of the contour are determined. An example of this is depicted in figure 5.5. In many cases the function `MnContours` does not return a contour at all. Obviously both cases make the determination of systematic uncertainties with this method entirely impossible. In 35% of the cases tested in this work a contour with less than 30 points is returned and for another 25% of the cases the construction of the contour failed completely.

A combination of initial values and parameter limits, where these cases happen most rarely, is determined among the combinations with a sufficient minimisation performance. The so determined combination $x = 2.5$ and tight parameter limits was used for the minimisation in figure 5.4 and figure 5.5.

5.3 Performance of the grid method

Analogous to the contour method the minimal number of points on the grid n_g^d for a sufficient precision is determined.

5.3.1 Error function grid

In figure 5.3 the uncertainty of the efficiency of several trigger items depending on the grid resolution n_g is shown as calculated from error function fits. Above $N_g = 1800$ the uncertainty changes only on a scale of 10^{-3}% with increasing n_g. Thus $n_g = 1800$ is used for the error function fits[4]. An interesting feature, which can be seen in figure 5.3 is that the uncertainty does not increase monotonously, but can decrease from one data point to the next in some cases. The reason for that is that the grid points are defined to be equidistant and thus not every grid contains all the points contained in a grid with a fewer number of points. Therefore the point of largest efficiency can be "missed" while determining the grid. The probability for that to happen decreases with the number of grid points.

5.3.2 MEF grid

In figure 5.6 the uncertainty calculated with the grid method and MEF fits depending on the grid resolution is depicted. A tendency for the uncertainties to converge for large n_g can

[4]A table illustrating that choice can be found in appendixD.

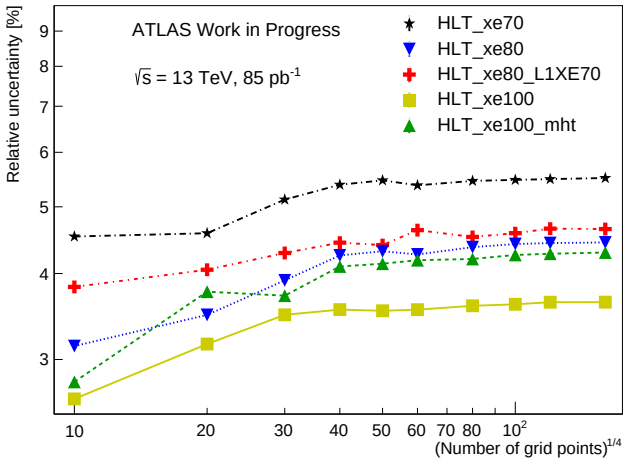

Figure 5.6: Systematic uncertainties of the signal trigger efficiency of a gluino R-hadron signal sample with $m_{\tilde{g}} = 800$ GeV simulated at $\sqrt{s} = 13$ TeV. Uncertainties, estimated with the contour method, of the triggers HLT_xe70 (black long dashed dotted line, black stars), HLT_xe80 (blue dotted line, blue triangles), HLT_xe80_L1XE70 (red dashed dotted line, red crosses), HLT_xe100 (yellow solid line, yellow squares), HLT_xe100_mht (green dashed line, green triangles pointing up) depending on the number of contour points.

be seen. However, the value of n_g, at which the uncertainties do not change significantly, is not reached in figure 5.6. Larger values for n_g are not tested, since the computation time is already at the order of days on a local machine for $n_g = 120$.

The problem with the usage of the grid method for MEF fits is the fast increase of the computation time with n_g^4. Thus demanding higher precision can possibly lead to a bad use of resources. Given that the grid method is the only method tested in this work to be able to determine systematic uncertainties from MEF fits this might be necessary regardless.

5.4 Estimation of trigger efficiencies used in 2012

In figure 5.7 the signal trigger efficiency of the trigger EF_xe80_tclcw_loose depending on the gluino mass of the signal sample is depicted. The systematic uncertainties calculated with the contour method are shown as error bars, which are smaller than the marker size for multiple gluino masses. The trigger efficiency shows a dependence on the gluino mass, because of the mass dependence of the production processes. Up to a mass of 600 GeV the production is dominated by gluon-gluon fusion. For higher masses the dominant production process is quark-antiquark annihilation. How often the production process causes ISR and thus E_T^{miss} depends on the gluino mass in both cases.

The efficiency values and systematic uncertainties of the trigger EF_xe80_tclcw_loose estimated with the three methods are listed in table 5.2. The uncertainties calculated with the new methods surpass the uncertainties calculated with the 2012 method by factors around 1.1. Furthermore, the contour method and the grid method lead to very similar results as expected, which is a good consistency check.

5.5 Trigger efficiencies after the long shutdown

Both the signal trigger efficiencies of the trigger EF_xe80_tclcw_loose and the trigger HLT_xe100_mht are shown in figure 5.7. For the efficiency of the HLT_xe100_mht only a small dependence on the gluino mass can be seen. The reason for that is possibly the higher

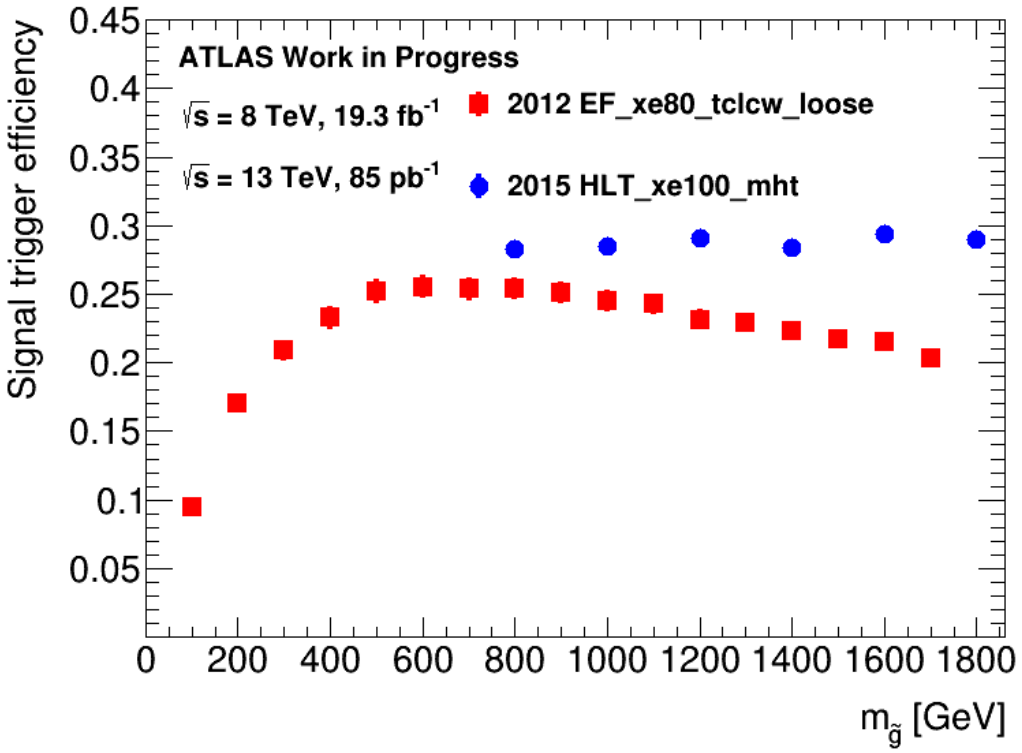

Figure 5.7: Gluino R-hadron signal trigger efficiencies for several gluino masses. Lowest unprescaled trigger in late 2012 EF_xe80_tclcw_loose (red squares) and a trigger used after the long shutdown HLT_xe100_mht (blue dots). The error bars correspond to the uncertainties calculated with the contour method.

Table 5.2: Efficiencies and systematic uncertainties of the trigger EF_xe80_tclcw_loose in gluino R-hadron signal samples simulated at $\sqrt{s} = 8$ TeV estimated with the three methods described above.

$m_{\tilde{g}}$	2012 method	contour method	grid method
100	0.0942 ± 0.0041	0.0942 ± 0.0047	0.0942 ± 0.0047
200	0.1702 ± 0.0065	0.1702 ± 0.0072	0.1702 ± 0.0072
300	0.2090 ± 0.0067	0.2090 ± 0.0076	0.2090 ± 0.0075
400	0.2327 ± 0.0075	0.2327 ± 0.0083	0.2327 ± 0.0082
500	0.2522 ± 0.0080	0.2522 ± 0.0088	0.2522 ± 0.0087
600	0.2552 ± 0.0075	0.2552 ± 0.0083	0.2552 ± 0.0082
700	0.2535 ± 0.0075	0.2535 ± 0.0083	0.2535 ± 0.0082
800	0.2541 ± 0.0074	0.2541 ± 0.0081	0.2541 ± 0.0081
900	0.2508 ± 0.0073	0.2508 ± 0.0080	0.2508 ± 0.0079
1000	0.2450 ± 0.0072	0.2450 ± 0.0079	0.2450 ± 0.0079
1100	0.2428 ± 0.0069	0.2428 ± 0.0076	0.2428 ± 0.0075
1200	0.2315 ± 0.0066	0.2315 ± 0.0073	0.2315 ± 0.0072
1300	0.2292 ± 0.0066	0.2292 ± 0.0073	0.2292 ± 0.0072
1400	0.2230 ± 0.0064	0.2230 ± 0.0071	0.2230 ± 0.0070
1500	0.2176 ± 0.0059	0.2176 ± 0.0066	0.2176 ± 0.0066
1600	0.2147 ± 0.0062	0.2147 ± 0.0068	0.2147 ± 0.0068
1700	0.2035 ± 0.0057	0.2035 ± 0.0064	0.2035 ± 0.0063

Table 5.3: Efficiencies and systematic uncertainties of the trigger HLT_xe70 in gluino R-hadron signal samples simulated at $\sqrt{s} = 13$ TeV estimated with the three methods described above.

$m_{\tilde{g}}$	2012 method	contour method	grid method
800	0.3182 ± 0.0158	0.3182 ± 0.0160	0.3182 ± 0.0159
1000	0.3223 ± 0.0168	0.3223 ± 0.0170	0.3223 ± 0.0170
1200	0.3306 ± 0.0160	0.3306 ± 0.0162	0.3306 ± 0.0162
1400	0.3219 ± 0.0158	0.3219 ± 0.0161	0.3219 ± 0.0161
1600	0.3323 ± 0.0154	0.3323 ± 0.0156	0.3323 ± 0.0156
1800	0.3266 ± 0.0157	0.3266 ± 0.0159	0.3266 ± 0.0159

Table 5.4: Efficiencies and systematic uncertainties of the trigger HLT_xe100_mht in gluino R-hadron signal samples simulated at $\sqrt{s} = 13$ TeV estimated with the three methods described above.

$m_{\tilde{g}}$	2012 method	contour method	grid method
800	0.2830 ± 0.0054	0.2830 ± 0.0059	0.2830 ± 0.0059
1000	0.2849 ± 0.0057	0.2849 ± 0.0062	0.2849 ± 0.0062
1200	0.2906 ± 0.0054	0.2906 ± 0.0059	0.2906 ± 0.0059
1400	0.2841 ± 0.0055	0.2841 ± 0.0060	0.2841 ± 0.0060
1600	0.2934 ± 0.0054	0.2934 ± 0.0060	0.2934 ± 0.0060
1800	0.2899 ± 0.0053	0.2899 ± 0.0058	0.2899 ± 0.0058

centre-of-mass energy, which might stretch the distribution to higher gluino masses. Therefore the part of the distribution depicted here could be the region, where the efficiency is the largest.

Furthermore, the E_T^{miss}-trigger efficiencies are strictly larger for the trigger used after the long shutdown, despite having a higher E_T^{miss}-threshold. This shows that the higher centre-of-mass energy also makes the generation of large E_T^{miss} more likely. In tables 5.3–5.4 the efficiencies and systematic uncertainties of the triggers HLT_xe70 and HLT_xe100_mht estimated with the three methods are listed[5]. Similarly to the result for the trigger EF_xe80_tclcw_loose the uncertainties are slightly larger, when estimated with one of the new methods. Furthermore, the contour method and the grid method lead to similar results.

[5]The efficiencies and systematic uncertainties of the other triggers tested in this work can be found in appendix E.

Chapter 6

Conclusion and Outlook

Studies of E_T^{miss} triggers for the search for SMPs with the ATLAS detector in the near future wear conducted. Compared to the most recent search [24] the signal trigger efficiencies for gluino R-hadrons are found to increase from values up to 0.26 to values as large as 0.29 for comparable E_T^{miss}-triggers.

Additionally, new methods to estimate systematic uncertainties were developed and new fit functions to parametrise the E_T^{miss} trigger turn-on curves were studied. Both the contour method and the grid method are shown to be useful as ways to estimate systematic uncertainties. Other than the previously used method they respect the likelihood of fit results, correlation between fit parameters and correct probability intervals in the uncertainty estimation. The contour method has an advantage over the grid method, due to the better use of computation time.

Among the new fit functions only the MEF shows a sufficient performance, while neither the SEF-like functions nor the GF can be recommended for the parametrisation without further modifications. However, the only method to estimate systematic uncertainties from MEF fits the grid method shows a very bad use of computation time, when requiring a sufficient precision of the method. Therefore the uncertainty estimation with the error function using the contour method is recommended for the search for SMPs with the ATLAS detector.

The applicability of the new uncertainty estimation methods reaches further than the search for SMPs alone. They can in principle be used for uncertainty estimations of any value, which is determined through a parametrisation. They are however only tested for the functions presented in this work and are problematic for fit functions with more than two fit parameters.

Using the contour method the systematic uncertainties increase by factors of about 1.1 for data taken in 2012 compared to the previously used method to calculate uncertainties. For the efficiencies of the triggers used in 2015 the uncertainties range between 2.0% and 5.3%.

Judging from the new higher signal trigger efficiencies, the search for SMPs with the ATLAS detector after the long shutdown looks promising. The increase of the uncertainties with the use of the contour method is not expected to be very hurtful to the analysis on that scale. Though larger systematic uncertainties might seem unfortunate, it is on the whole positive, to have a better understanding of the systematic effects.

Acknowledgements

I thank the CERN and the ATLAS collaboration for providing me with simulations, software, data and allowing me to be part of the history of particles physics. I am thankful to my supervisor Sascha Mehlhase for providing me with more simulations, answers to my many questions as well as valuable insight into particle physics and distractions from work. It was also pleasure to work with Jochen Heinrich and Michael Adersberger, who were always helpful and proved to me that one can be both passionate about physics and sometimes not take it too seriously. I also thank Dorothee Schaile for giving me the opportunity to be part of a great team of all the dedicated scientists at her chair.

Also I would like to thank my friends and my family for always being supportive and understanding for my lack of time in the last weeks of my thesis. Finally, I am grateful for the proofreading of endless passages of tiring physics thesis text my sister went through. And I thank my mum for making my life easy enough to fully be able to concentrate on my work.

List of Figures

List of Tables

Bibliography

[1] The CDF collaboration. "Observation of top quark production in $\bar{p}p$ collisions with the collider detector at fermilab". In: *Physical review letters* 74.14 (1995), p. 2626.

[2] The D0 collaboration. "Observation of the top quark". In: *Physical Review Letters* 74.14 (1995), p. 2632.

[3] The DONUT collaboration. "Observation of tau neutrino interactions". In: *Phys. Lett.* B504 (2001), pp. 218–224. DOI: 10.1016/S0370-2693(01)00307-0. arXiv: hep-ex/0012035 [hep-ex].

[4] The ATLAS collaboration. "Observation of a new particle in the search for the Standard Model Higgs boson with the ATLAS detector at the LHC". In: *Physics Letters B* 716.1 (2012), pp. 1–29.

[5] The CMS collaboration. "Observation of a new boson at a mass of 125 GeV with the CMS experiment at the LHC". In: *Physics Letters B* 716.1 (2012), pp. 30–61.

[6] The Planck collaboration. "Planck 2013 results. I. Overview of products and scientific results". In: *Astronomy & Astrophysics* 571 (2014), A1.

[7] Raymond Davis Jr, Don S Harmer and Kenneth C Hoffman. "Search for neutrinos from the sun". In: *Physical Review Letters* 20.21 (1968), p. 1205.

[8] The Super-Kamiokande collaboration. "Evidence for oscillation of atmospheric neutrinos". In: *Physical Review Letters* 81.8 (1998), p. 1562.

[9] The SNO collaboration. "Measurement of the Rate of $\nu_e + d \rightarrow p + p + e^-$ Interactions Produced by B 8 Solar Neutrinos at the Sudbury Neutrino Observatory". In: *Physical Review Letters* 87.7 (2001), p. 071301.

[10] Pierre Binétruy. *Supersymmetry: theory, experiment, and cosmology*. Oxford University Press, 2012.

[11] Julius Wess and Bruno Zumino. "A Lagrangian model invariant under supergauge transformations". In: *Phys. Lett. B* 49.CERN-TH-1794 (1973), pp. 52–54.

[12] Nima Arkani-Hamed and Savas Dimopoulos. "Supersymmetric unification without low energy supersymmetry and signatures for fine-tuning at the LHC". In: *JHEP* 06 (2005), p. 073. DOI: 10.1088/1126-6708/2005/06/073. arXiv: hep-th/0405159 [hep-th].

[13] Michael Dine and Ann E. Nelson. "Dynamical supersymmetry breaking at low-energies". In: *Phys. Rev.* D48 (1993), pp. 1277–1287. DOI: 10.1103/PhysRevD.48.1277. arXiv: hep-ph/9303230 [hep-ph].

[14] Andrea De Simone et al. "Leptogenic Supersymmetry". In: *Phys. Rev.* D80 (2009), p. 035010. DOI: 10.1103/PhysRevD.80.035010. arXiv: 0903.5305 [hep-ph].

[15] Keith R. Dienes, Emilian Dudas and Tony Gherghetta. "Extra space-time dimensions and unification". In: *Phys. Lett.* B436 (1998), pp. 55–65. DOI: 10.1016/S0370-2693(98)00977-0. arXiv: hep-ph/9803466 [hep-ph].

[16] Thomas Appelquist, Hsin-Chia Cheng and Bogdan A. Dobrescu. "Bounds on universal extra dimensions". In: *Phys. Rev.* D64 (2001), p. 035002. DOI: 10.1103/PhysRevD.64.035002. arXiv: hep-ph/0012100 [hep-ph].

[17] C. Friberg, E. Norrbin and T. Sjostrand. "QCD aspects of leptoquark production at HERA". In: *Phys. Lett.* B403 (1997), pp. 329–334. DOI: 10.1016/S0370-2693(97)00543-1. arXiv: hep-ph/9704214 [hep-ph].

[18] Tao Han et al. "Phenomenology of hidden valleys at hadron colliders". In: *Journal of High Energy Physics* 2008.07 (2008), p. 008.

[19] Gian Francesco Giudice and Riccardo Rattazzi. "Theories with gauge-mediated supersymmetry breaking". In: *Physics Reports* 322.6 (1999), pp. 419–499.

[20] Enrique Kajomovitz, ed. *New Physics at the LHC: results and Run II perspectives.* 12th Dec. 2014.

[21] Malcolm Fairbairn et al. "Stable massive particles at colliders". In: *Physics reports* 438.1 (2007), pp. 1–63.

[22] The ATLAS Collaboration. *ATLAS level-1 trigger: Technical Design Report.* Technical Design Report ATLAS. Geneva: CERN, 1998. URL: http://cds.cern.ch/record/381429.

[23] The ATLAS Collaboration. *ATLAS high-level trigger, data-acquisition and controls: Technical Design Report.* Technical Design Report ATLAS. Geneva: CERN, 2003. URL: http://cds.cern.ch/record/616089.

[24] The ATLAS Collaboration. "Searches for heavy long-lived charged particles with the ATLAS detector in proton-proton collions at $\sqrt{s} = 8$ TeV". In: *Journal of high energy physics* 2015.1 (2015), pp. 1–51.

[25] David Griffiths. *Introduction to elementary particles.* 2008.

[26] K. A. Olive et al. "Review of Particle Physics". In: *Chin. Phys.C* 38 (2014), p. 090001. DOI: 10.1088/1674-1137/38/9/090001.

[27] Georges Aad et al. "Combined Measurement of the Higgs Boson Mass in pp Collisions at $\sqrt{s} = 7$ and 8 TeV with the ATLAS and CMS Experiments". In: *Phys. Rev. Lett.* 114 (2015), p. 191803. DOI: 10.1103/PhysRevLett.114.191803. arXiv: 1503.07589 [hep-ex].

[28] S. Dittmaier et al. "Handbook of LHC Higgs Cross Sections: 2. Differential Distributions". In: (2012). DOI: 10.5170/CERN-2012-002. arXiv: 1201.3084 [hep-ph].

[29] Emmy Noether. "Invariante variationsprobleme". In: *Nachrichten von der Gesellschaft der Wissenschaften zu Göttingen, mathematisch-physikalische Klasse* 1918 (1918), pp. 235–257.

[30] Franz Mandl and Graham Shaw. *Quantum field theory.* John Wiley & Sons, 2010.

[31] The LHCb collaboration. "Observation of $J/\psi p$ resonances consistent with pentaquark states in $\Lambda_b^0 \to J/\psi K^- p$ decays". In: (2015). arXiv: 1507.03414 [hep-ex].

[32] TJ Humanic. "Extracting the hadronization timescale in $\sqrt{s} = 7$ TeV proton–proton collisions from pion and kaon femtoscopy". In: *Journal of Physics G: Nuclear and Particle Physics* 41.7 (2014), p. 075105.

[33] Klaus Bethge and Ulrich E Schröder. *Elementarteilchen und ihre Wechselwirkungen.* John Wiley & Sons, 2012.

[34] Laurent Canetti, Marco Drewes and Mikhail Shaposhnikov. "Matter and Antimatter in the Universe". In: *New J. Phys.* 14 (2012), p. 095012. DOI: 10.1088/1367-2630/14/9/095012. arXiv: 1204.4186 [hep-ph].

[35] S. P. Martin. "A Supersymmetry Primer". In: *Perspectives On Supersymmetry. Series: Advanced Series on Directions in High Energy Physics. WORLD SCIENTIFIC, Edited by Gordon L Kane, vol. 18, pp. 1-98* 18 (July 1998), pp. 1–98. DOI: 10.1142/9789812839657_0001. eprint: hep-ph/9709356.

[36] LS Schaile LMU Munich. *Supersymmetry*. Ed. by Alexander Mann. 2015. URL: http://www.etp.physik.uni-muenchen.de/research/atlas/susy/index.html.

[37] Theodor Kaluza. "Zum unitätsproblem der physik". In: *Sitzungsber. Preuss. Akad. Wiss. Berlin.(Math. Phys.)* 1921.966972 (1921), p. 45.

[38] Geraldine Servant and Timothy M. P. Tait. "Is the lightest Kaluza-Klein particle a viable dark matter candidate?" In: *Nucl. Phys.* B650 (2003), pp. 391–419. DOI: 10.1016/S0550-3213(02)01012-X. arXiv: hep-ph/0206071 [hep-ph].

[39] Bruno Rossi and David B Hall. "Variation of the rate of decay of mesotrons with momentum". In: *Physical Review* 59.3 (1941), p. 223.

[40] Lyndon Evans and Philip Bryant. "LHC machine". In: *JINST* 3 (2008), S08001.

[41] The ATLAS Collaboration. *Luminosity Public Results*. Ed. by Guillaume Unal and Luca Fiorini. 2015. URL: https://twiki.cern.ch/twiki/bin/view/AtlasPublic/LuminosityPublicResults.

[42] The ATLAS Collaboration. *Luminosity Public Results*. Ed. by Eric Torrence. 2015. URL: https://twiki.cern.ch/twiki/bin/view/AtlasPublic/LuminosityPublicResultsRun2.

[43] The ATLAS collaboration. "The ATLAS experiment at the CERN large hadron collider". In: *Journal of Instrumentation* 3.08 (2008), S08003.

[44] The ATLAS collaboration. "ATLAS pixel detector electronics and sensors". In: *Journal of Instrumentation* 3.07 (2008), P07007.

[45] Y. Unno representing the ATLAS SCT collaboration. "ATLAS silicon microstrip Semiconductor Tracker (SCT)". In: *Nuclear Instruments and Methods in Physics Research Section A: Accelerators, Spectrometers, Detectors and Associated Equipment* 453.1 (2000), pp. 109–120.

[46] The ATLAS TRT collaboration. "The ATLAS Transition Radiation Tracker (TRT) proportional drift tube: design and performance". In: *Journal of Instrumentation* 3.02 (2008), P02013.

[47] Georges Aad et al. "Performance of Missing Transverse Momentum Reconstruction in Proton-Proton Collisions at 7 TeV with ATLAS". In: *Eur. Phys. J.* C72 (2012), p. 1844. DOI: 10.1140/epjc/s10052-011-1844-6. arXiv: 1108.5602 [hep-ex].

[48] *ATLAS tile calorimeter: Technical Design Report*. Tech. rep. 1996. URL: http://cds.cern.ch/record/331062.

[49] *dE/dx measurement in the ATLAS Pixel Detector and its use for particle identification*. Tech. rep. ATLAS-CONF-2011-016. Geneva: CERN, Mar. 2011. URL: http://cds.cern.ch/record/1336519.

[50] Michael Adersberger. "Studies on Velocity Measurements with the ATLAS Calorimeters for the Search for Heavy Long-Lived Particles". Master. LMU Munich, 2015.

[51] Stefano Frixione, Paolo Nason and Carlo Oleari. "Matching NLO QCD computations with Parton Shower simulations: the POWHEG method". In: *JHEP* 11 (2007), p. 070. DOI: 10.1088/1126-6708/2007/11/070. arXiv: 0709.2092 [hep-ph].

[52] Torbjorn Sjostrand, Stephen Mrenna and Peter Z. Skands. "PYTHIA 6.4 Physics and Manual". In: *JHEP* 05 (2006), p. 026. DOI: 10.1088/1126-6708/2006/05/026. arXiv: hep-ph/0603175 [hep-ph].

[53] Rasmus Mackeprang. “Stable heavy hadrons in ATLAS”. PhD thesis. University of Copenhagen, 2007.

[54] Aafke Christine Kraan. “Interactions of heavy stable hadronizing particles”. In: *Eur. Phys. J.* C37 (2004), pp. 91–104. DOI: 10.1140/epjc/s2004-01997-7. arXiv: hep-ex/0404001 [hep-ex].

[55] A Marzin, ed. *Trigger menu for Run 2*. 16th Apr. 2014.

[56] ROOT CERN. *TGraphAsymmErrors*. 2015. URL: https://root.cern.ch/root/html/TGraphAsymmErrors.html.

[57] ROOT CERN. *TEfficiency*. 2015. URL: https://root.cern.ch/root/html/TEfficiency.html#TEfficiency:ClopperPearson.

[58] Larry C. Andrews. *Special Functions of Mathematics for Engineers*. 1998.

[59] Fred James and Matthias Winkler. “Minuit user’s guide”. In: *CERN, Geneva* 23 (2004).

[60] Jun Han and Claudio Moraga. “The influence of the sigmoid function parameters on the speed of backpropagation learning”. English. In: *From Natural to Artificial Neural Computation*. Ed. by Jose Mira and Francisco Sandoval. Vol. 930. Lecture Notes in Computer Science. Springer Berlin Heidelberg, 1995, pp. 195–201. ISBN: 978-3-540-59497-0. DOI: 10.1007/3-540-59497-3_175. URL: http://dx.doi.org/10.1007/3-540-59497-3_175.

[61] The ATLAS collaboration. *MetTriggerStudiesPileup*. Ed. by P. H. Beauchemin. 2014. URL: https://twiki.cern.ch/twiki/bin/viewauth/Atlas/MetTriggerStudiesPileup.

[62] Fred James. *The interpretation of errors*. 2004.

[63] Frederick James. *Statistical methods in experimental physics*. World Scientific, 2006.

Appendices

Appendix A

Data and simulated samples

Table A.1: Simulation tags of the MC samples used in this work.

MC sample	Simulation tags
8 TeV $Z \to \mu\mu$	e1169, s1469, s1470, r3658
8 TeV gluino R-hadron	e1724, s1612, s1586, r4190
13 TeV $Z \to \mu\mu$	e3601, s2576, s2132, r6765, r6282
13 TeV gluino R-hadron $m_{\tilde{g}} \leq 1400$ GeV	e4085, s2673, s2183, r6793, r6264
13 TeV gluino R-hadron $m_{\tilde{g}} > 1400$ GeV	e4085, s2673, s2183, r6892, r6264

Appendix B

Example turn-on curves

Additional turn-on curves meant as comparisons to the turn-on curves in the main text are presented below in figures B.1–B.2.

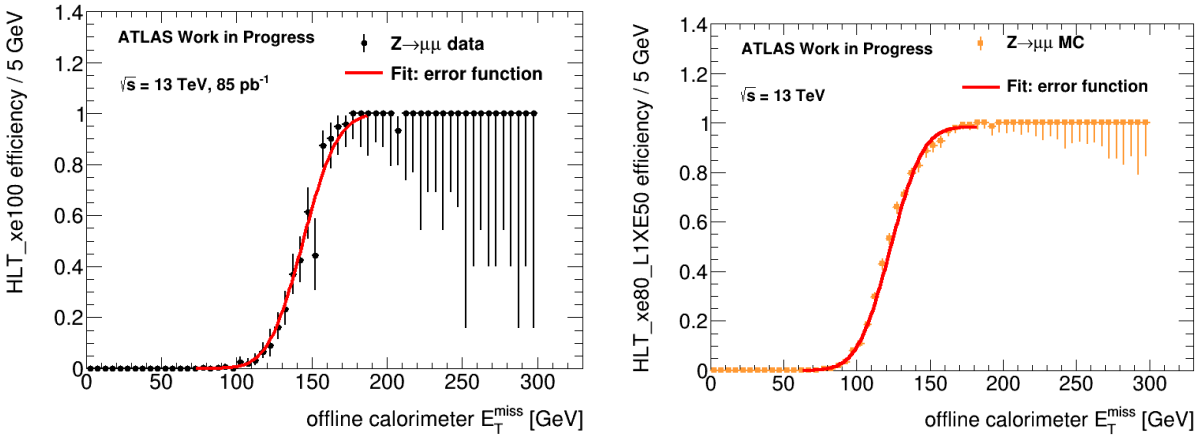

Figure B.1: Turn-on curve of the trigger HLT_xe100 for $Z \to \mu\mu$ selected events in data taken in 2015 at $\sqrt{s} = 13$ TeV (orange squares). Error function fit (red solid line) to the data points (left). Turn-on curve of the trigger HLT_xe80_L1XE50 for $Z \to \mu\mu$ selected events in a MC simulated $Z \to \mu\mu$ sample at $\sqrt{s} = 13$ TeV (orange squares). Error function fit (red solid line) to the data points (right).

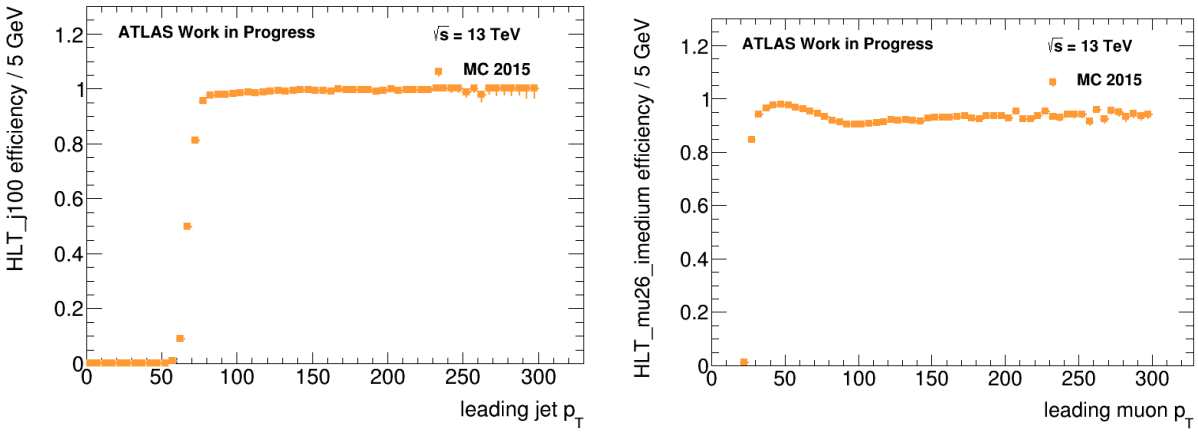

Figure B.2: Turn-on curve of the trigger HLT_j100 for $Z \to \mu\mu$ selected events in a $Z \to \mu\mu$ sample simulated at $\sqrt{s} = 13$ TeV (left). Turn-on curve of the trigger HLT_mu26_imedium for $Z \to \mu\mu$ selected events in a MC simulated $Z \to \mu\mu$ sample at $\sqrt{s} = 13$ TeV (right).

Appendix C

Fit function performances

The performance of the two remaining fit functions is illustrated in figures C.1–C.2.

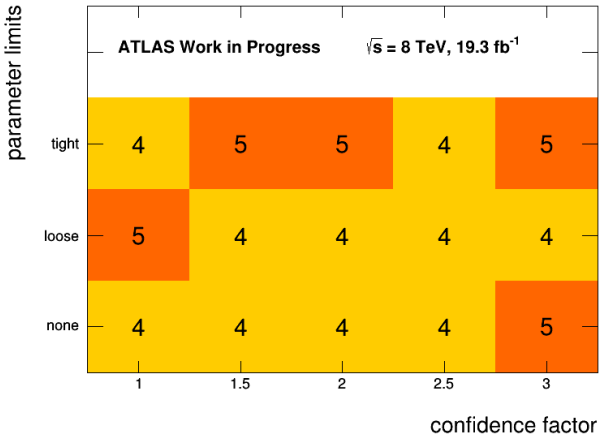

Figure C.1: Minimisation performance of the SEFi. The performance of the SEFi depending on the choice of initial values through the confidence factor x and the choice of parameter limits is illustrated with grades, where a lower grade corresponds to a better performance.

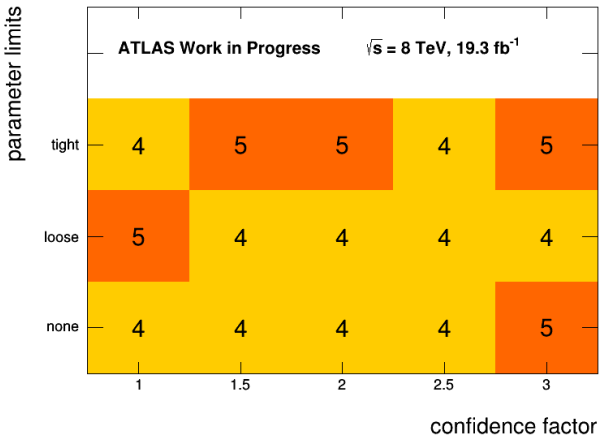

Figure C.2: Minimisation performance of the SEFb. The performance of the SEFb depending on the choice of initial values through the confidence factor x and the choice of parameter limits is illustrated with grades, where a lower grade corresponds to a better performance.

Appendix D

Performance of the uncertainty estimation methods

Supplementary material on the precision of the newly developed uncertainty estimation methods can be found in table D.1.

Table D.1: Relative systematic uncertainties of the trigger HLT_xe100_mht in gluino *R*-hadron signal samples simulated at $\sqrt{s} = 8$ TeV estimated with contour and grid method described above. The number of contour points n_c and the grid precision n_g is varied from 5 to 240 and from 50 to 2400, respectively.

n_c	contour uncertainty	n_g	grid uncertainty
5	2.06674%	50	1.67445%
10	2.06674%	100	1.67317%
15	2.07320%	150	1.89106%
20	2.07320%	200	1.91999%
30	2.08259%	300	1.98298%
40	2.08259%	400	2.01773%
50	2.08389%	500	2.03276%
60	2.08499%	600	2.05050%
70	2.08499%	700	2.05971%
80	2.08499%	800	2.07101%
90	2.08745%	900	2.06586%
100	2.08745%	1000	2.06759%
120	2.08745%	1200	2.07365%
140	2.08745%	1400	2.08210%
160	2.08745%	1600	2.08131%
180	2.08745%	1800	2.08071%
200	2.08745%	2000	2.08206%
240	2.08745%	2400	2.08098%

Appendix E

Efficiencies and systematic uncertainties of the trigger items under study

The signal trigger efficiencies not presented in section 5 are listed below. The trigger efficiencies for data taken at 8 TeV can be found in tables E.1–E.4. Trigger efficiencies for the triggers used after the long shutdown are presented in tables E.5–E.13.

Table E.1: Efficiencies and systematic uncertainties of the trigger EF_xe80 in gluino R-hadron signal samples simulated at $\sqrt{s} = 8$ TeV estimated with the three methods described above.

$m_{\tilde{g}}$	2012 method	contour method	grid method
100	0.0564 ± 0.0018	0.0564 ± 0.0019	0.0564 ± 0.0019
200	0.1139 ± 0.0027	0.1139 ± 0.0032	0.1139 ± 0.0031
300	0.1484 ± 0.0028	0.1484 ± 0.0033	0.1484 ± 0.0033
400	0.1694 ± 0.0031	0.1694 ± 0.0036	0.1694 ± 0.0035
500	0.1854 ± 0.0032	0.1854 ± 0.0037	0.1854 ± 0.0037
600	0.1897 ± 0.0030	0.1897 ± 0.0036	0.1897 ± 0.0036
700	0.1905 ± 0.0030	0.1905 ± 0.0036	0.1905 ± 0.0036
800	0.1911 ± 0.0030	0.1911 ± 0.0035	0.1911 ± 0.0035
900	0.1886 ± 0.0029	0.1886 ± 0.0035	0.1886 ± 0.0034
1000	0.1842 ± 0.0029	0.1842 ± 0.0034	0.1842 ± 0.0034
1100	0.1845 ± 0.0028	0.1845 ± 0.0034	0.1845 ± 0.0033
1200	0.1756 ± 0.0027	0.1756 ± 0.0032	0.1756 ± 0.0032
1300	0.1735 ± 0.0027	0.1735 ± 0.0033	0.1735 ± 0.0033
1400	0.1643 ± 0.0026	0.1643 ± 0.0030	0.1643 ± 0.0030
1500	0.1657 ± 0.0025	0.1657 ± 0.0030	0.1657 ± 0.0029
1600	0.1621 ± 0.0025	0.1621 ± 0.0031	0.1621 ± 0.0030
1700	0.1538 ± 0.0024	0.1538 ± 0.0028	0.1538 ± 0.0028

Table E.2: Efficiencies and systematic uncertainties of the trigger EF_xe100 in gluino R-hadron signal samples simulated at $\sqrt{s} = 8$ TeV estimated with the three methods described above.

$m_{\tilde{g}}$	2012 method	contour method	grid method
100	0.0407 ± 0.0015	0.0407 ± 0.0016	0.0407 ± 0.0016
200	0.0867 ± 0.0027	0.0867 ± 0.0030	0.0867 ± 0.0029
300	0.1185 ± 0.0027	0.1185 ± 0.0031	0.1185 ± 0.0031
400	0.1351 ± 0.0029	0.1351 ± 0.0033	0.1351 ± 0.0033
500	0.1518 ± 0.0031	0.1518 ± 0.0035	0.1518 ± 0.0035
600	0.1570 ± 0.0030	0.1570 ± 0.0035	0.1570 ± 0.0035
700	0.1562 ± 0.0030	0.1562 ± 0.0034	0.1562 ± 0.0034
800	0.1599 ± 0.0029	0.1599 ± 0.0035	0.1599 ± 0.0035
900	0.1568 ± 0.0029	0.1568 ± 0.0034	0.1568 ± 0.0033
1000	0.1547 ± 0.0029	0.1547 ± 0.0034	0.1547 ± 0.0033
1100	0.1532 ± 0.0028	0.1532 ± 0.0033	0.1532 ± 0.0033
1200	0.1466 ± 0.0026	0.1466 ± 0.0032	0.1466 ± 0.0031
1300	0.1438 ± 0.0028	0.1438 ± 0.0033	0.1438 ± 0.0032
1400	0.1387 ± 0.0025	0.1387 ± 0.0030	0.1387 ± 0.0029
1500	0.1396 ± 0.0025	0.1396 ± 0.0030	0.1396 ± 0.0030
1600	0.1356 ± 0.0026	0.1356 ± 0.0030	0.1356 ± 0.0029
1700	0.1303 ± 0.0023	0.1303 ± 0.0027	0.1303 ± 0.0027

Table E.3: Efficiencies and systematic uncertainties of the trigger EF_xe100_tclcw_loose in gluino R-hadron signal samples simulated at $\sqrt{s} = 8$ TeV estimated with the three methods described above.

$m_{\tilde{g}}$	2012 method	contour method	grid method
100	0.0673 ± 0.0026	0.0673 ± 0.0031	0.0673 ± 0.0031
200	0.1326 ± 0.0034	0.1326 ± 0.0044	0.1326 ± 0.0043
300	0.1680 ± 0.0036	0.1680 ± 0.0046	0.1680 ± 0.0045
400	0.1902 ± 0.0038	0.1902 ± 0.0049	0.1902 ± 0.0049
500	0.2090 ± 0.0039	0.2090 ± 0.0051	0.2090 ± 0.0050
600	0.2123 ± 0.0037	0.2123 ± 0.0048	0.2123 ± 0.0048
700	0.2118 ± 0.0037	0.2118 ± 0.0048	0.2118 ± 0.0048
800	0.2137 ± 0.0036	0.2137 ± 0.0047	0.2137 ± 0.0047
900	0.2108 ± 0.0036	0.2108 ± 0.0046	0.2108 ± 0.0046
1000	0.2053 ± 0.0036	0.2053 ± 0.0046	0.2053 ± 0.0046
1100	0.2055 ± 0.0033	0.2055 ± 0.0044	0.2055 ± 0.0043
1200	0.1954 ± 0.0034	0.1954 ± 0.0044	0.1954 ± 0.0043
1300	0.1936 ± 0.0032	0.1936 ± 0.0042	0.1936 ± 0.0042
1400	0.1845 ± 0.0032	0.1845 ± 0.0042	0.1845 ± 0.0041
1500	0.1835 ± 0.0030	0.1835 ± 0.0039	0.1835 ± 0.0039
1600	0.1824 ± 0.0030	0.1824 ± 0.0040	0.1824 ± 0.0040
1700	0.1711 ± 0.0030	0.1711 ± 0.0038	0.1711 ± 0.0038

Table E.4: Efficiencies and systematic uncertainties of the trigger EF_xe110 in gluino R-hadron signal samples simulated at $\sqrt{s} = 8$ TeV estimated with the three methods described above.

$m_{\tilde{g}}$	2012 method	contour method	grid method
100	0.0339 ± 0.0013	0.0339 ± 0.0014	0.0339 ± 0.0014
200	0.0731 ± 0.0023	0.0731 ± 0.0026	0.0731 ± 0.0025
300	0.1059 ± 0.0025	0.1059 ± 0.0030	0.1059 ± 0.0030
400	0.1192 ± 0.0026	0.1192 ± 0.0032	0.1192 ± 0.0031
500	0.1370 ± 0.0028	0.1370 ± 0.0033	0.1370 ± 0.0033
600	0.1422 ± 0.0028	0.1422 ± 0.0034	0.1422 ± 0.0034
700	0.1413 ± 0.0027	0.1413 ± 0.0033	0.1413 ± 0.0033
800	0.1453 ± 0.0028	0.1453 ± 0.0033	0.1453 ± 0.0033
900	0.1427 ± 0.0027	0.1427 ± 0.0032	0.1427 ± 0.0032
1000	0.1380 ± 0.0026	0.1380 ± 0.0032	0.1380 ± 0.0031
1100	0.1378 ± 0.0026	0.1378 ± 0.0033	0.1378 ± 0.0032
1200	0.1325 ± 0.0025	0.1325 ± 0.0031	0.1325 ± 0.0030
1300	0.1279 ± 0.0025	0.1279 ± 0.0030	0.1279 ± 0.0029
1400	0.1259 ± 0.0023	0.1259 ± 0.0028	0.1259 ± 0.0028
1500	0.1266 ± 0.0024	0.1266 ± 0.0028	0.1266 ± 0.0028
1600	0.1222 ± 0.0023	0.1222 ± 0.0028	0.1222 ± 0.0028
1700	0.1183 ± 0.0021	0.1183 ± 0.0027	0.1183 ± 0.0027

Table E.5: Efficiencies and systematic uncertainties of the trigger HLT_xe80_L1XE50 in gluino R-hadron signal samples simulated at $\sqrt{s} = 13$ TeV estimated with the three methods described above.

$m_{\tilde{g}}$	2012 method	contour method	grid method
800	0.2977 ± 0.0099	0.2977 ± 0.0102	0.2977 ± 0.0102
1000	0.2987 ± 0.0105	0.2987 ± 0.0108	0.2987 ± 0.0108
1200	0.3063 ± 0.0099	0.3063 ± 0.0103	0.3063 ± 0.0103
1400	0.2981 ± 0.0099	0.2981 ± 0.0103	0.2981 ± 0.0103
1600	0.3104 ± 0.0097	0.3104 ± 0.0102	0.3104 ± 0.0101
1800	0.3020 ± 0.0097	0.3020 ± 0.0100	0.3020 ± 0.0100

Table E.6: Efficiencies and systematic uncertainties of the trigger HLT_xe80_L1XE70 in gluino R-hadron signal samples simulated at $\sqrt{s} = 13$ TeV estimated with the three methods described above.

$m_{\tilde{g}}$	2012 method	contour method	grid method
800	0.2809 ± 0.0076	0.2809 ± 0.0079	0.2809 ± 0.0079
1000	0.2799 ± 0.0080	0.2799 ± 0.0083	0.2799 ± 0.0083
1200	0.2867 ± 0.0075	0.2867 ± 0.0079	0.2867 ± 0.0079
1400	0.2794 ± 0.0075	0.2794 ± 0.0079	0.2794 ± 0.0079
1600	0.2905 ± 0.0074	0.2905 ± 0.0079	0.2905 ± 0.0079
1800	0.2855 ± 0.0074	0.2855 ± 0.0077	0.2855 ± 0.0077

Table E.7: Efficiencies and systematic uncertainties of the trigger HLT_xe80_tc_lcw_L1XE50 in gluino R-hadron signal samples simulated at $\sqrt{s} = 13$ TeV estimated with the three methods described above. Note: This trigger is the equivalent to the trigger EF_xe80_tclcw_loose.

$m_{\tilde{g}}$	2012 method	contour method	grid method
800	0.3397 ± 0.0115	0.3397 ± 0.0118	0.3397 ± 0.0118
1000	0.3452 ± 0.0123	0.3452 ± 0.0127	0.3452 ± 0.0126
1200	0.3510 ± 0.0116	0.3510 ± 0.0120	0.3510 ± 0.0119
1400	0.3416 ± 0.0115	0.3416 ± 0.0119	0.3416 ± 0.0118
1600	0.3490 ± 0.0111	0.3490 ± 0.0115	0.3490 ± 0.0115
1800	0.3456 ± 0.0115	0.3456 ± 0.0118	0.3456 ± 0.0118

Table E.8: Efficiencies and systematic uncertainties of the trigger HLT_xe80 in gluino R-hadron signal samples simulated at $\sqrt{s} = 13$ TeV estimated with the three methods described above.

$m_{\tilde{g}}$	2012 method	contour method	grid method
800	0.2927 ± 0.0090	0.2927 ± 0.0094	0.2927 ± 0.0093
1000	0.2928 ± 0.0095	0.2928 ± 0.0099	0.2928 ± 0.0099
1200	0.2996 ± 0.0090	0.2996 ± 0.0094	0.2996 ± 0.0093
1400	0.2931 ± 0.0090	0.2931 ± 0.0094	0.2931 ± 0.0094
1600	0.3042 ± 0.0089	0.3042 ± 0.0093	0.3042 ± 0.0093
1800	0.2965 ± 0.0088	0.2965 ± 0.0092	0.2965 ± 0.0091

Table E.9: Efficiencies and systematic uncertainties of the trigger HLT_xe100 in gluino R-hadron signal samples simulated at $\sqrt{s} = 13$ TeV estimated with the three methods described above.

$m_{\tilde{g}}$	2012 method	contour method	grid method
800	0.2483 ± 0.0061	0.2483 ± 0.0066	0.2483 ± 0.0066
1000	0.2500 ± 0.0064	0.2500 ± 0.0068	0.2500 ± 0.0069
1200	0.2583 ± 0.0062	0.2583 ± 0.0067	0.2583 ± 0.0067
1400	0.2501 ± 0.0063	0.2501 ± 0.0068	0.2501 ± 0.0069
1600	0.2611 ± 0.0063	0.2611 ± 0.0070	0.2611 ± 0.0070
1800	0.2603 ± 0.0060	0.2603 ± 0.0065	0.2603 ± 0.0065

Table E.10: Efficiencies and systematic uncertainties of the trigger HLT_xe100_pueta in gluino R-hadron signal samples simulated at $\sqrt{s} = 13$ TeV estimated with the three methods described above.

$m_{\tilde{g}}$	2012 method	contour method	grid method
800	0.2776 ± 0.0066	0.2776 ± 0.0070	0.2776 ± 0.0070
1000	0.2800 ± 0.0069	0.2800 ± 0.0073	0.2800 ± 0.0073
1200	0.2846 ± 0.0066	0.2846 ± 0.0070	0.2846 ± 0.0070
1400	0.2783 ± 0.0066	0.2783 ± 0.0071	0.2783 ± 0.0071
1600	0.2887 ± 0.0066	0.2887 ± 0.0072	0.2887 ± 0.0072
1800	0.2847 ± 0.0064	0.2847 ± 0.0068	0.2847 ± 0.0068

Table E.11: Efficiencies and systematic uncertainties of the trigger HLT_xe100_pufit in gluino R-hadron signal samples simulated at $\sqrt{s} = 13$ TeV estimated with the three methods described above.

$m_{\tilde{g}}$	2012 method	contour method	grid method
800	0.2821 ± 0.0058	0.2821 ± 0.0063	0.2821 ± 0.0063
1000	0.2826 ± 0.0061	0.2826 ± 0.0066	0.2826 ± 0.0066
1200	0.2893 ± 0.0058	0.2893 ± 0.0064	0.2893 ± 0.0063
1400	0.2819 ± 0.0059	0.2819 ± 0.0065	0.2819 ± 0.0064
1600	0.2912 ± 0.0058	0.2912 ± 0.0065	0.2912 ± 0.0065
1800	0.2875 ± 0.0056	0.2875 ± 0.0061	0.2875 ± 0.0061

Table E.12: Efficiencies and systematic uncertainties of the trigger HLT_xe100_tc_em in gluino R-hadron signal samples simulated at $\sqrt{s} = 13$ TeV estimated with the three methods described above.

$m_{\tilde{g}}$	2012 method	contour method	grid method
800	0.2587 ± 0.0071	0.2587 ± 0.0076	0.2587 ± 0.0076
1000	0.2579 ± 0.0074	0.2579 ± 0.0079	0.2579 ± 0.0078
1200	0.2671 ± 0.0072	0.2671 ± 0.0077	0.2671 ± 0.0076
1400	0.2600 ± 0.0073	0.2600 ± 0.0078	0.2600 ± 0.0078
1600	0.2706 ± 0.0074	0.2706 ± 0.0080	0.2706 ± 0.0080
1800	0.2662 ± 0.0069	0.2662 ± 0.0073	0.2662 ± 0.0073

Table E.13: Efficiencies and systematic uncertainties of the trigger HLT_xe100_tc_lcw in gluino R-hadron signal samples simulated at $\sqrt{s} = 13$ TeV estimated with the three methods described above.

$m_{\tilde{g}}$	2012 method	contour method	grid method
800	0.2821 ± 0.0057	0.2821 ± 0.0062	0.2821 ± 0.0062
1000	0.2825 ± 0.0060	0.2825 ± 0.0065	0.2825 ± 0.0065
1200	0.2893 ± 0.0057	0.2893 ± 0.0063	0.2893 ± 0.0062
1400	0.2817 ± 0.0058	0.2817 ± 0.0064	0.2817 ± 0.0063
1600	0.2913 ± 0.0057	0.2913 ± 0.0064	0.2913 ± 0.0064
1800	0.2875 ± 0.0056	0.2875 ± 0.0060	0.2875 ± 0.0060

Selbständigkeitserklärung

Ich versichere hiermit, die vorliegende Arbeit mit dem Titel

Triggerstudien zur Suche nach stabilen, massiven Teilchen mit dem ATLAS-Detektor

selbständig verfasst zu haben und keine anderen als die angegebenen Quellen und Hilfsmittel verwendet zu haben.

Vincent Kitali

München, den 30. September 2015